Cell Reports
Medicine

Article

Genetic and microenvironmental evolution of colorectal liver metastases under chemotherapy

Graphical abstract

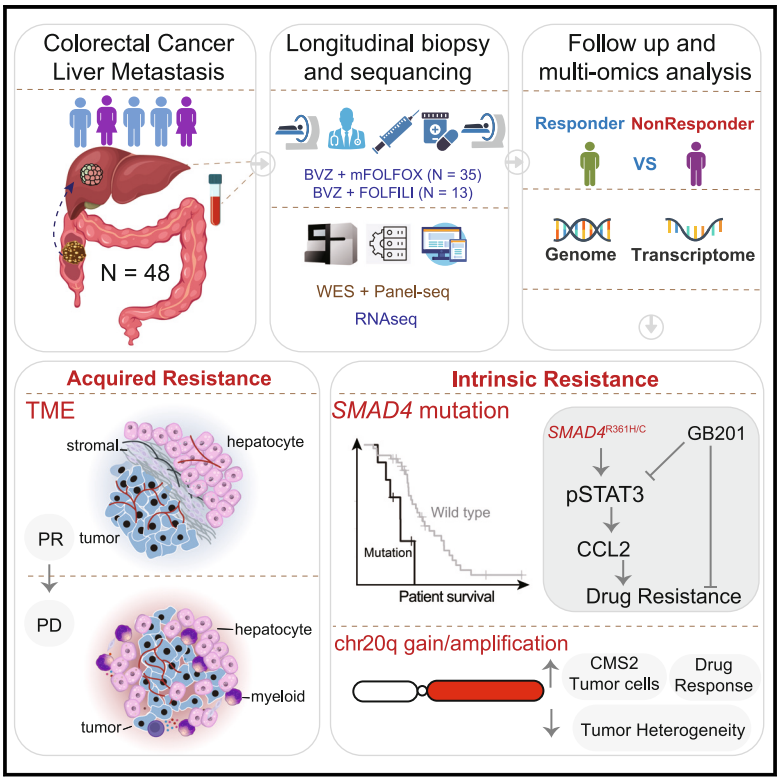

Highlights

- Longitudinal sequencing reveals TME reorganization after BVZ-C therapy
- Acquired resistance associates with the spatial distance of tumors and hepatocytes
- *SMAD4* mutation and chr20q copy-number gain associate with intrinsic resistance
- STAT3 inhibition overcomes resistance in *SMAD4*-mutant cells and holds therapeutic potential

Authors

Min Shi, Yingxi Yang, Na Huang, ..., Quanhua Mu, Jiguang Wang, Wangjun Liao

Correspondence

jgwang@ust.hk (J.W.),
liaowj@smu.edu.cn (W.L.)

In brief

Shi et al. identified spatial and genetic factors contributing to intrinsic and acquired resistance in patients with colorectal cancer liver metastases. By demonstrating the restoration of therapeutic response with a STAT3 inhibitor, this study paves the way for targeted therapeutic strategies to overcome drug resistance.

Shi et al., 2024, Cell Reports Medicine *5*, 101838
December 17, 2024
https://doi.org/10.1016/j.xcrm.2024.101838

CellPress

Cell Reports Medicine

CellPress
OPEN ACCESS

Article

Genetic and microenvironmental evolution of colorectal liver metastases under chemotherapy

Min Shi,[1,3,5,6] Yingxi Yang,[2,6] Na Huang,[1,6] Dongqiang Zeng,[1,3,5,6] Zongchao Mo,[2,6] Jiao Wang,[1] Xiaomeng Zhang,[2] Ran Liu,[2] Chunlin Wang,[1] Xiaoxiang Rong,[1] Zhenzhen Wu,[1] Qiong Huang,[1] Haixia Shang,[2] Jihong Tang,[2] Zhaojun Wang,[1] Jianan Cai,[1] Genjie Huang,[1] Yijin Guan,[1] Jian Guo,[1] Quanhua Mu,[2] Jiguang Wang,[2,4,*] and Wangjun Liao[1,3,5,7,*]

[1]Department of Oncology, Nanfang Hospital, Southern Medical University, Guangzhou, Guangdong 510515, P.R. China
[2]Department of Chemical and Biological Engineering, Division of Life Science and State Key Laboratory of Molecular Neuroscience, The Hong Kong University of Science and Technology, Clear Water Bay, Kowloon, Hong Kong SAR, China
[3]Cancer Center, the Sixth Affiliated Hospital, School of Medicine, South China University of Technology, Foshan, China
[4]SIAT-HKUST Joint Laboratory of Cell Evolution and Digital Health, HKUST Shenzhen-Hong Kong Collaborative Innovation Research Institute, Futian, Shenzhen 518000, P.R. China
[5]Foshan Key Laboratory of Translational Medicine in Oncology, the Sixth Affiliated Hospital, School of Medicine, South China University of Technology, Foshan, China
[6]These authors contributed equally
[7]Lead contact
*Correspondence: jgwang@ust.hk (J.W.), liaowj@smu.edu.cn (W.L.)
https://doi.org/10.1016/j.xcrm.2024.101838

SUMMARY

Drug resistance limits the efficacy of chemotherapy for colorectal cancer liver metastasis (CRLM). However, the evolution of CRLM during drug treatment remains poorly elucidated. Multi-omics and treatment response data from 115 samples of 49 patients with CRLM undergoing bevacizumab (BVZ)-based chemotherapy show little difference in genomic alterations in 92% of cases, while remarkable differences are observed at the transcriptomic level. By decoupling intrinsic and acquired resistance, we find that hepatocyte and myeloid cell infiltration contribute to 38.5% and 23.1% of acquired resistance, respectively. Importantly, *SMAD4* mutations and chr20q copy-number gain are associated with intrinsic chemoresistance. Gene interference experiments suggest that *SMAD4*$^{R361H/C}$ mutations confer BVZ and 5-fluorouracil (5-FU) resistance through STAT3 signaling. Notably, supplementing BVZ and 5-FU with the STAT3 inhibitor GB201 restores therapeutic efficacy in *SMAD4*$^{R361H/C}$ cancer cells. Our study uncovers the evolutionary dynamics of CRLM and its microenvironment during treatment and offers strategies to overcome drug resistance.

INTRODUCTION

Colorectal cancer liver metastases (CRLMs) constitute approximately 70% of colorectal cancer (CRC)-related deaths.[1] In 2004, the Food and Drug Administration (FDA) approved bevacizumab (BVZ), an antiangiogenic agent, in combination with chemotherapeutic agents for treating metastatic CRC (mCRC).[2] Since then, its application has been extended to various treatment regimens, including first- and cross-line therapies,[3,4] adjuvant therapy,[5] and maintenance therapy.[6] BVZ-based chemotherapies (BVZ-C therapies) are currently administered as the primary first-line treatment for CRC and CRLMs. Notwithstanding such progress, nearly 50% of patients with CRLM fail to respond,[7] and many patients who initially benefit would relapse rapidly.[8] Identifying predictive biomarkers of BVZ-C therapy responders in patients with CRLM is urgently needed to optimize therapeutic decisions.

Exome and transcriptome sequencing technologies have revolutionized our knowledge of CRC and its metastases. The Cancer Genome Atlas (TCGA) group[9] and Yaeger et al.[10] established a comprehensive genomic landscape of CRC and metastatic CRCs. Subsequent expression-based analyses classified CRC into four consensus molecular subtypes (CMSs) with distinguishing features.[11] More recently, Zhao et al. expanded our knowledge of Chinese patients, linking tumor genomic heterogeneity to different clinical characteristics.[12] Nevertheless, the clinical and molecular features associated with treatment response remain poorly understood owing to the unavailability of treatment data in these studies.

Remarkable efforts have been devoted to identifying biomarkers of BVZ-C therapy response in patients with CRC. Smeets et al. performed low-coverage whole-genome sequencing on patients with CRC treated with BVZ-C and discovered the role of chromosomal instability in treatment outcomes.[13] However, it is unclear how tumor cells evolve to become chemoresistant in response to therapy. Additionally, drug resistance cannot be completely explained by genomic factors.[14,15] Several studies have focused on non-genetic resistance mechanisms, such as epithelial-mesenchymal transition, metabolic reprogramming, and tumor-stromal cell interactions,[16] particularly in microenvironment-targeted strategies, such as

BVZ. It has been reported that the redundancy of angiogenic signaling molecules, vascular symbiosis, and increased infiltration of fibroblasts and myeloid cells are closely related to BVZ resistance.[17,18] Studies have suggested that the molecular mechanisms of genetic and non-genetic drug resistance are heterogeneous but partly overlapping.[16] Hence, characterizing the evolution of the tumor and tumor microenvironment (TME) induced by BVZ-C treatment is crucial for understanding the mechanisms of drug resistance.

In this study, we provided a longitudinal cohort of matched pre- and post-treatment samples from 49 patients with CRLM who received BVZ-C therapy as the first-line standard treatment. Leveraging whole-exome and RNA sequencing of multi-time point tumor samples during the course of clinical treatment of patients with CRLM, we aimed to dissect the underlying molecular and TME determinants that may regulate patient prognosis and tumor response to treatment.

RESULTS

Longitudinal sequencing characterized CRLM under treatment

To investigate the treatment efficacy of CRLM, we enrolled 49 patients diagnosed as CRLM at Nanfang Hospital of Southern Medical University. They were treated with BVZ plus either mFOLFOX6 (oxaliplatin + 5-fluorouracil [5-FU]) or FOLFIRI (irinotecan + 5-FU), with follow-up durations ranging from 1.5 months to over 50 months (Figure 1A; Table S1). Of the full cohort, 77% migrated from left-sided CRCs, 83% were staged IVA or IVB, and 42% simultaneously developed lung metastases. The median age at diagnosis was 55.5 years, range: 29–79 years (Figure S1A). The median progression-free survival (PFS) and overall survival (OS) for the cohort were 9.97 and 25.37 months, respectively (Figure S1B). To assess the treatment response of each tumor sample, we used Response Evaluation Criteria in Solid Tumors (RECIST) 1.1[19] to classify all samples into partial response (PR), stable disease (SD), or progressive disease (PD) (Figure 1B). We then defined responders as those with PR or non-continuous stable disease (tumor volumes shrink continually to PR within two cycles) and non-responders as those with PD or continuous stable disease (tumor size was stable or increasing to PD over at least four months; Figures 1C and S1C). As a result, 48 patients were stratified into 21 responders and 27 non-responders, and one patient (B29) was not stratified owing to inadequate follow-up. Responders (median PFS: 11.67 months) portended a longer PFS than non-responders (median PFS: 8.33 months, p = 4.0e−2; Figure S1D). Cohort-level analysis of the response rate showed no significant difference between the two first-line regimens (mFOLFOX6-BVZ: 60% [95% exact confidence interval (CI): 42.11%–76.13%, 21 of 35 patients] versus FOLFIRI-BVZ: 46.2% [95% exact CI: 19.22%–74.87%, 6 of 13 patients]) (Figure 1D). Similarly, they had comparable PFS and OS rates (Figure S1E), which are consistent with a previous study.[20] Further examination of clinical parameters showed that neither age, gender, primary site, nor the number of metastases was associated with the response to BVZ-based therapies, while lung metastases were slightly higher in responders (56%, p = 0.04, Figure S1A).

It is worth mentioning that in the context of BVZ-C therapies for CRLMs, a usual pattern is observed in which patients initially respond well to treatment; however, as treatment continues, drug resistance almost inevitably emerges.[21,22] To monitor CRLM evolution in response to therapeutic pressures, longitudinal tumor specimens (n = 115) were collected (through either biopsy or surgery) from the patients, among whom two cases had four tumor samples, i.e., pre-treatment (Pre), Post1, Post2, and Post3; 13 cases had three tumor samples (Pre, Post1, and Post2), and the remaining cases had two samples. We observed that approximately half of the patients were non-responders at the beginning, and the proportion of non-responders steadily increased over time, reaching 100% in the 10th month after the first BVZ-C therapy (Figure 1E). To investigate the molecular mechanisms of both intrinsic resistance (IR) and acquired resistance (AR) in BVZ-C-treated CRLMs, we carried out DNA and/or RNA sequencing on the enrolled tumor samples, coupled with matched blood controls, leading to whole-exome sequencing (WES) or panel-seq data of 115 samples and RNA sequencing (RNA-seq) data of 100 samples (Figure 1F).

Genomic aberrations were preserved after treatment

To delineate the evolving landscape of tumor genomic mutations, we analyzed the WES and panel-seq data. WES achieved a median of 318× (125×–657×) coverage in tumors and 313× (137×–535×) in normal blood. In the panel-seq data, the average depth of the targeted regions was 500×. The median somatic mutation load per sample was 83 (range, 0–235; Table S2). We detected somatic mutations in the driver genes of CRC (Figure S2), including *TP53* (73.5%), *APC* (63.3%), *KRAS* (57.1%), *PIK3CA* (18.4%), *BRAF* (12.2%), and *SMAD4* (16.3%). The altered signaling pathways were P53 (77.6%), WNT (75.5%), RTK/RAS (69.4%), TGF (26.5%), and PI3K (26.5%). Compared to the TCGA CRC dataset,[9] CRLMs in this cohort displayed a higher incidence of *TP53* mutations (73.5% versus 53.8%, p = 1.2e−2), with comparable mutation rates for other reported genes (Figure S2). In addition, this cohort demonstrated a greater prevalence of microsatellite stability (MSS: 100% versus 70.2% in TCGA, p = 9.7e−6; Figure S2), consistent with a recent study that reported a high proportion of MSS among Chinese patients with mCRC.[23]

We then used the CELLO pipeline[24] to characterize the evolutionary landscape of CRLM under therapy. All driver genes had consistent mutation frequencies in tumors before and after treatment (Figure 2A), and no statistical differences were observed in the overall burden of somatic mutations (pre [median: 90, 0–202]; post [median: 86, range: 0–235]; Figure 2B), nor in chromosomal copy-number heterogeneity[25] (CNH, a global measure of chromosomal complexity; Figure S3A) between the baseline and treated tumors. In sharp contrast, a significant reduction in tumor purity was observed after therapy (Figure 2C), particularly in the responder group, with no change in the non-responder group (Figure S3B). We constructed phylogenetic trees to explore the temporal evolution of tumors under treatment-induced pressures and then mapped them to a Moduli space (Figure S3C). Our analysis indicated that most patients were clustered in the common corner (Figure S3D), but a few cases were scattered near the pre- or post-treatment private corner, potentially biased by the low tumor content (Figure S3C). We then applied an

CellPress
OPEN ACCESS

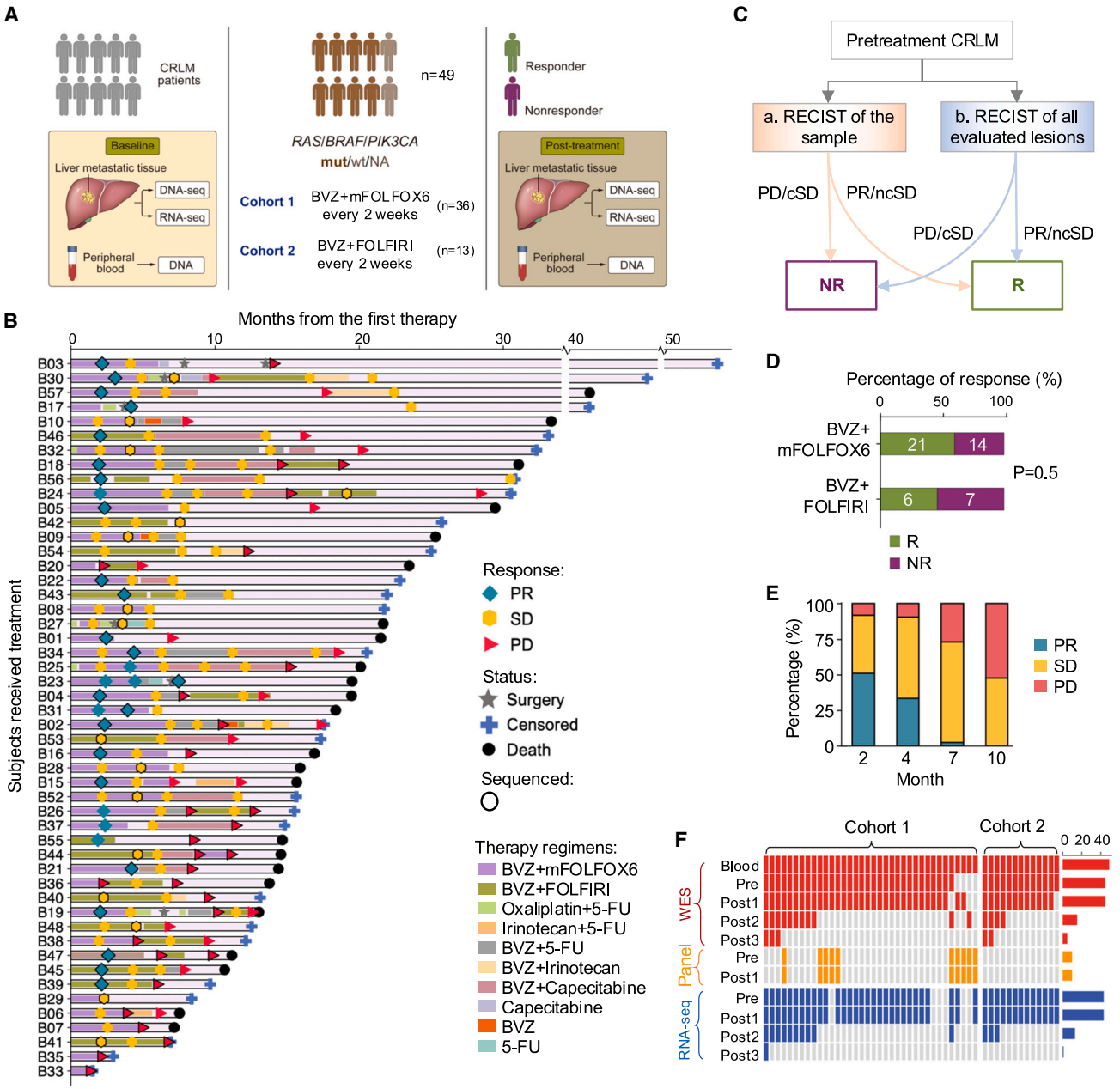

Figure 1. Longitudinal follow-up and multi-omics characterization of CRLM under chemotherapy

(A) Schematic diagram of patient enrollment and sample collection.

(B) Swimmer plot depicting time on treatment, duration of treatment, response, and survival characteristics. Each lane represents a single patient's data. The x axis represents the duration of therapy for each patient. The key within the plot describes all symbols and color coding. Samples sequenced are encircled with black border.

(C) Guideline of response classification based on RECIST 1.1. Samples with inconsistent assessment are labeled with criteria b. cSD, continuous stable disease (SD for 4 months or SD for 2 months and then PD for 2 months); ncSD, non-continuous stable disease (SD for 2 months and then PR for 2 months). R: responder; NR: non-responder.

(D) Bar plot comparing differences in objective response rate between treatment arms.

(E) Bar plot depicting response rate over time in our cohort. The x axis indicates the number of months after the start of treatment and y axis denotes the fraction of different response groups.

(F) Summary of DNA and RNA sequencing data collected in this study. See also Figure S1.

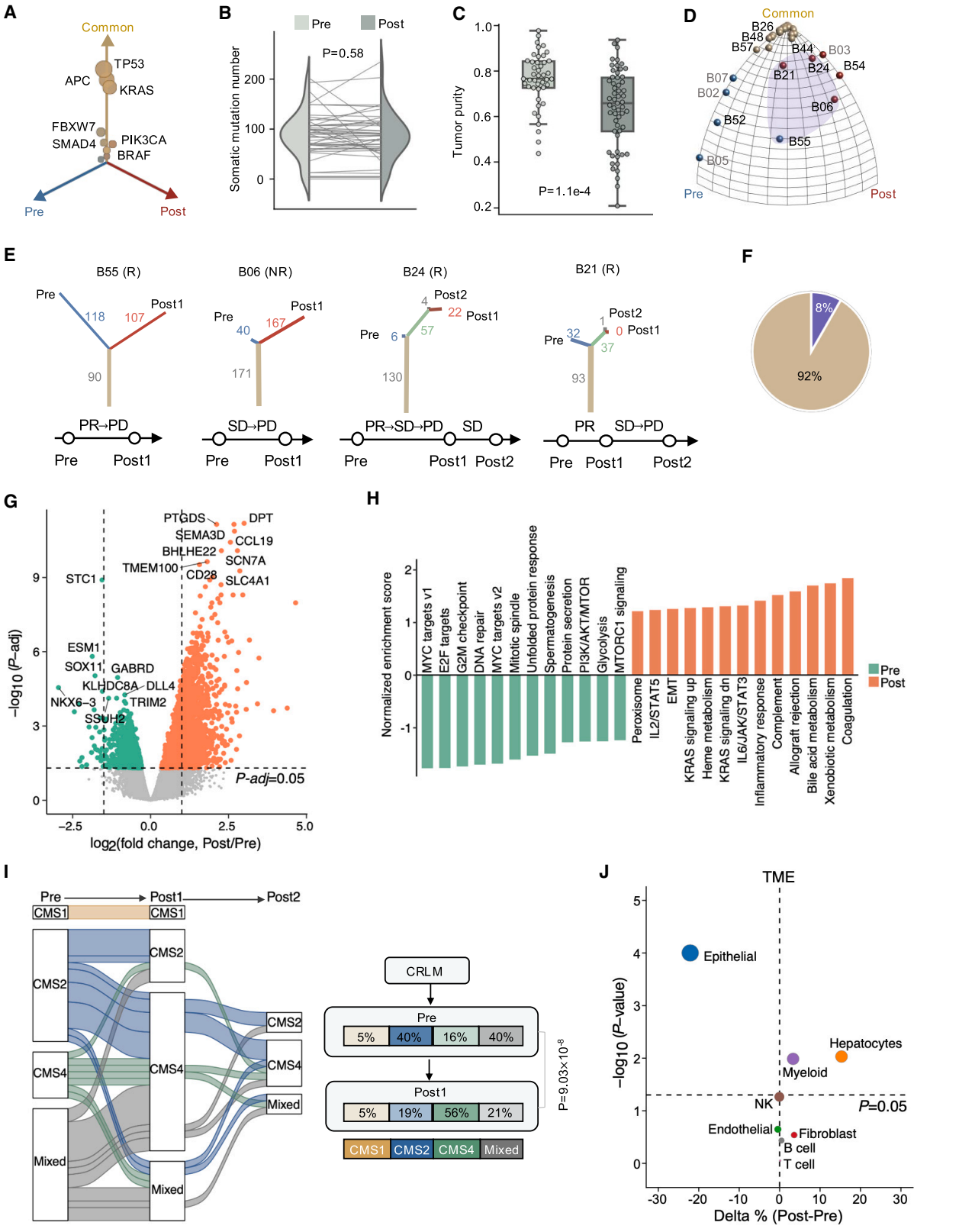

(legend on next page)

in-house mathematical method, the Evolutionary Tree Inference Program (ETRIP) (Figure S3E), to recover the number of underestimated mutations due to limited sequencing coverage and/or low tumor purity from the DNA sequencing data (Methods). Using ETRIP, we reconstructed phylogenetic trees and observed that 92% of CRLM tumors showed no substantial divergence in genomic profiles in response to current treatment regimens (linear evolution, Figure 2D). Nevertheless, post-treatment tumors from four cases (B21, B24, B05, and B55; Figures 2E and 2F) acquired 37 to 167 coding mutations compared to baseline tumors (branched evolution). Together, our data showed a marked convergence in the tumor genome during therapy.

Treatment reshaped TME

Next, we sought to investigate the transcriptomic changes in CRLM during therapy. RNA sequencing data from 100 pre- or post-treatment tumor samples of 43 patients were collected and processed following the standard pipeline (Methods). To evaluate temporal changes in gene expression, we conducted differentially expressed gene (DEG) analysis between pre- and post-treatment samples and identified 4,573 DEGs after controlling for the false discovery rate ($q < 0.05$, Figure 2G), suggesting that treatment remarkably perturbs either tumor cell transcriptomic profiles, TME, or both. Subsequent gene set enrichment analysis (GSEA) revealed prevailing downregulation of cell proliferation hallmarks such as MYC targets, E2F targets, G2M checkpoints, and DNA repair, and strong upregulation of genes involved in epithelial-mesenchymal transition (EMT), immunity-related (e.g., coagulation, complement, and inflammatory response), and metabolism-related hallmarks (e.g., xenobiotic metabolism, bile acid metabolism, and heme metabolism) after treatment (Figure 2H). Using the CMS classification system,[11] we assessed the transcriptional subtype for each CRLM sample and examined phenotype transitions in matched pre- and post-treatment pairs. Importantly, the baseline CMS2-canonical/epithelial (58.8%, 10/17) and mixed subtypes (58.8%, 10/17) switched to CMS4-mesenchymal/stromal subtypes after treatment (Figure 2I). These observations signified that BVZ-C therapy triggers significant transcriptional reconfiguration and phenotypic variation.

To further discern how BVZ-C therapy may impact the TME, we deconvolved the RNA expression data using BayesPrism,[26] a Bayesian method that jointly reconstructs cell type abundance and cell-type-specific gene expression profiles from bulk transcriptomes (Methods). To test the performance of BayesPrism in the CRLM dataset, we generated pseudobulk samples from public CRLM single-cell profiles covering eight major cell types.[27] The cell type proportions inferred by BayesPrism were highly concordant with the ground truth (Figure S4A). As expected, using deconvolution in our cohort, we found strong correlations between the proportion of epithelial (tumor cells) proportions and the estimated tumor purity based on independent methods (Figure S4B). Surprisingly, DEG analysis of epithelial cells revealed that the transcriptional profile of tumor cells showed little change after therapy (Figure S4C). This observation resembled our aforementioned findings concerning rare treatment-associated genomic changes. Therefore, we turned our attention to TME dynamics and observed a notable reduction in epithelial cells along with increased infiltration of hepatocytes and myeloid cells after treatment (Figures 2J and S4D), implying an evolving shift in the composition of TME cells as a key feature of BVZ-C treatment.

We next compared the transcriptional features of samples before and after treatment by the response group. Compared to the non-responders, a notably higher number of DEGs were detected between pre- and post-treatment samples in the responders (Figure S5A). Enrichment analysis revealed that cell cycle/proliferation pathways were prevalent in pre-treatment samples from both groups, while metabolism and immune response pathways were enriched in post-treatment samples of responders (Figure S5B). Responders also displayed a greater CMS2-to-CMS4 shift following treatment (Figures S5C and S5D). Moreover, treatment significantly altered the TME in responders, reducing epithelial cells and increasing hepatocytes and myeloid cells, with no notable changes in non-responders (Figures S5E and S5F). Collectively, responders to the treatment demonstrated more substantial transcriptional changes, encompassing more DEGs, a larger CMS2-to-CMS4 shift, and greater TME dynamics than non-responders.

Spatial proximity of hepatocytes and tumors contributed to acquired resistance

To uncover the molecular mechanisms of how IR and AR limit treatment benefit (Figure 1E), we developed a biomarker

Figure 2. Genomic and transcriptomic profiles of pre- and post-treatment CLRMs

(A) Three-dimensional bubble plot showing the frequency of pre-treatment-private (blue; left axis), post-treatment-private (red; right axis), and common somatic mutations (yellow; upper axis).

(B) Somatic mutation number of pre-treatment tumors versus post-treatment tumors. *p* value: two-sided paired t test.

(C) Tumor purity (inferred by ESTIMATE) of pre-treatment versus post-treatment tumors. *p* value: two-sided Mann-Whitney U test.

(D) Ternary plot of moduli space of evolutionary trees inferred by ETRIP. Each ball represents a patient, with colors indicating three clusters within moduli space. Patients with a higher fraction of shared somatic mutations between pre- and post-treatment stages are clustered near the "Common" corner, while those with a significant reduction in mutations after treatment are located near the "Pre" corner. Purple shading highlights patients with branched tumor evolution.

(E) The phylogenetic tree and response history for the four patients highlighted in (D).

(F) The proportion of patients with linear evolution (yellow) and branched evolution (purple).

(G) Volcano plot showing DEGs in post-treatment versus pre-treatment tumor samples.

(H) The enriched hallmark gene sets in baseline compared with post-treatment samples.

(I) Consensus molecular subtype (CMS) transitions under treatment (left). Right: proportion change in each subtype. *p* value: chi-squared test.

(J) Percentage changes of various cell types between post-treatment and pre-treatment samples. Relative percentage of each cell type within the bulk RNA-seq samples is inferred by the deconvolution method BayesPrism. Percentage changes (delta %) are calculated by subtracting the average cell type proportions in treated samples from those in baseline samples. The bubble size is proportional to $-\log_{10}(p \text{ value})$. *p* value: two-sided Mann-Whitney U test. See also Figures S2–S5.

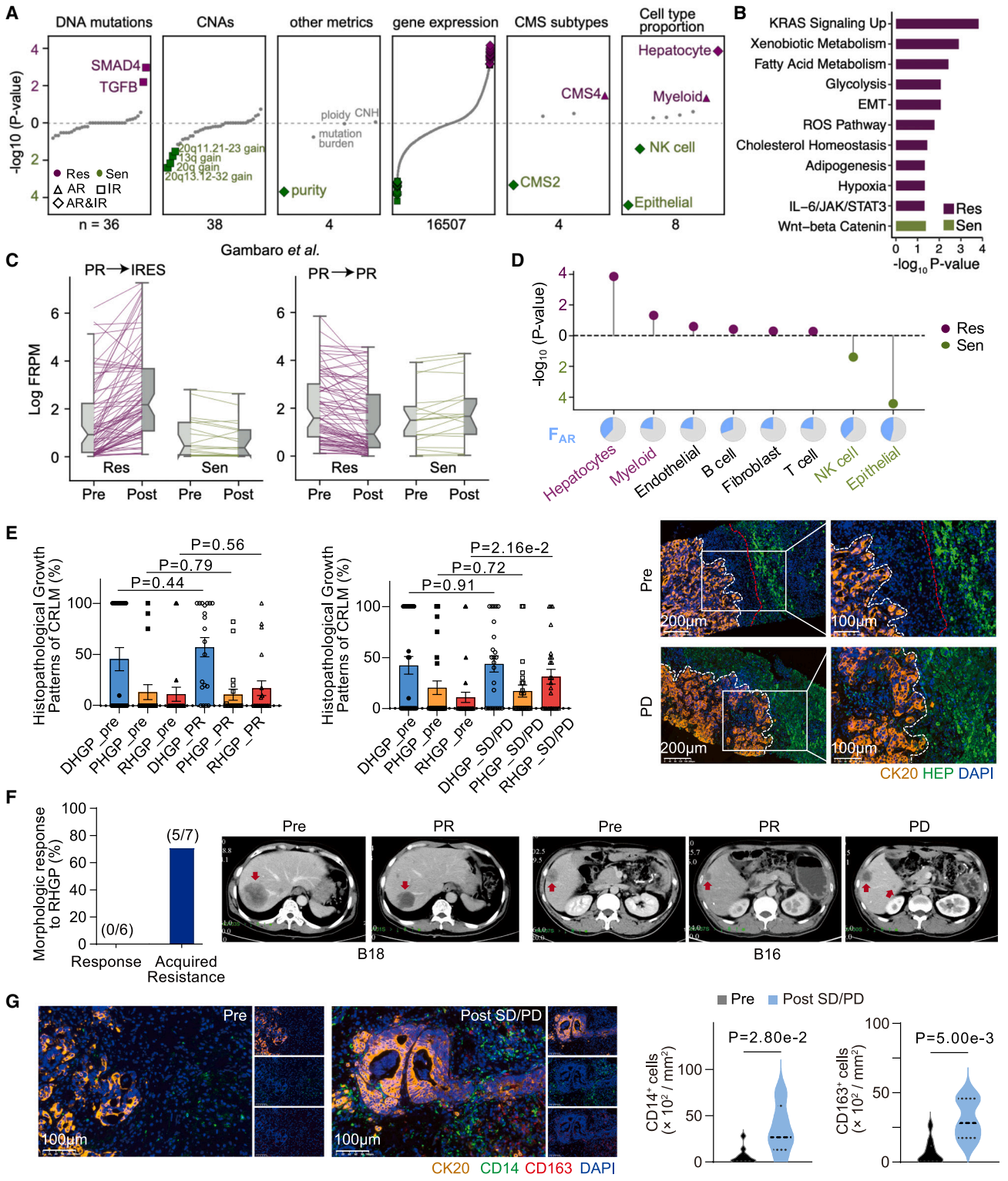

Figure 3. Genomic and transcriptomic factors associated with AR

(A) Different types of features prioritized by SRFS. Each dot represents an individual feature and significant AR or IR-associated features are highlighted in green (pro-sensitive) or purple (pro-resistant). The digital number at the bottom summarizes total feature numbers for the corresponding feature type. Shapes indicate the therapeutic resistance types (triangle: AR-only, square: IR-only, diamond: AR and IR).

(B) The enriched hallmark gene sets from the AR-related genes identified from (A).

(legend continued on next page)

detection method, termed SRFS (sample-based response feature selection) (Figure S6A; Table S3) to dissect the contributors of AR and IR. For each feature, SRFS evaluated its discriminative power between sensitive (PR, n = 27) and resistant groups (SD or PD, n = 64) using a univariate logistic regression model (continuous features) or a Fisher's exact test (categorical features) and derived its relative contribution to AR and IR (Methods). Employing SRFS on a comprehensive list of DNA and RNA features, we identified 107 significant AR-related features (24 sensitive-relevant and 83 resistant-relevant; Figure S6B; Tables S4 and S5). We observed that none of the genomic features were significantly associated with AR, spanning mutations, copy-number alterations (CNAs), ploidy, mutation burden, and CNH (Figures S6B and 3A). Instead, we found that AR was largely dependent on transcriptomic features. Specifically, the sensitive-relevant features encompassed tumor purity, CMS2 subtype, relative abundance of epithelial and natural killer (NK) cells, and expression levels of 20 genes, whereas the resistant-relevant features nominated the CMS4 subtype, relative abundance of hepatocytes and myeloid cells, and expression levels of 80 genes (Figure 3A and S6B–D). Enrichment of the sensitive-relevant genes designated Wnt/β-catenin signaling. In contrast, the resistant-relevant genes were mainly enriched in cancer hallmarks, including KRAS signaling upregulation, metabolism, EMT, hypoxia, and IL-6/JAK/STAT3 signaling (Figure 3B). Given the strong association between the expression levels of these genes and AR in our cohort (Figure S6E), we tested this association in two previously published patients with CRLM treated with oxaliplatin + BVZ.[28] Consistently, upregulation of resistant-relevant genes was observed in the patient with disease progression, while the responsive patient displayed the opposite trend (Figure 3C), indicating that these resistant-relevant genes were important for tumor progression.

Following our earlier observations of AR-related cell types (Figure 3A), we found that increased infiltration of hepatocytes and myeloid cells contributed to 38.5% and 23.1% of AR, respectively (Figure 3D), pinpointing the potential resistance-promoting roles of the hepatic and myeloid milieu. The spatial transcriptome dataset of patients with CRLM[29] also revealed the increased hepatocyte infiltration and decreased spatial distance between hepatocytes and tumor cells after XELOX treatment (Figure S6F). Interestingly, previous studies have corroborated that replacement histopathological growth patterns (RHGPs), characterized by tumor cell invasion into hepatic plates and co-option of existing sinusoidal vessels within the liver parenchyma, were closely correlated with an adverse response to BVZ-C.[17,18,30] To elucidate the relationship between AR and the spatial organization of tumors and hepatocytes in our cohort, we classified CRLMs into three different histopathological growth patterns (HGPs)[31]: desmoplastic HGP (DHGP), pushing HGP (PHGP), and RHGP, which corresponds to a gradual decrease in the spatial distance between the two. Our quantification of the three HGPs in CRLM samples using hematoxylin-eosin (HE) staining demonstrated a significant increase in RHGP patterns in treated SD/PD samples compared to baseline, with no significant changes observed in the DHGP and PHGP patterns (Figure 3E). Conversely, the post-treatment PR group exhibited no changes in RHGP patterns compared with the baseline controls. Some examples were examined in Figure 3E by multiplex immunofluorescence (mIF) staining, and samples that developed AR showed a markedly reduced distance between tumor cells and hepatocytes. Assessment of contrast-enhanced computed tomography (CT) images also revealed a higher proportion of RHGP in disease-progressive tumors than in disease-responsive tumors (Figure 3F). Furthermore, mIF staining confirmed a notably larger proportion of $CD14^+$ (monocyte marker) and $CD163^+$ (macrophage marker) cells surrounding disease-progressive tumors compared to the responsive baseline levels (Figure 3G). In sum, our data suggested the tumor and hepatic cell proximity, as well as elevated myeloid cell abundance as potential mechanisms underlying AR to BVZ-C therapy.

SMAD4 mutations and chr20q-gain contributed to IR

By leveraging the SRFS method, we identified 100 features that were significantly related to IR (Figure S7A; Tables S4 and S5). Whereas the somatic mutation load CNH and ploidy were not correlated with IR (Figure 3A), somatic *SMAD4* mutations, TGF-β pathway mutations, relative abundance of hepatocytes, and the upregulation of 50 genes were the key IR factors promoting resistance, and amplification/gain of chromosome 20q13.12–32, 20q, 13q, and 20q11.21–23, high tumor purity, CMS2 subtype, relative abundance of epithelial and NK cells, and the upregulation of 50 genes were the significant favorable factors for a positive response (Figure 3A). Interestingly, the top pro-sensitive genes were enriched in chromosome 20q, which included *SALL4*, *MYH7B*, *TAF4*, *FITM2*, and *TTI1*, echoing

(C) Validation of AR-related genes in samples from an independent cohort. Re-analysis of previously reported patients demonstrated that pro-resistant genes are remarkably upregulated in P029 (left side) but downregulated in P135 (right side). Both patients were partial response (PR) when treated by oxaliplatin plus BVZ, and P029 became IRES (lesions continue to grow under therapy) when the post-treatment sample was collected, while P135 remained PR.

(D) Lollipop plot showing −log10 p values of the AR relevance for different cell type proportions calculated by SRFS. Relative proportion for each cell type is inferred by BayesPrism. Pie charts (bottom) show the fraction of patients whose AR was potentially contributed by certain cellular type.

(E) Comparison of three histopathological growth patterns (HGPs) of CRLMs before and after treatment. Left: proportion of HGPs by HE staining in SD/PD (n = 36) or PR (n = 20) and corresponding pre-treatment nodes. p value: unpaired t test. Right: representative immunofluorescence images of HGPs from tissues of hepatic metastases in the PD and pre-treatment stages. Scale bars, 100 and 200 μm, respectively. The white and red dashed lines indicate the tumor interface and liver-stromal interface, respectively. DHGP, desmoplastic HGP; PHGP, pushing HGP; RHGP, replacement HGP; CK20, cytokeratin 20 (cancer cell marker); HEP, hepatocyte (hepatocyte marker).

(F) A histogram (left) and representative images (right) demonstrate the proportion of RHGP based on CT images in response (n = 6) and acquired resistance (n = 7) CRLM cohorts. Red arrows indicate liver metastases.

(G) Representative IF images (left) and quantification (right) of monocytes ($CD14^+$) and macrophages ($CD163^+$) in CRLM samples from SD/PD (n = 5) and pre-treatment (n = 10). p value: two-sided Mann-Whitney U test. Scale bars, 100 μm. See also Figure S6.

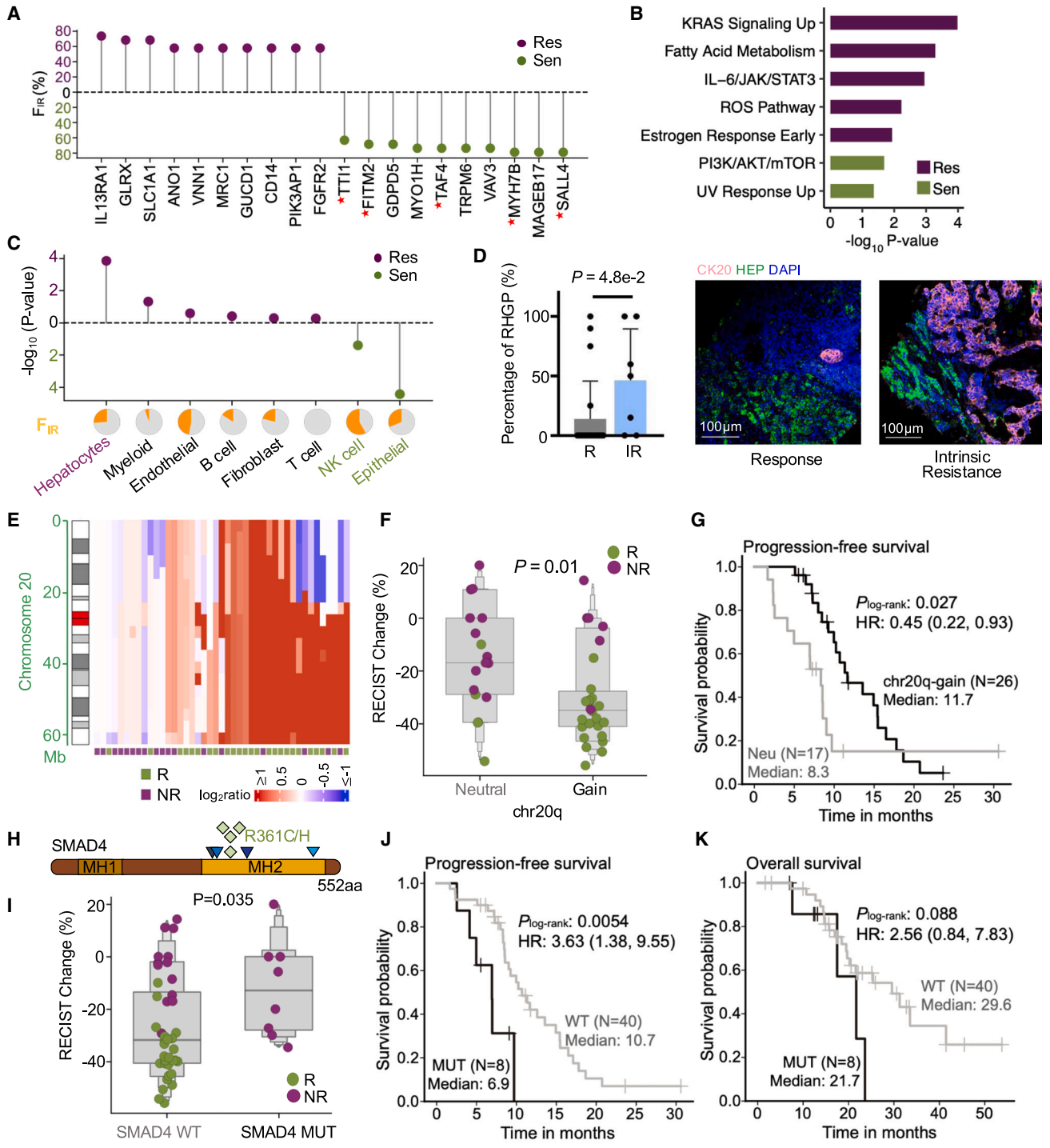

Figure 4. Genomic and transcriptomic factors associated to IR

(A) Lollipop plot showing the top 10 genes related to IR. The y axis represents the proportion of patients whose IR might be driven by the corresponding gene expression.

(B) The enriched hallmark gene sets from the significant IR-related genes in Figure 3A.

(C) Lollipop plot showing −log10 *p* values of the relevance of various cell types to IR, prioritized by SRFS. Pie charts (bottom) show the proportion of patients whose IR might be driven by the corresponding cell type.

(D) Comparison of the proportion of RHGP in responders ($n = 21$) and patients with IR ($n = 7$). A bar chart (left) and representative IF images (right) illustrate the proportion of RHGP. *p* value: Mann-Whitney U test. Scale bars, 100 μm.

(E) Chromosomal ideogram and heatmap, annotated with response status of first-line therapy, showing that chr20q-gain was frequently observed in responders.

(legend continued on next page)

the aforementioned DNA-level results of chromosome 20q-gain (Figures 4A and S7B). Furthermore, our analysis characterized immune-related factors such as *IL13RA1* (the receptor for interleukin 13), *MRC1*, and *CD14* (marker genes for myeloid cells), metabolism-related transcripts (*SLC1A1*, *CES1*, and *GUCD*1), and the stroma-related gene *FGFR2* as the top genes whose expression promote resistance. Functional enrichment analysis revealed that pro-sensitive IR-relevant genes were enriched in PI3K/AKT/mTOR signaling and UV response, while pro-resistant IR-relevant genes were enriched in KRAS signaling, fatty acid metabolism, and IL-6/JAK/STAT3 signaling (Figure 4B). Cellular-level analyses demonstrated that the post-treatment increase in hepatocytes was the most pronounced compared to other TME cell types, explaining 26.3% of IR (Figures 4C and S4D). We then proposed that the spatial distance between tumors and hepatocytes might be a determinant of IR. To provide further evidence to this hypothesis, mIF staining images were carefully examined and we found higher levels of RHGP in the IR group than in responsive patients, supporting that early hepatic infiltrates of tumors conferred IR to BVZ-C therapy (Figure 4D). Besides, myeloid cells were also highly enriched in the IR group (Figure S7C). Limited to the malignant RHGP tumors (n = 9), factors such as high tumor purity, CMS2 subtype, and relative abundance of epithelial and NK cells were still associated with a positive response. Additionally, mutations in TGF-β pathway, along with relative abundance of hepatocytes and myeloid cells were still identified as IR factors in RHGP tumors (Figure S7D). Regarding gene expression, no genes showed significant correlations with drug resistance, but due to the small RHGP sample size, validation of these findings in additional cohorts is warranted.

As the most significant pro-sensitive IR-relevant factor at the DNA level, gain/amplification of chromosomal region 20q (hereafter referred to as 20q-gain) was detected in 26 cases (60.5%). We confirmed a higher incidence of 20q-gain in responders (80%, 20/25) relative to non-responders (33.3%, 6/18) before therapy (Figure 4E), suggesting the 20q-gain as a positive predictor of treatment response. To investigate the prognostic value of 20q-gain, we examined the association between 20q copy-number status and clinical outcome. Patients whose tumors had 20q-gain exhibited a profound reduction in tumor size following treatment (Figure 4F) and significantly improved PFS (p = 2.7e−2, Figure 4G), with no stark difference observed in the OS (Figure S7E). To verify this observation, we extracted publicly available CNA data from 67 patients with CRLM treated with oxaliplatin and/or irinotecan plus BVZ.[28] As expected, 20q-gain was more frequent in the CR/PR group than in the SD/PD group (Figure S7F). Since CNAs may influence the genomic landscape of tumor cells and drive their evolution, we also explore whether 20q-gain is correlated to tumor cell plasticity. We conducted an analysis using the public CRC single-cell RNA-seq dataset (GSE132465[32]). Tumor cells were categorized into different CMS cell states, and the Shannon entropy index was used to measure the likelihood of tumor cell state transitions (Figure S7G). We revealed a significant increase in CMS2 tumor cells and lower cellular diversity in patients with 20q-gain, while those without 20q-gain showed greater intratumor heterogeneity and predominance of non-CMS2 subtypes. Hence, 20q-gain might be linked to BVZ-C responsiveness due to the enrichment of CMS2 tumor cells and reduced tumor cell plasticity, congruent with CMS subtype results (Figure 3A).

The *SMAD4* mutations stood out as the strongest genomic predictor of IR (Figure 3A). The mutation rate of *SMAD4* in this cohort was 16.3% (8/49). Four of the eight *SMAD4*-mutant cases (Figure 4H; Table S2) had recurrent hotspot mutations (R361H/C) in the MH2 domain involved in heterodimeric complex formation and transcriptional activation,[33] and the other four patients carried missense mutations in nearby regions. All were intrinsically unresponsive (Figure S2). It was recently reported that *SMAD4* loss in colon cancer cells is resistant to 5-FU and irinotecan.[34] However, loss of *SMAD4* did not distinguish responders from non-responders in our cohort (Figure S8A). In addition, the patient's IR response was not affected by the expression level of *SMAD4* (Figure S8A). Next, we examined the clinical relevance of *SMAD4* mutations. Remarkably, $SMAD4^{mutated}$ patients experienced a more significant increase in tumor size following treatment (p = 3.5e−2) and had materially worse survival outcomes (p = 5.4e−3 for PFS and 8.8e−2 for OS by log rank test) than $SMAD4^{wild\text{-}type}$ patients (Figures 4I–4K). Intrigued by these findings, we replicated this observation in an independent cohort of patients diagnosed with stage IV CRC from three Chinese centers and treated with BVZ-C therapy. Droplet digital PCR was performed to analyze the $SMAD4^{R361H}$ and $SMAD4^{R361C}$ mutations in primary or metastatic CRC tumor samples from these cases. Importantly, patients harboring $SMAD4^{R361H/C}$ mutation had significantly worse PFS (p = 0.02 by log rank test, Figure S8B) compared to those with $SMAD4^{wild\text{-}type}$, strengthening the prognostic value of *SMAD4* mutations in predicting resistance to BVZ-C therapy. We also verified this association in the published Chinese ChangKang[12] and MSK[10] CRC cohorts. Consistently, the R361H/C group had significantly worse OS (Chinese ChangKang: p = 9.8e−3, MSK: p = 8.6e−4) compared to the *SMAD4* wild-type group (Figures S8C and S8D). A similar tendency for PFS was also observed in the Chinese ChangKang cohort, although the result was insignificant (Figure S8C).

Furthermore, the *SMAD4* mutations were mutually exclusive with 20q-gain in pre-treatment samples (Figure S8E). We next examined the relationship between the IR-related genetic (*SMAD4* mutation and 20q-gain) and transcriptomic features (CMS subtype, cell type proportion, and gene expression). The CMS2 subtype showed a significant depletion in the *SMAD4*-mutant group but was markedly enriched in the 20q-gain group (Figures S8F and S8G). Additionally, the *SMAD4*-mutant group had a higher prevalence of the mixed subtype compared to

(F) Boxplot showing the association between RECIST changes and chr20q-gain. p value: two-sided Mann-Whitney U test.
(G) Kaplan-Meier estimates of PFS for patients segregated by chr20q-gain. p value: log rank test. HR: hazard ratio.
(H) Schematics of the protein structures showing the locations of *SMAD4* mutations. MH: Mad homology.
(I) The association between RECIST changes and *SMAD4* mutation. p value: two-sided Mann-Whitney U test.
(J and K) Kaplan-Meier estimates of PFS (J) and OS (K) for patients segregated by $SMAD4^{mutated}$. p value: log rank test. See also Figures S7–S9.

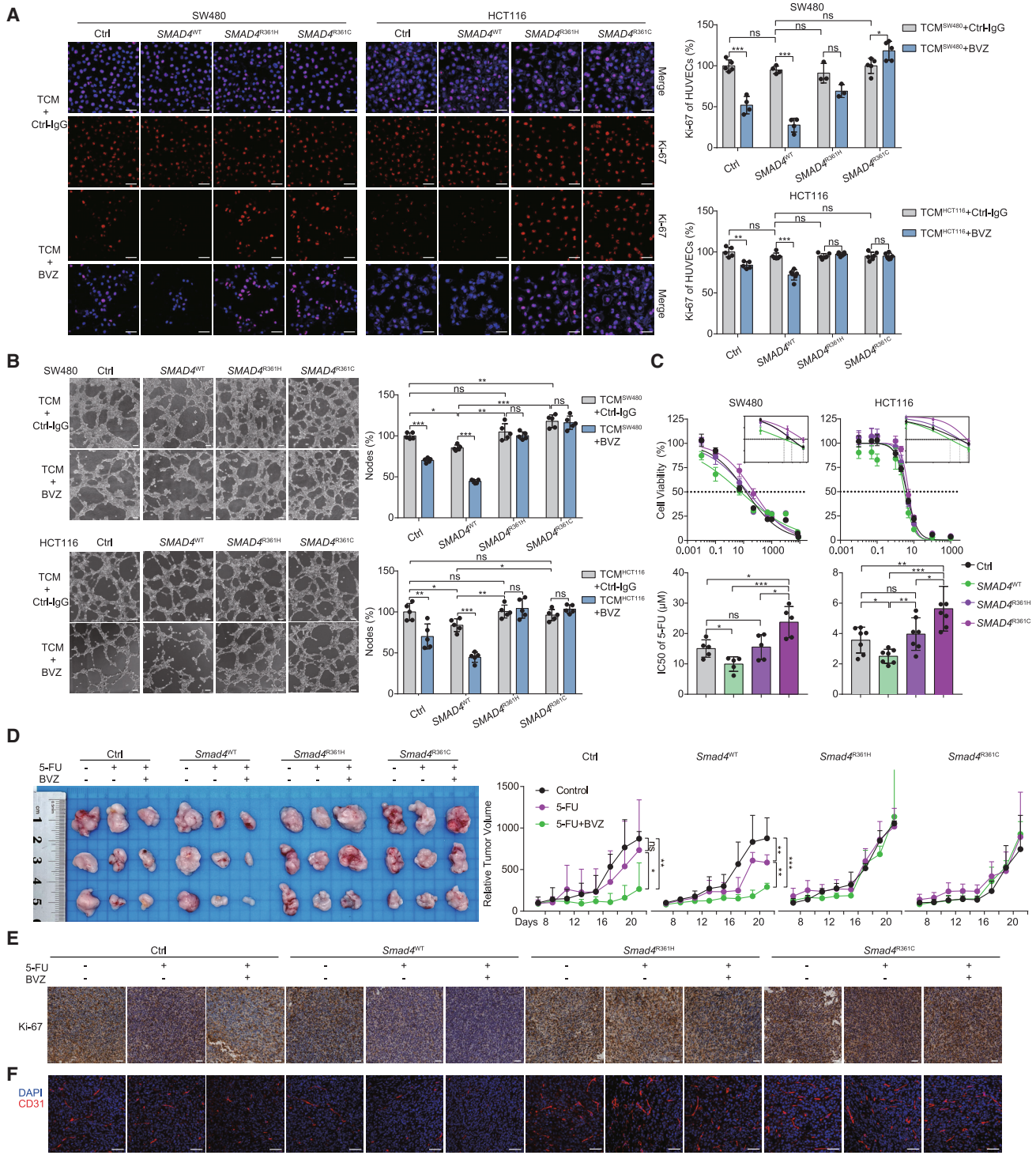

Figure 5. *SMAD4*$^{R361H/C}$ mutations promote 5-FU and BVZ resistance in CRC

(A) IF staining for Ki-67 (red) and DAPI (blue) in HUVECs incubated with tumor conditioned medium (TCM) collected from the indicated cells and BVZ (0.25 mg/mL). Representative IF images (left) and the quantification (right) of mean fluorescence intensity (MFI) are shown (n = 4–5). Scale bar, 100 μm.

(B) Representative images (left) and quantification (right) of the formation of HUVECs tubules following incubation with TCM and treatment with BVZ (n = 4–5). Scale bar, 100 μm.

(C) Cell viability assay of SW480 and HCT116 cells following treatment with 5-FU for 48 h, IC50 value of 5-FU (bottom) and representative curve-fitting graphs (top) are shown (n = 5, 7).

(legend continued on next page)

wild type, indicating that *SMAD4*-mutant tumors may have greater intratumoral heterogeneity. No significant association was identified between the two genomic features and TME pro-sensitive (epithelial and NK cells) or pro-resistant (hepatocytes) cell types, but the *SMAD4*-mutant samples were distinguished by a higher proportion of endothelial and myeloid cells compared to wild type. Moreover, most pro-sensitive genes were upregulated in the 20q-gain group but downregulated in the *SMAD4*-mutant group, while pro-resistant genes showed the opposite trend, suggesting a strong concordance between genomic and transcriptomic response-related features. Compared with non-mutants, tumors with mutations in *SMAD4* exhibited higher expression of metabolism (glucose transporter *SLC1A1*) and angiogenesis (vascular endothelial growth factor [VEGF] and semaphorin co-receptor *NRP1*)-associated genes. Concurrently, the elevated expression of myeloid markers (*MRC1* and *CD14*) was observed, implying an increased myeloid cell infiltration in *SMAD4*-mutant tumors. In contrast, tumors harboring 20q-gain displayed strong upregulation of pro-sensitive genes on chromosome 20q. Taken together, *SMAD4* mutations and 20q-gain might contribute to intrinsic drug resistance and sensitivity, respectively; and 20q-gain associated with the CMS2 subtype, whereas *SMAD4* mutations associated with increased myeloid cell infiltration and the mixed CMS subtype.

To extend our findings into practical clinical applications, we utilized the identified resistance-related features to train a machine learning model (Figure S9A), which could assist in the early prediction of drug resistance in patients with CRLM. The model achieved an area under the receiver operating characteristic curve of 0.82 and effectively distinguished responders versus non-responders (Figures S9B and S9C). Notably, the key sensitive determinants in the model included *TAF4* and *TRPM6* expression and chr20q-gain (Figure S9D). *TAF4*, involved in transcription initiation, was previously linked to the maintenance of stem cell function.[35] The top resistant informative features included the expression levels of *SLC1A1*, *FGFR2*, and *ANO1* (Figure S9D). *SLC1A1* was reported to be overexpressed in oxaliplatin-resistant CRCs.[36] *FGFR2* was a fibroblast growth factor receptor (FGFR), and prior studies have associated fibroblast growth factors and FGFRs with resistance to multiple cytotoxic agents, like cisplatin, tamoxifen, 5-FU, and BVZ.[37] *ANO1* was found to be associated with CRC progression.[38] These evidence together supported that our model could be a useful tool for forecasting drug response to optimize the treatment and benefit patients in the clinic.

SMAD4$^{R361\ H/C}$ induces resistance to BVZ and 5-FU *in vitro* and *in vivo*

To experimentally gauge the biological effect of *SMAD4* mutations, we used the human CRC cell lines SW480 (SMAD4 negative) and HCT116 (SMAD4 positive and wild type), which were transduced with retroviral constructs expressing either *SMAD4* wild-type or point mutations at the arginine 361 residue (R361) and containing an N-terminal FLAG tag (Figure S10A). We first explored the influence of *SMAD4*$^{R361H/C}$ mutations on BVZ treatment efficacy *in vitro*. The human umbilical vein endothelial cells (HUVECs) were incubated with tumor conditioned medium (TCM), which was derived from *SMAD4*-transduced tumor cells. After 48 h of culturing, we measured the changes in cell proliferation and tubular formation of HUVECs. Notably, immunofluorescence (IF) staining in HUVECs revealed unchanged or even higher expression levels of Ki-67 in *SMAD4*$^{R361H/C}$ groups after BVZ treatment, in contrast to the decreased expression in the control and wild-type groups (Figure 5A). Moreover, tube formation experiments showed that BVZ treatment significantly reduced the number of nodes in the control and wild-type groups; however, no changes were observed in the *SMAD4*$^{R361H/C}$ group (Figure 5B). In brief, these results suggested that *SMAD4*$^{R361H/C}$ tumors induced resistance to BVZ. Next, we focused on the common chemotherapeutic agents, mFOLFOX6 and FOLFIRI. Transfected SW480 and HCT116 cells were treated with increasing concentrations of 5-FU, irinotecan, or oxaliplatin (Figures 5C and S10B). Judging by the IC50 (half-maximal inhibitory concentration) values, the control cells were less sensitive to 5-FU and irinotecan relative to *SMAD4*^{WT} cells, while there was no difference in response to oxaliplatin, in agreement with a previous report on drug resistance of *SMAD4* loss.[34] Importantly, compared to *SMAD4*^{WT} cells, *SMAD4*$^{R361H/C}$ tumor cells were markedly resistant to 5-FU, but not to irinotecan or oxaliplatin (Figures 5C and S10B), which was further confirmed by colony formation and apoptosis assays (Figures S10C and S10D). Taken together, these results demonstrated that *SMAD4*$^{R361H/C}$ conferred *in vitro* resistance to BVZ and 5-FU.

To extend these findings *in vivo*, we transduced murine CT26 cells with *Smad4*^{WT} or *Smad4*$^{R361H/C}$ constructs and subcutaneously injected them into BALB/c mice, followed by treatment with 5-FU and monoclonal BVZ (B20.4–1.1, anti-VEGF antibody). In the control and *Smad4*^{WT} groups, 5-FU or 5-FU plus BVZ treatment significantly improved tumor growth inhibition compared to PBS treatment, whereas tumor volume showed no change in the *Smad4*$^{R361H/C}$ groups receiving the same therapies (Figure 5D). Similar results were obtained using immunohistochemical staining for Ki-67 (Figures 5E and S10E). Additionally, CD31-marked tumor vessels showed a remarkably decreased density in the control and *Smad4*^{WT} groups after treatment, especially with 5-FU plus BVZ, but no significant trend was found in the *Smad4*$^{R361H/C}$ groups (Figures 5F and S10E). Collectively, these findings provided compelling evidence of *in vivo* resistance to BVZ and 5-FU in *SMAD4*$^{R361H/C}$-harboring CRC tumors.

GB201 combination treatment ameliorates resistance in *SMAD4*$^{R361\ H/C}$ CRCs

Next, we sought to identify the potential mechanisms underlying BVZ and 5-FU resistance induced by *SMAD4* mutations. To this

(D) Stably transfected CT26 cells were subcutaneously injected in BALB/c mice. Mice were treated with PBS, 5-FU (25 mg/kg), or 5-FU (25 mg/kg, twice a week) combined with monoclonal BVZ (B20.4-1.1, 5 mg/kg, twice a week). Representative images (left) and tumor growth curve (right) are shown ($n = 3$).
(E and F) Transplanted subcutaneous tumors with treatment are collected for immunohistochemical staining of Ki-67 (E) and immunofluorescence of vascular marker CD31 (F); blue: DAPI, red: CD31. Scale bar, 100 μm. Data are graphed as the mean ± SD; *, $p < 0.05$; **, $p < 0.01$; ***, $p < 0.001$; ns, non-significant, $p > 0.05$. See also Figure S10.

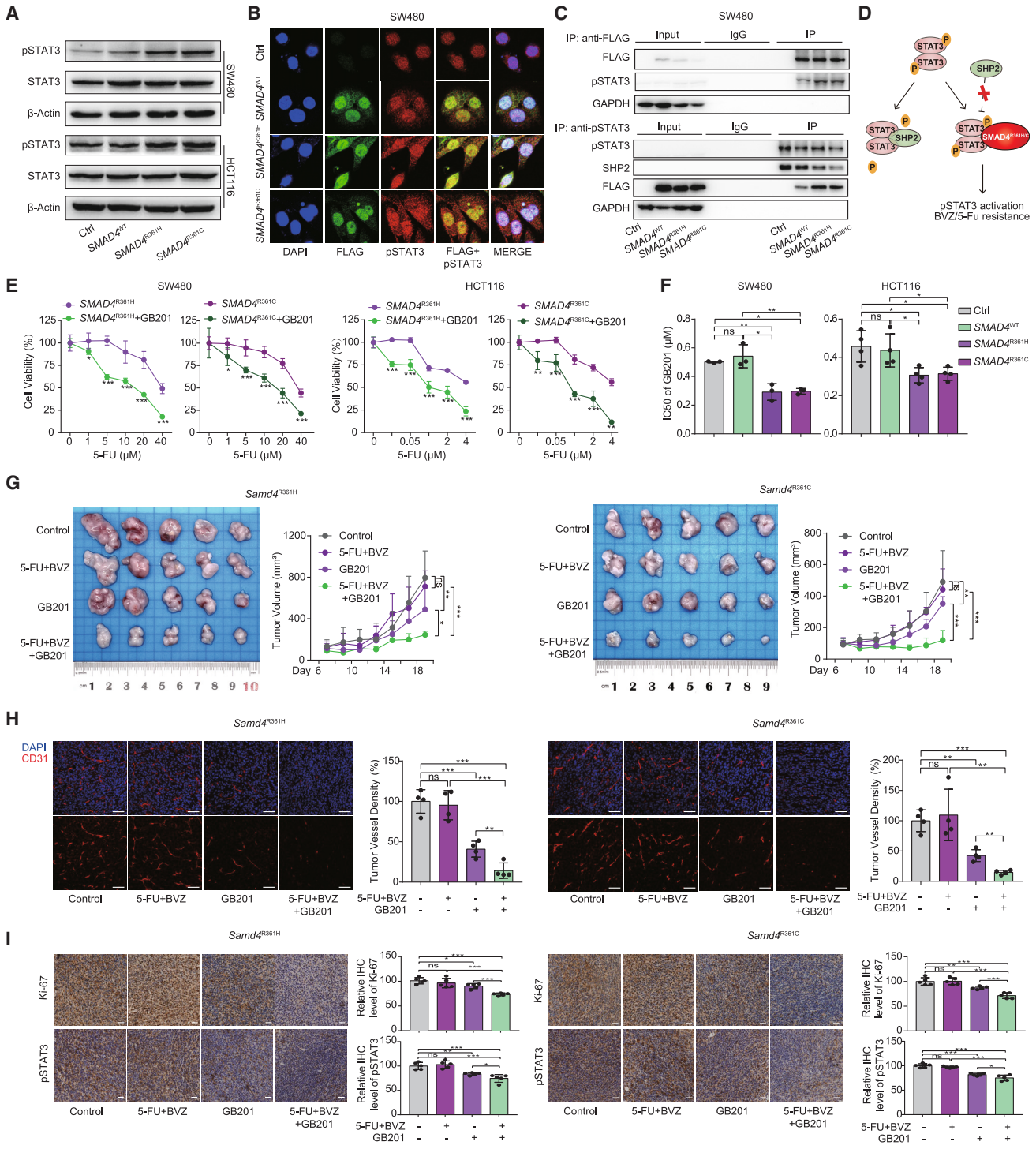

Figure 6. GB201 can target *SMAD4*$^{R361H/C}$ mutation-mediated activation of the pSTAT3 pathway to reverse resistance in CRC

(A) Western blot analysis of pSTAT3 protein in SW480 and HCT116 cells.

(B) IF staining for FLAG-labeled SMAD4 protein (green), pSTAT3 protein (red), and DAPI (blue) in SW480. Scale bar, 100 μm.

(C) Co-IP assay shows a complex containing pSTAT3 and FLAG-SMAD4^{R361H}, SMAD4^{R361C}, or SHP2 in SW480 cells. Top, FLAG antibody co-precipitating pSTAT3. Bottom, pSTAT3 antibody co-precipitating FLAG-SMAD4^{R361H}, SMAD4^{R361C}, or SHP2 protein. Input, protein expression in cell lysates detected by western blot. IgG, negative control. IP, expression of compound co-precipitated by pSTAT3 or FLAG antibody.

(D) Schematic diagram of SMAD4$^{R361H/C}$ protein activating pSTAT3 through competitive binding with SHP2.

(E) Cell viability of SW480 and HCT116 cells with *SMAD4*$^{R361H/C}$ exposed to 5-FU at the gradient concentrations, with or without combination with GB201.

(legend continued on next page)

end, we conducted GSEA comparing pre-treatment RNA samples with and without *SMAD4* mutations. GSEA revealed that the inflammatory response and TNFA signaling via NF-κB, IL-2-STAT5, and IL-6-STAT3 were enriched in *SMAD4*-mutant samples (Figure S11A). Based on this, three inhibitors, JSH-23 (NF-κB inhibitor), AC-4-130 (STAT5 inhibitor), and STATTIC (STAT3 inhibitor), were tested in CRC cell lines; the IC50 values showed that mutant cells were more sensitive to the STAT3 inhibitor, highlighting the importance of STAT3 signaling in $SMAD4^{R361H/C}$ tumor resistance (Figure S11B). Western blotting (WB, Figure 6A) and IF staining (Figure 6B) of pSTAT3 together confirmed the elevated phosphorylated STAT3 in $SMAD4^{R361H/C}$ cells. Co-immunoprecipitation (Co-IP) experiments were conducted to examine functional connections. Intriguingly, $SMAD4^{R361H/C}$ mutations bound to the pSTAT3 protein and impeded its interaction with tyrosine phosphatase SHP2, protecting pSTAT3 from dephosphorylation (Figures 6C and S11C). This mechanism resembles that observed in p53 mutations.[39] Thus, our data showed that $SMAD4^{R361H/C}$ mutation could hyperactivate STAT3 through competitive displacement of SHP2 (Figure 6D).

To further understand the mechanism of BVZ resistance, we re-examined the DEGs in *SMAD4*-mutant versus *SMAD4*-WT CRLM samples. The results revealed a significant upregulation of several chemokines in the inflammatory response pathway, such as *CCL2*, *CCL7*, and *CCL22*, in *SMAD4*-mutant samples, with qPCR assays further confirming the upregulation of *CCL2* in $SMAD4^{R361H/C}$ CRC cell lines (Figures S11D and S11E). This led us to speculate that CCL2 may be involved in BVZ resistance. Next, we knocked down *STAT3* in $SMAD4^{R361H/C}$ tumor cells using small interfering RNA and collected their tumor culture supernatant after 48 h to stimulate HUVECs (Figures S11F–S11I). STAT3 knockdown in tumor cells inhibited endothelial cell proliferation and tube formation, effectively attenuating $SMAD4^{R361H/C}$-induced BVZ resistance. Conversely, exogenous addition of CCL2 enhanced cell proliferation and tube formation to restore BVZ resistance. These data substantiated that $SMAD4^{R361\ H/C}$ might induce resistance to BVZ in CRC via the pSTAT3-CCL2 axis.

Given the crucial role of STAT3 signaling in $SMAD4^{R361H/C}$ CRC, we used STATTIC and GB201 (both STAT3 inhibitors) in combination with 5-FU to explore combinatorial treatment efficacy through drug-sensitive experiments. In contrast to STATTIC, GB201 significantly reduced 5-FU resistance (Figures 6E, 6F, and S11J). WB experiments further confirmed the notable inhibitory effect of GB201 on the pSTAT3-CCL2 axis (Figure S11K). Therefore, we established *Smad4*-mutant CRC animal models and administered them with single-agent GB201, doublet therapy (BVZ and 5-FU), and triplet therapy (BVZ, 5-FU, and GB201). The results showed that GB201 effectively restored sensitivity to BVZ and 5-FU in $Smad4^{R361H/C}$ groups (Figure 6G), with a three-drug combination significantly abating tumor vessels and proliferation (Figures 6H and 6I). Based on the upregulation of STAT3 signaling in $SMAD4^{R361H/C}$ tumors, we proposed the addition of GB201 to BVZ-C therapies as a novel drug repurposing strategy to overcome therapeutic resistance in $SMAD4^{R361H/C}$ CRC.

DISCUSSION

Here, we gathered a large cohort of multi-time point samples to study in-depth tumor and microenvironment evolution in patients with CRLM before and after BVZ-C therapy. Previous studies have shown that secondary drug resistance is often heterogeneous, possibly due to polyclonal and multiple selection patterns.[40] In contrast, we found that 92% of patients exhibited linear tumor evolution under treatment, with only four cases acquiring notable mutations post treatment. Moreover, high similarities were observed in the tumor expression profiles after treatment. Thus, tumor clonal selection is not the major mechanism behind AR to BVZ-C, rendering the targeting of clonal subpopulations an unviable approach to counteract AR. Phenotypic plasticity, or non-genetic reprogramming, has been listed as one of the 14 hallmarks of malignancy[41] and is another critical determinant in mediating tumor drug resistance.[42] Transcriptional analyses revealed a dramatic increase in hepatocyte and myeloid cell composition after therapy, indicating that reprogramming of microenvironmental cells, rather than tumor cells, may be the primary driving force behind secondary resistance.

Next, we screened AR- and IR-related features using the SRFS method. Interestingly, increased hepatic infiltration of tumor cells not only predicts primary non-response to BVZ-C but also correlates with disease progression, suggesting the potential enhancement of hepatocyte-tumor cell interactions under treatment. Combining the histopathological, immunofluorescence, and CT data of clinical patients, we found that the RHGP largely contributed to IR and AR to BVZ-C therapy, consistent with previous findings.[17,18] The liver is highly vascularized, and drug resistance in RHGP-type CRLMs is often associated with vascular co-option, in which cancer cells can infiltrate the hepatic plate of the liver parenchyma and absorb pre-existing hepatic sinusoidal vessels.[30] Therefore, co-targeting angiogenesis and vascular co-option is expected to be the key to reversing drug resistance in patients with CRLM; however, the underlying molecular mechanisms require further investigation.

The SRFS method revealed two predictive markers for IR: (1) 20q-gain with favorable response and (2) *SMAD4* mutation with unfavorable response. The 20q-gain showed the CMS2 tumor cell predominance and was related to reduced intratumor

(F) IC50 value of SW480 and HCT116 cells with $SMAD4^{R361H/C}$ exposed to GB201 is shown (n = 3, 4).
(G) Stably transfected CT26 cells with $Smad4^{R361H/C}$ were subcutaneously injected in BALB/c mice. Mice were treated with PBS, 5-FU (25 mg/kg, twice a week) combined with monoclonal BVZ (5 mg/kg, twice a week), GB201 (10 mg/kg, q2d), and three-drug combination for 2 weeks. Representative images (left) and tumor growth curve (right) of transplanted subcutaneous tumors of CT26 cells with $Smad4^{R361H/C}$ are shown (n = 5).
(H) Transplanted subcutaneous tumors with treatment and $Smad4^{R361H/C}$ are collected for IF staining of CD31, representative IF images and the quantification are shown; blue: DAPI, red: CD31. Scale bar, 100 μm.
(I) Representative immunohistochemical staining for Ki-67 and pSTAT3 and their quantification of xenograft tumor with $Smad4^{R361H/C}$ mutations. Scale bar, 100 μm. See also Figure S11.

heterogeneity. According to previous reports, chr20q amplification is related to the immune-cold microenvironment in CRC[43] and lymph node metastasis in breast cancer.[44] Therefore, CRC with or without 20q-gain may be suitable for different treatment options. 20q-gain tumors could potentially benefit from targeted combination chemotherapy, whereas immunotherapy or drugs such as tipifarnib, mitomycin-C, and AUY922[43] may hold promise for 20q-neutral tumors. *SMAD4* is a key component of the TGF-β pathway, and its mutations often lead to selective elimination of the anti-tumor effect of TGF-β, thereby promoting tumor growth and progression.[45] *SMAD4* mutations have been reported to occur in approximately 8.6% of CRC cases,[46] are more common in patients with stage IV and CMS3 subtypes,[47] and are associated with worse OS and disease-free survival.[48] A few studies have revealed correlations between *SMAD4* loss and 5-FU[49] or cetuximab resistance.[50,51] In this study, we found that *SMAD4*$^{R361H/C}$ mutation mediated BVZ and 5-FU cross-resistance in CRC cells through *in vivo* and *in vitro* experiments but had no impact on sensitivity to oxaliplatin and irinotecan. In addition, *SMAD4*^{R361C} exhibited greater 5-FU resistance than *SMAD4*^{R361H} *in vitro*, but this difference was not observed in mouse models. Previously, the biological function of *SMAD4*-mutant protein was rarely reported, and its understanding was limited to cell cycle disorder and apoptosis caused by *SMAD4* protein inactivation.[52] We proved that *SMAD4*$^{R361H/C}$ can activate the pSTAT3 pathway to mediate BVZ and 5-FU cross-resistance through the competitive combination of pSTAT3 and SHP2, as well as activate pSTAT3-CCL2 axis (pro-vascular redundancy signal) to mediate BVZ resistance.

The STAT3 pathway has been widely reported to play a role in regulating the expression of various chemokines and cytokines.[53] Prior research also suggested that STAT3 can directly bind the promoter of CCL2, thereby activating its transcription and expression in CRC.[54] Our investigation further elucidated that the *SMAD4*$^{R361H/C}$ led to the activation of STAT3, which induced the secretion of CCL2. Additionally, CCL2 can enhance inflammatory responses by recruiting myeloid cells into TME, and it can also promote STAT3 phosphorylation.[55,56] Together, the *SMAD4*$^{R361H/C}$ augmented the expression of inflammatory chemokines such as CCL2 by activating STAT3, and STAT3-CCL2 regulatory relationship could further stimulate inflammation in TME. GB201 (also known as napabucasin or BB608) is the only STAT3 inhibitor that has entered phase 3 clinical trials. In 2016, the FDA approved GB201 for the treatment of gastric cancer[57] and pancreatic cancer[58]; subsequent phase 3 trials failed. The results of a phase 3 clinical trial (NCT01830621) of patients with CRC also showed no difference in OS between the GB201 and placebo groups.[59] However, subgroup analysis showed that GB201 significantly benefited the high pSTAT3 expression subgroup.[59] Our experiments showed that pSTAT3 was significantly activated in *SMAD4*$^{R361H/C}$ CRC, and GB201 combined with 5-FU and BVZ significantly inhibited the growth of *SMAD4*$^{R361H/C}$ CRC, indicating the importance of patient screening as a crucial breakthrough for effective GB201 treatment.

Here, our study identified hepatocyte-tumor spatial proximity and increased myeloid cell infiltration, rather than clonal selection and transcriptional reprogramming of tumor cells, as the primary causes of resistance to BVZ-C therapy in CRLMs. Importantly, we demonstrated that *SMAD4*$^{R361H/C}$ serves as a genomic marker, which provides a stratification basis and therapeutic target for the first-line therapy of CRC, and GB201 combination therapy is expected to reverse BVZ-C therapeutic resistance. Finally, we summarized the BVZ-C response-associated features as well as the well-known factors[13,30,39,54–56,60–65] as a diagram to connect the different feature categories (Figure S12).

Limitations of the study

There are some limitations to our study. Although our large cohort of multi-time point samples enabled the study of IR and AR to BVZ-C therapy, independent multi-source studies are needed to validate the predictive role of the identified response-related factors. In addition, the association between AR and spatial proximity of hepatocytes or myeloid cells to tumors cannot be investigated via the bulk transcriptomic data, and the longitudinal spatial transcriptomics should be included to further evaluate the spatial and architectural features.

RESOURCE AVAILABILITY

Lead contact

Further information and requests for resources and data should be directed to and will be fulfilled by the lead contact, Wangjun Liao (liaowj@smu.edu.cn).

Materials availability

All materials used in this paper are available from the lead contact upon request.

Data and code availability

- The raw sequence data were deposited in the Genome Sequence Archive at the National Genomics Data Center, under the accession code GSA: HRA005455.
- All code has been deposited in Zenodo and can be accessed at https://doi.org/10.5281/zenodo.13997442.
- Any additional information required to reanalyze the data reported in this paper is available from the lead contact upon request.

ACKNOWLEDGMENTS

This study was supported by grants from Guangdong Province Science and Technology Plan Project (no. 2020A0505090007) and the Guangdong Basic and Applied Basic Research Foundation (no. 2022A1515011693), the Seed fund of the Big Data for Bio-Intelligence Laboratory (Z0428) from HKUST, Hong Kong Research Grant Council (16101021, R4017-18, and C4008-23W), and Hong Kong Innovation and Technology Commission (ITCPD/17-9). Jiguang Wang was also supported by the Padma Harilela Professorship.

AUTHOR CONTRIBUTIONS

Conceptualization, W.L. and Jiguang Wang; computational analyses, Y.Y., with help from D.Z., Z.M., X.Z., R.L., Q.M., H.S., and J.T.; experiments, M.S., Jiao Wang, Z. Wang, J.C., and G.H.; surgery, W.L., M.S., N.H., C.W., X.R., and Z. Wu; data curation, G.H., Y.G., D.Z., and J.G.; writing – original draft, Y.Y., N.H., and Q.H.; writing – review and editing, Y.Y., Q.H., D.Z., Z.M., and Jiguang Wang.

DECLARATION OF INTERESTS

The authors declare no competing interests.

STAR★METHODS

Detailed methods are provided in the online version of this paper and include the following:

- KEY RESOURCES TABLE
- EXPERIMENTAL MODEL AND STUDY PARTICIPANT DETAILS
  - Clinical sample acquisition and treatment response evaluation
  - Cell lines
  - Animals
- METHOD DETAILS
  - DNA extraction and library construction
  - Somatic mutation detection
  - Somatic copy number alteration
  - Microsatellite instability prediction
  - Evolutionary tree
  - RNA extraction and library construction
  - Bulk RNA-seq preprocessing
  - Differential gene expression analysis, pathway analysis and gene set enrichment
  - Sample-based response feature selection
  - Bulk transcriptional subtype classification
  - Deconvolution analysis
  - Spatial transcriptomic data analysis
  - Machine learning model
  - Antibodies
  - Chemicals
  - Scoring of morphological response to therapy
  - Tumor conditioned medium
  - Cell tubule formation
  - Cell viability assay
  - Western blotting
  - RNA isolation and quantitative PCR analysis
  - Colony formation
  - Cell apoptosis
  - Immunofluorescence staining
  - Immunohistochemistry staining
  - Co-IP analysis
  - siRNA transfection
- QUANTIFICATION AND STATISTICAL ANALYSIS

SUPPLEMENTAL INFORMATION

Supplemental information can be found online at https://doi.org/10.1016/j.xcrm.2024.101838.

Received: May 17, 2024
Revised: September 16, 2024
Accepted: November 4, 2024
Published: December 3, 2024

REFERENCES

1. Wang, R., Li, J., Zhou, X., Mao, Y., Wang, W., Gao, S., Wang, W., Gao, Y., Chen, K., Yu, S., et al. (2022). Single-cell genomic and transcriptomic landscapes of primary and metastatic colorectal cancer tumors. Genome Med. *14*, 93.
2. Hurwitz, H., Fehrenbacher, L., Novotny, W., Cartwright, T., Hainsworth, J., Heim, W., Berlin, J., Baron, A., Griffing, S., Holmgren, E., et al. (2004). Bevacizumab plus irinotecan, fluorouracil, and leucovorin for metastatic colorectal cancer. N. Engl. J. Med. *350*, 2335–2342.
3. Cremolini, C., Loupakis, F., Antoniotti, C., Lupi, C., Sensi, E., Lonardi, S., Mezi, S., Tomasello, G., Ronzoni, M., Zaniboni, A., et al. (2015). FOLFOXIRI plus bevacizumab versus FOLFIRI plus bevacizumab as first-line treatment of patients with metastatic colorectal cancer: updated overall survival and molecular subgroup analyses of the open-label, phase 3 TRIBE study. Lancet Oncol. *16*, 1306–1315.
4. Bennouna, J., Sastre, J., Arnold, D., Österlund, P., Greil, R., Van Cutsem, E., von Moos, R., Viéitez, J.M., Bouché, O., Borg, C., et al. (2013). Continuation of bevacizumab after first progression in metastatic colorectal cancer (ML18147): a randomised phase 3 trial. Lancet Oncol. *14*, 29–37.
5. Masi, G., Vivaldi, C., Fornaro, L., Lonardi, S., Buccianti, P., Sainato, A., Marcucci, L., Martignetti, A., Luca Urso, E.D., Castagna, M., et al. (2019). Total neoadjuvant approach with FOLFOXIRI plus bevacizumab followed by chemoradiotherapy plus bevacizumab in locally advanced rectal cancer: the TRUST trial. Eur. J. Cancer *110*, 32–41.
6. Simkens, L.H.J., van Tinteren, H., May, A., ten Tije, A.J., Creemers, G.J.M., Loosveld, O.J.L., de Jongh, F.E., Erdkamp, F.L.G., Erjavec, Z., van der Torren, A.M.E., et al. (2015). Maintenance treatment with capecitabine and bevacizumab in metastatic colorectal cancer (CAIRO3): a phase 3 randomised controlled trial of the Dutch Colorectal Cancer Group. Lancet *385*, 1843–1852.
7. Heinemann, V., von Weikersthal, L.F., Decker, T., Kiani, A., Kaiser, F., Al-Batran, S.E., Heintges, T., Lerchenmüller, C., Kahl, C., Seipelt, G., et al. (2021). FOLFIRI plus cetuximab or bevacizumab for advanced colorectal cancer: final survival and per-protocol analysis of FIRE-3, a randomised clinical trial. Br. J. Cancer *124*, 587–594.
8. Shen, Y., Wang, X., Lu, J., Salfenmoser, M., Wirsik, N.M., Schleussner, N., Imle, A., Freire Valls, A., Radhakrishnan, P., Liang, J., et al. (2020). Reduction of Liver Metastasis Stiffness Improves Response to Bevacizumab in Metastatic Colorectal Cancer. Cancer Cell *37*, 800–817.e7.
9. Cancer Genome Atlas Network (2012). Comprehensive molecular characterization of human colon and rectal cancer. Nature (London) *487*, 330–337.
10. Yaeger, R., Chatila, W.K., Lipsyc, M.D., Hechtman, J.F., Cercek, A., Sanchez-Vega, F., Jayakumaran, G., Middha, S., Zehir, A., Donoghue, M.T.A., et al. (2018). Clinical Sequencing Defines the Genomic Landscape of Metastatic Colorectal Cancer. Cancer Cell *33*, 125–136.e3.
11. Guinney, J., Dienstmann, R., Wang, X., de Reyniès, A., Schlicker, A., Soneson, C., Marisa, L., Roepman, P., Nyamundanda, G., Angelino, P., et al. (2015). The consensus molecular subtypes of colorectal cancer. Nat. Med. *21*, 1350–1356. https://doi.org/10.1038/nm.3967.
12. Zhao, Q., Wang, F., Chen, Y.X., Chen, S., Yao, Y.C., Zeng, Z.L., Jiang, T.J., Wang, Y.N., Wu, C.Y., Jing, Y., et al. (2022). Comprehensive profiling of 1015 patients' exomes reveals genomic-clinical associations in colorectal cancer. Nat. Commun. *13*, 2342. https://doi.org/10.1038/s41467-022-30062-8.
13. Smeets, D., Miller, I.S., O'Connor, D.P., Das, S., Moran, B., Boeckx, B., Gaiser, T., Betge, J., Barat, A., Klinger, R., et al. (2018). Copy number load predicts outcome of metastatic colorectal cancer patients receiving bevacizumab combination therapy. Nat. Commun. *9*, 4112.
14. Woolston, A., Khan, K., Spain, G., Barber, L.J., Griffiths, B., Gonzalez-Exposito, R., Hornsteiner, L., Punta, M., Patil, Y., Newey, A., et al. (2019). Genomic and Transcriptomic Determinants of Therapy Resistance and Immune Landscape Evolution during Anti-EGFR Treatment in Colorectal Cancer. Cancer Cell *36*, 35–50.e9. https://doi.org/10.1016/j.ccell.2019.05.013.
15. Kim, C., Gao, R., Sei, E., Brandt, R., Hartman, J., Hatschek, T., Crosetto, N., Foukakis, T., and Navin, N.E. (2018). Chemoresistance Evolution in Triple-Negative Breast Cancer Delineated by Single-Cell Sequencing. Cell *173*, 879–893.e13.
16. Marine, J.C., Dawson, S.J., and Dawson, M.A. (2020). Non-genetic mechanisms of therapeutic resistance in cancer. Nat. Rev. Cancer *20*, 743–756.
17. Huang, M., Lin, Y., Wang, C., Deng, L., Chen, M., Assaraf, Y.G., Chen, Z.S., Ye, W., and Zhang, D. (2022). New insights into antiangiogenic therapy resistance in cancer: Mechanisms and therapeutic aspects. Drug Resist. Updates *64*, 100849.

18. Qi, M., Fan, S., Huang, M., Pan, J., Li, Y., Miao, Q., Lyu, W., Li, X., Deng, L., Qiu, S., et al. (2022). Targeting FAPα-expressing hepatic stellate cells overcomes resistance to antiangiogenics in colorectal cancer liver metastasis models. J. Clin. Invest. *132*.

19. Eisenhauer, E.A., Therasse, P., Bogaerts, J., Schwartz, L.H., Sargent, D., Ford, R., Dancey, J., Arbuck, S., Gwyther, S., Mooney, M., et al. (2009). New response evaluation criteria in solid tumours: Revised RECIST guideline (version 1.1). Eur. J. Cancer *45*, 228–247.

20. Parikh, A.R., Lee, F.-C., Yau, L., Koh, H., Knost, J., Mitchell, E.P., Bosanac, I., Choong, N., Scappaticci, F., Mancao, C., and Lenz, H.-J. (2019). MAVERICC, a Randomized, Biomarker-stratified, Phase II Study of mFOLFOX6-Bevacizumab versus FOLFIRI-Bevacizumab as First-line Chemotherapy in Metastatic Colorectal Cancer. Clin. Cancer Res. *25*, 2988–2995.

21. Turner, N.C., and Reis-Filho, J.S. (2012). Genetic heterogeneity and cancer drug resistance. Lancet Oncol. *13*, e178–e185.

22. Lippert, T.H., Ruoff, H.J., and Volm, M. (2008). Intrinsic and acquired drug resistance in malignant tumors. The main reason for therapeutic failure. Arzneimittelforschung *58*, 261–264.

23. Li, C., Sun, Y.D., Yu, G.Y., Cui, J.R., Lou, Z., Zhang, H., Huang, Y., Bai, C.G., Deng, L.L., Liu, P., et al. (2020). Integrated Omics of Metastatic Colorectal Cancer. Cancer Cell *38*, 734–747.e9.

24. Jiang, B., Song, D., Mu, Q., and Wang, J.J.Q.B. (2020). CELLO: a longitudinal data analysis toolbox untangling cancer evolution. Quantitative Biology *8*, 256–266.

25. van Dijk, E., van den Bosch, T., Lenos, K.J., El Makrini, K., Nijman, L.E., van Essen, H.F.B., Lansu, N., Boekhout, M., Hageman, J.H., Fitzgerald, R.C., et al. (2021). Chromosomal copy number heterogeneity predicts survival rates across cancers. Nat. Commun. *12*, 3188. https://doi.org/10.1038/s41467-021-23384-6.

26. Chu, T., Wang, Z., Pe'er, D., and Danko, C.G. (2022). Cell type and gene expression deconvolution with BayesPrism enables Bayesian integrative analysis across bulk and single-cell RNA sequencing in oncology. Nat. Can. (Ott.) *3*, 505–517. https://doi.org/10.1038/s43018-022-00356-3.

27. Sathe, A., Mason, K., Grimes, S.M., Zhou, Z., Lau, B.T., Bai, X., Su, A., Tan, X., Lee, H., Suarez, C.J., et al. (2023). Colorectal Cancer Metastases in the Liver Establish Immunosuppressive Spatial Networking between Tumor-Associated SPP1+ Macrophages and Fibroblasts. Clin. Cancer Res. *29*, 244–260. https://doi.org/10.1158/1078-0432.Ccr-22-2041.

28. Gambaro, K., Marques, M., McNamara, S., Couetoux du Tertre, M., Diaz, Z., Hoffert, C., Srivastava, A., Hébert, S., Samson, B., Lespérance, B., et al. (2021). Copy number and transcriptome alterations associated with metastatic lesion response to treatment in colorectal cancer. Clin. Transl. Med. *11*, e401.

29. Wu, Y., Yang, S., Ma, J., Chen, Z., Song, G., Rao, D., Cheng, Y., Huang, S., Liu, Y., Jiang, S., et al. (2022). Spatiotemporal Immune Landscape of Colorectal Cancer Liver Metastasis at Single-Cell Level. Cancer Discov. *12*, 134–153. https://doi.org/10.1158/2159-8290.Cd-21-0316.

30. Frentzas, S., Simoneau, E., Bridgeman, V.L., Vermeulen, P.B., Foo, S., Kostaras, E., Nathan, M., Wotherspoon, A., Gao, Z.H., Shi, Y., et al. (2016). Vessel co-option mediates resistance to anti-angiogenic therapy in liver metastases. Nat. Med. *22*, 1294–1302.

31. Chun, Y.S., Vauthey, J.N., Boonsirikamchai, P., Maru, D.M., Kopetz, S., Palavecino, M., Curley, S.A., Abdalla, E.K., Kaur, H., Charnsangavej, C., and Loyer, E.M. (2009). Association of computed tomography morphologic criteria with pathologic response and survival in patients treated with bevacizumab for colorectal liver metastases. JAMA *302*, 2338–2344. https://doi.org/10.1001/jama.2009.1755.

32. Lee, H.O., Hong, Y., Etlioglu, H.E., Cho, Y.B., Pomella, V., Van den Bosch, B., Vanhecke, J., Verbandt, S., Hong, H., Min, J.W., et al. (2020). Lineage-dependent gene expression programs influence the immune landscape of colorectal cancer. Nat. Genet. *52*, 594–603. https://doi.org/10.1038/s41588-020-0636-z.

33. Lanauze, C.B., Sehgal, P., Hayer, K., Torres-Diz, M., Pippin, J.A., Grant, S.F.A., and Thomas-Tikhonenko, A. (2021). Colorectal Cancer-Associated Smad4 R361 Hotspot Mutations Boost Wnt/β-Catenin Signaling through Enhanced Smad4–LEF1 Binding. Mol. Cancer Res. *19*, 823–833.

34. Wong, C.K., Lambert, A.W., Ozturk, S., Papageorgis, P., Lopez, D., Shen, N., Sen, Z., Abdolmaleky, H.M., Győrffy, B., Feng, H., and Thiagalingam, S. (2020). Targeting RICTOR Sensitizes SMAD4-Negative Colon Cancer to Irinotecan. Mol. Cancer Res. *18*, 414–423.

35. Säisä-Borreill, S., Davidson, G., Kleiber, T., Thevenot, A., Martin, E., Mondot, S., Blottiere, H., Helleux, A., Mengus, G., Plateroti, M., et al. (2023). General transcription factor TAF4 antagonizes epigenetic silencing by Polycomb to maintain intestine stem cell functions. Cell Death Differ. *30*, 839–853. https://doi.org/10.1038/s41418-022-01109-6.

36. Pedraz-Cuesta, E., Christensen, S., Jensen, A.A., Jensen, N.F., Bunch, L., Romer, M.U., Brünner, N., Stenvang, J., and Pedersen, S.F. (2015). The glutamate transport inhibitor DL-Threo-beta-Benzyloxyaspartic acid (DL-TBOA) differentially affects SN38- and oxaliplatin-induced death of drug-resistant colorectal cancer cells. BMC Cancer *15*, 411. https://doi.org/10.1186/s12885-015-1405-8.

37. Szymczyk, J., Sluzalska, K.D., Materla, I., Opalinski, L., Otlewski, J., and Zakrzewska, M. (2021). FGF/FGFR-Dependent Molecular Mechanisms Underlying Anti-Cancer Drug Resistance. Cancers *13*, 5796. https://doi.org/10.3390/cancers13225796.

38. Chen, J., Wang, H., Peng, F., Qiao, H., Liu, L., Wang, L., and Shang, B. (2022). Ano1 is a Prognostic Biomarker That is Correlated with Immune Infiltration in Colorectal Cancer. Int. J. Gen. Med. *15*, 1547–1564. https://doi.org/10.2147/IJGM.S348296.

39. Schulz-Heddergott, R., Stark, N., Edmunds, S.J., Li, J., Conradi, L.C., Bohnenberger, H., Ceteci, F., Greten, F.R., Dobbelstein, M., and Moll, U.M. (2018). Therapeutic Ablation of Gain-of-Function Mutant p53 in Colorectal Cancer Inhibits Stat3-Mediated Tumor Growth and Invasion. Cancer Cell *34*, 298–314.e7.

40. Pich, O., Bailey, C., Watkins, T.B.K., Zaccaria, S., Jamal-Hanjani, M., and Swanton, C. (2022). The translational challenges of precision oncology. Cancer Cell *40*, 458–478.

41. Hanahan, D. (2022). Hallmarks of Cancer: New Dimensions. Cancer Discov. *12*, 31–46.

42. Shi, Z.-D., Pang, K., Wu, Z.-X., Dong, Y., Hao, L., Qin, J.-X., Wang, W., Chen, Z.-S., and Han, C.-H. (2023). Tumor cell plasticity in targeted therapy-induced resistance: mechanisms and new strategies. Signal Transduct. Targeted Ther. *8*, 113.

43. Zhang, B., Yao, K., Zhou, E., Zhang, L., and Cheng, C. (2021). Chr20q Amplification Defines a Distinct Molecular Subtype of Microsatellite Stable Colorectal Cancer. Cancer Res. *81*, 1977–1987.

44. Bao, L., Qian, Z., Lyng, M.B., Wang, L., Yu, Y., Wang, T., Zhang, X., Yang, H., Brünner, N., Wang, J., and Ditzel, H.J. (2018). Coexisting genomic aberrations associated with lymph node metastasis in breast cancer. J. Clin. Invest. *128*, 2310–2324.

45. Frey, P., Devisme, A., Rose, K., Schrempp, M., Freihen, V., Andrieux, G., Boerries, M., and Hecht, A. (2022). SMAD4 mutations do not preclude epithelial-mesenchymal transition in colorectal cancer. Oncogene *41*, 824–837.

46. Fleming, N.I., Jorissen, R.N., Mouradov, D., Christie, M., Sakthianandeswaren, A., Palmieri, M., Day, F., Li, S., Tsui, C., Lipton, L., et al. (2013). SMAD2, SMAD3 and SMAD4 mutations in colorectal cancer. Cancer Res. *73*, 725–735.

47. Mehrvarz Sarshekeh, A., Advani, S., Overman, M.J., Manyam, G., Kee, B.K., Fogelman, D.R., Dasari, A., Raghav, K., Vilar, E., Manuel, S., et al. (2017). Association of SMAD4 mutation with patient demographics, tumor characteristics, and clinical outcomes in colorectal cancer. PLoS One *12*, e0173345.

48. Szeglin, B.C., Wu, C., Marco, M.R., Park, H.S., Zhang, Z., Zhang, B., Garcia-Aguilar, J., Beauchamp, R.D., Chen, X.S., and Smith, J.J. (2022). A SMAD4-modulated gene profile predicts disease-free survival in stage II and III colorectal cancer. Cancer Rep. *5*, e1423.

49. Zhang, B., Zhang, B., Chen, X., Bae, S., Singh, K., Washington, M.K., and Datta, P.K. (2014). Loss of Smad4 in colorectal cancer induces resistance to 5-fluorouracil through activating Akt pathway. Br. J. Cancer *110*, 946–957.

50. Lin, Z., Zhang, L., Zhou, J., and Zheng, J. (2019). Silencing Smad4 attenuates sensitivity of colorectal cancer cells to cetuximab by promoting epithelial-mesenchymal transition. Mol. Med. Rep. *20*, 3735–3745.

51. Ozawa, H., Ranaweera, R.S., Izumchenko, E., Makarev, E., Zhavoronkov, A., Fertig, E.J., Howard, J.D., Markovic, A., Bedi, A., Ravi, R., et al. (2017). SMAD4 Loss Is Associated with Cetuximab Resistance and Induction of MAPK/JNK Activation in Head and Neck Cancer Cells. Clin. Cancer Res. *23*, 5162–5175.

52. Zhang, B., Leng, C., Wu, C., Zhang, Z., Dou, L., Luo, X., Zhang, B., and Chen, X. (2016). Smad4 sensitizes colorectal cancer to 5-fluorouracil through cell cycle arrest by inhibiting the PI3K/Akt/CDC2/survivin cascade. Oncol. Rep. *35*, 1807–1815.

53. Yu, H., Pardoll, D., and Jove, R. (2009). STATs in cancer inflammation and immunity: a leading role for STAT3. Nat. Rev. Cancer *9*, 798–809. https://doi.org/10.1038/nrc2734.

54. Feng, H., Liu, K., Shen, X., Liang, J., Wang, C., Qiu, W., Cheng, X., and Zhao, R. (2020). Targeting tumor cell-derived CCL2 as a strategy to overcome Bevacizumab resistance in ETV5+ colorectal cancer. Cell Death Dis. *11*, 916. https://doi.org/10.1038/s41419-020-03111-7.

55. Yu, D., Xu, H., Zhou, J., Fang, K., Zhao, Z., and Xu, K. (2024). PDPN/CCL2/STAT3 feedback loop alter CAF heterogeneity to promote angiogenesis in colorectal cancer. Angiogenesis *27*, 809–825. https://doi.org/10.1007/s10456-024-09941-9.

56. Chun, E., Lavoie, S., Michaud, M., Gallini, C.A., Kim, J., Soucy, G., Odze, R., Glickman, J.N., and Garrett, W.S. (2015). CCL2 Promotes Colorectal Carcinogenesis by Enhancing Polymorphonuclear Myeloid-Derived Suppressor Cell Population and Function. Cell Rep. *12*, 244–257. https://doi.org/10.1016/j.celrep.2015.06.024.

57. Shah, M.A., Shitara, K., Lordick, F., Bang, Y.J., Tebbutt, N.C., Metges, J.P., Muro, K., Lee, K.W., Shen, L., Tjulandin, S., et al. (2022). Randomized, double-blind, placebo-controlled phase III study of paclitaxel$\pm$Napabucasin in pretreated advanced gastric or gastroesophageal junction adenocarcinoma. Clin. Cancer Res. *28*, OF1–OF9.

58. Sonbol, M.B., Ahn, D.H., Goldstein, D., Okusaka, T., Tabernero, J., Macarulla, T., Reni, M., Li, C.P., O'Neil, B., Van Cutsem, E., and Bekaii-Saab, T. (2019). CanStem111P trial: a Phase III study of napabucasin plus nab-paclitaxel with gemcitabine. Future Oncol. *15*, 1295–1302.

59. Jonker, D.J., Nott, L., Yoshino, T., Gill, S., Shapiro, J., Ohtsu, A., Zalcberg, J., Vickers, M.M., Wei, A.C., Gao, Y., et al. (2018). Napabucasin versus placebo in refractory advanced colorectal cancer: a randomised phase 3 trial. Lancet. Gastroenterol. Hepatol. *3*, 263–270.

60. Fan, Z., Cui, Y., Chen, L., Liu, P., and Duan, W. (2024). 23-Hydroxybetulinic acid attenuates 5-fluorouracil resistance of colorectal cancer by modulating M2 macrophage polarization via STAT6 signaling. Cancer Immunol. Immunother. *73*, 83. https://doi.org/10.1007/s00262-024-03662-0.

61. Laoukili, J., Constantinides, A., Wassenaar, E.C.E., Elias, S.G., Raats, D.A.E., van Schelven, S.J., van Wettum, J., Volckmann, R., Koster, J., Huitema, A.D.R., et al. (2022). Peritoneal metastases from colorectal cancer belong to Consensus Molecular Subtype 4 and are sensitised to oxaliplatin by inhibiting reducing capacity. Br. J. Cancer *126*, 1824–1833. https://doi.org/10.1038/s41416-022-01742-5.

62. Mitsuhashi, A., Goto, H., Saijo, A., Trung, V.T., Aono, Y., Ogino, H., Kuramoto, T., Tabata, S., Uehara, H., Izumi, K., et al. (2015). Fibrocyte-like cells mediate acquired resistance to anti-angiogenic therapy with bevacizumab. Nat. Commun. *6*, 8792. https://doi.org/10.1038/ncomms9792.

63. Mooi, J.K., Wirapati, P., Asher, R., Lee, C.K., Savas, P., Price, T.J., Townsend, A., Hardingham, J., Buchanan, D., Williams, D., et al. (2018). The prognostic impact of consensus molecular subtypes (CMS) and its predictive effects for bevacizumab benefit in metastatic colorectal cancer: molecular analysis of the AGITG MAX clinical trial. Ann. Oncol. *29*, 2240–2246. https://doi.org/10.1093/annonc/mdy410.

64. Yang, X., Lin, Y., Shi, Y., Li, B., Liu, W., Yin, W., Dang, Y., Chu, Y., Fan, J., and He, R. (2016). FAP Promotes Immunosuppression by Cancer-Associated Fibroblasts in the Tumor Microenvironment via STAT3-CCL2 Signaling. Cancer Res. *76*, 4124–4135. https://doi.org/10.1158/0008-5472.CAN-15-2973.

65. Yu, H., Kortylewski, M., and Pardoll, D. (2007). Crosstalk between cancer and immune cells: role of STAT3 in the tumour microenvironment. Nat. Rev. Immunol. *7*, 41–51. https://doi.org/10.1038/nri1995.

66. Cerami, E., Gao, J., Dogrusoz, U., Gross, B.E., Sumer, S.O., Aksoy, B.A., Jacobsen, A., Byrne, C.J., Heuer, M.L., Larsson, E., et al. (2012). The cBio cancer genomics portal: an open platform for exploring multidimensional cancer genomics data. Cancer Discov. *2*, 401–404. https://doi.org/10.1158/2159-8290.Cd-12-0095.

67. Li, H., and Durbin, R. (2009). Fast and accurate short read alignment with Burrows-Wheeler transform. Bioinformatics *25*, 1754–1760. https://doi.org/10.1093/bioinformatics/btp324.

68. Chen, S., Zhou, Y., Chen, Y., and Gu, J. (2018). fastp: an ultra-fast all-in-one FASTQ preprocessor. Bioinformatics *34*, i884–i890. https://doi.org/10.1093/bioinformatics/bty560.

69. Hu, H., Mu, Q., Bao, Z., Chen, Y., Liu, Y., Chen, J., Wang, K., Wang, Z., Nam, Y., Jiang, B., et al. (2018). Mutational Landscape of Secondary Glioblastoma Guides MET-Targeted Trial in Brain Tumor. Cell *175*, 1665–1678.e18. https://doi.org/10.1016/j.cell.2018.09.038.

70. Li, H., Handsaker, B., Wysoker, A., Fennell, T., Ruan, J., Homer, N., Marth, G., Abecasis, G., and Durbin, R.; 1000 Genome Project Data Processing Subgroup (2009). The Sequence Alignment/Map format and SAMtools. Bioinformatics *25*, 2078–2079. https://doi.org/10.1093/bioinformatics/btp352.

71. Shen, R., and Seshan, V.E. (2016). FACETS: allele-specific copy number and clonal heterogeneity analysis tool for high-throughput DNA sequencing. Nucleic Acids Res. *44*, e131. https://doi.org/10.1093/nar/gkw520.

72. Kautto, E.A., Bonneville, R., Miya, J., Yu, L., Krook, M.A., Reeser, J.W., and Roychowdhury, S. (2017). Performance evaluation for rapid detection of pan-cancer microsatellite instability with MANTIS. Oncotarget *8*, 7452–7463. https://doi.org/10.18632/oncotarget.13918.

73. Paradis, E., Claude, J., and Strimmer, K. (2004). APE: Analyses of Phylogenetics and Evolution in R language. Bioinformatics *20*, 289–290. https://doi.org/10.1093/bioinformatics/btg412.

74. Dobin, A., Davis, C.A., Schlesinger, F., Drenkow, J., Zaleski, C., Jha, S., Batut, P., Chaisson, M., and Gingeras, T.R. (2013). STAR: ultrafast universal RNA-seq aligner. Bioinformatics *29*, 15–21. https://doi.org/10.1093/bioinformatics/bts635.

75. Liao, Y., Smyth, G.K., and Shi, W. (2014). featureCounts: an efficient general purpose program for assigning sequence reads to genomic features. Bioinformatics *30*, 923–930. https://doi.org/10.1093/bioinformatics/btt656.

76. Zhang, Y., Parmigiani, G., and Johnson, W.E. (2020). ComBat-seq: batch effect adjustment for RNA-seq count data. NAR Genom. Bioinform. *2*, lqaa078. https://doi.org/10.1093/nargab/lqaa078.

77. Yoshihara, K., Shahmoradgoli, M., Martínez, E., Vegesna, R., Kim, H., Torres-Garcia, W., Treviño, V., Shen, H., Laird, P.W., Levine, D.A., et al. (2013). Inferring tumour purity and stromal and immune cell admixture from expression data. Nat. Commun. *4*, 2612. https://doi.org/10.1038/ncomms3612.

78. Love, M.I., Huber, W., and Anders, S. (2014). Moderated estimation of fold change and dispersion for RNA-seq data with DESeq2. Genome Biol. *15*, 550. https://doi.org/10.1186/s13059-014-0550-8.

79. Ritchie, M.E., Phipson, B., Wu, D., Hu, Y., Law, C.W., Shi, W., and Smyth, G.K. (2015). limma powers differential expression analyses for RNA-sequencing and microarray studies. Nucleic Acids Res. *43*, e47. https://doi.org/10.1093/nar/gkv007.

80. Subramanian, A., Tamayo, P., Mootha, V.K., Mukherjee, S., Ebert, B.L., Gillette, M.A., Paulovich, A., Pomeroy, S.L., Golub, T.R., Lander, E.S., and Mesirov, J.P. (2005). Gene set enrichment analysis: a knowledge-based approach for interpreting genome-wide expression profiles. Proc. Natl. Acad. Sci. USA *102*, 15545–15550. https://doi.org/10.1073/pnas.0506580102.

81. Chen, E.Y., Tan, C.M., Kou, Y., Duan, Q., Wang, Z., Meirelles, G.V., Clark, N.R., and Ma'ayan, A. (2013). Enrichr: interactive and collaborative HTML5 gene list enrichment analysis tool. BMC Bioinf. *14*, 128. https://doi.org/10.1186/1471-2105-14-128.

82. Cable, D.M., Murray, E., Zou, L.S., Goeva, A., Macosko, E.Z., Chen, F., and Irizarry, R.A. (2022). Robust decomposition of cell type mixtures in spatial transcriptomics. Nat. Biotechnol. *40*, 517–526. https://doi.org/10.1038/s41587-021-00830-w.

83. Hess, L.M., Brnabic, A., Mason, O., Lee, P., and Barker, S. (2019). Relationship between Progression-free Survival and Overall Survival in Randomized Clinical Trials of Targeted and Biologic Agents in Oncology. J. Cancer *10*, 3717–3727. https://doi.org/10.7150/jca.32205.

84. Tarasov, A., Vilella, A.J., Cuppen, E., Nijman, I.J., and Prins, P. (2015). Sambamba: fast processing of NGS alignment formats. Bioinformatics *31*, 2032–2034. https://doi.org/10.1093/bioinformatics/btv098.

85. Cancer Genome Atlas Network (2012). Comprehensive molecular characterization of human colon and rectal cancer. Nature *487*, 330–337. https://doi.org/10.1038/nature11252.

86. Saitou, N., and Nei, M. (1987). The neighbor-joining method: a new method for reconstructing phylogenetic trees. Mol. Biol. Evol. *4*, 406–425. https://doi.org/10.1093/oxfordjournals.molbev.a040454.

87. Liberzon, A., Birger, C., Thorvaldsdóttir, H., Ghandi, M., Mesirov, J.P., and Tamayo, P. (2015). The Molecular Signatures Database (MSigDB) hallmark gene set collection. Cell Syst. *1*, 417–425. https://doi.org/10.1016/j.cels.2015.12.004.

88. Varn, F.S., Johnson, K.C., Martinek, J., Huse, J.T., Nasrallah, M.P., Wesseling, P., Cooper, L.A.D., Malta, T.M., Wade, T.E., Sabedot, T.S., et al. (2022). Glioma progression is shaped by genetic evolution and microenvironment interactions. Cell *185*, 2184–2199.e16. https://doi.org/10.1016/j.cell.2022.04.038.

89. Huang, N., Liu, Y., Fang, Y., Zheng, S., Wu, J., Wang, M., Zhong, W., Shi, M., Xing, M., and Liao, W. (2020). Gold Nanoparticles Induce Tumor Vessel Normalization and Impair Metastasis by Inhibiting Endothelial Smad2/3 Signaling. ACS Nano *14*, 7940–7958. https://doi.org/10.1021/acsnano.9b08460.

90. Wang, J., Huang, Q., Hu, X., Zhang, S., Jiang, Y., Yao, G., Hu, K., Xu, X., Liang, B., Wu, Q., et al. (2022). Disrupting Circadian Rhythm via the PER1-HK2 Axis Reverses Trastuzumab Resistance in Gastric Cancer. Cancer Res. *82*, 1503–1517. https://doi.org/10.1158/0008-5472.Can-21-1820.

STAR★METHODS

KEY RESOURCES TABLE

REAGENT or RESOURCE	SOURCE	IDENTIFIER
Antibodies		
Rabbit anti-SMAD4	CST	Cat# 46535; RRID: AB_2736998
Rabbit anti-DYKDDDDK	CST	Cat# 14793; RRID: AB_2572291
Rabbit anti-STAT3	CST	Cat# 12640; RRID: AB_2629499
Rabbit anti-phospho-STAT3 (Tyr705)	CST	Cat# 9145; RRID: AB_2491009
Rabbit anti-SHP2	CST	Cat# 3397; RRID: AB_2174959
Mouse monoclonal anti-SMAD4R361H	NewEast Biotechnologies	Cat# 26422; RRID: AB_2629384
Mouse monoclonal anti-β-Actin	Proteintech	Cat# 60008-1-Ig; RRID: AB_2289225
Mouse monoclonal anti-GAPDH	Proteintech	Cat# 60004–1-Ig; RRID: AB_2107436
Mouse monoclonal anti-CCL2	Proteintech	Cat# 66272-1-Ig; RRID: AB_2861337
Rabbit anti-Ki-67	Proteintech	Cat# 27309-1-AP; RRID: AB_2756525
Rabbit anti-CD31	Proteintech	Cat# 11265-1-AP; RRID: AB_2299349
Alexa Fluor 647-labeled Goat Anti-Rabbit IgG	Beyotime	Cat# A0468; RRID: AB_2936379
Chemicals, peptides, and recombinant proteins		
STATTIC	MCE (MedChemExpress)	Cat# HY-13818
JSH-23	MCE (MedChemExpress)	Cat# HY-13982
AC-4-130	MCE (MedChemExpress)	Cat# HY-124500
GB201	MCE (MedChemExpress)	Cat# HY-13919
Recombinant CCL2 protein	MCE (MedChemExpress)	Cat# HY-P7237
5-FU	Hainan Zhuotai Pharmaceutical Co., Ltd	N/A
Oxaliplatin	Jiangsu Hengrui Pharmaceuticals Co., Ltd	N/A
Irinotecan	Selleck	Cat# S5026
Bevacizumab	Roche Pharma (Schweiz) Ltd	N/A
B20.4–1.1	Genentech	N/A
Deposited data		
Raw DNA sequencing data	Bao et al.[44]	PRJNA635121
MSK mutation data	Yaeger et al.[10]	PRJEB2384
ChangKang mutation data	Zhao et al.[12]	HRA000873
TCGA mutation data	Cerami et al.[66]	https://www.cbioportal.org/study/summary?id=coadread_tcga
CRLM single cell data	Sathe et al.[27]	https://dna-discovery.stanford.edu/research/datasets
CRLM spatial transcriptomic data	Wu et al.[29]	OEP001756
CRLM RNAseq raw data	This paper	HRA005455
CRLM WES raw data	This paper	HRA005455
Software and algorithms		
bwa	Li et al.[67]	http://maq.sourceforge.net/
fastp	Chen et al.[68]	https://github.com/OpenGene/fastp
SAVI2	Hu et al.[69]	https://github.com/WangLabHKUST/SAVI
samtools	Li et al.[70]	http://samtools.sourceforge.net/
Facets	Shen et al.[71]	https://github.com/mskcc/facets

(*Continued on next page*)

Continued

REAGENT or RESOURCE	SOURCE	IDENTIFIER
MANTIS	Kautto et al.[72]	https://github.com/OSU-SRLab/MANTIS
ape	Paradis et al.[73]	https://cran.r-project.org/web/packages/ape/index.html
Cello2-R	Jiang et al.[24]	https://github.com/WangLabHKUST/CELLO
STAR	Dobin et al.[74]	https://github.com/alexdobin/STAR
featureCounts	Liao et al.[75]	http://subread.sourceforge.net/
Comb-seq	Zhang et al.[76]	https://github.com/zhangyuqing/ComBat-seq
ESTIMATE	Yoshihara et al.[77]	http://www.bioconductor.org/
DESeq2	Love et al.[78]	http://www.bioconductor.org/
limma	Ritchie et al.[79]	http://www.bioconductor.org/
GSEA	Subramanian et al.[80]	https://www.gsea-msigdb.org/gsea/index.jsp
Enrichr	Chen et al.[81]	https://maayanlab.cloud/Enrichr/
CMSclassifier	Guinney et al.[11]	https://github.com/Sage-Bionetworks/CMSclassifier
BayesPrism	Chu et al.[26]	https://github.com/Danko-Lab/BayesPrism
spacexr	Cable et al.[82]	https://github.com/dmcable/spacexr
Python (3.8.5)	Anaconda	https://www.anaconda.com/
R (4.2.2)	CRAN	https://cran.r-project.org/
Python code	This paper	https://github.com/WangLabHKUST/CRLM https://doi.org/10.5281/zenodo.13997442

EXPERIMENTAL MODEL AND STUDY PARTICIPANT DETAILS

Clinical sample acquisition and treatment response evaluation

Patients' samples were collected and analyzed after informed consent was obtained and approved by the ethics committee (NFEC-2017-206) of Nanfang Hospital, Southern Medical University (Guangzhou, China). The enrolled patients with clinically and histologically confirmed colorectal cancer liver metastases (CRLM) were defined by the American Joint Committee on Cancer guidelines. Forty-nine patients with unresectable CRLM were recruited. Thirty-six patients were treated with mFOLFOX6 (modified fluorouracil, leucovorin, and oxaliplatin) plus bevacizumab, and the other thirteen were treated with FOLFIRI (fluorouracil, leucovorin, and irinotecan) plus bevacizumab (Table S1). A liver biopsy was performed in all patients before initial treatment, and the same site was biopsied within one week after response evaluation and blood samples as ref.[14]. Two patients received a fourth biopsy, and 13 patients received a third biopsy as the tumor progressed. Therapeutic responses were defined by Response Evaluation Criteria in Solid Tumors (RECIST 1.1) and assessed radiographically about every four treatment cycles. The RECIST of the biopsy and RECIST of all evaluated lesions were used to determine of responders and non-responders (Figure S1C). Progression-free survival (PFS),[83] the period from the start of treatment until the first of disease progressed, and overall survival (OS),[83] the period of patient survival after the start of treatment. The biopsy specimens were paraffin-embedded and stored in RNAlater (Qiagen, Düsseldorf, Germany), respectively. Suppose tumor content was estimated to be over 40% after a thorough pathological review; tumor RNA and DNA were extracted from freshly obtained tissues. Next, the whole-exome sequencing (WES, n = 44), panel sequencing data (n = 5), and RNA sequencing of the tumor biopsy specimens were parallelly performed. As for blood samples, plasma, and blood cells were sub-packaged into 500 pL per vial and stored at 80°C until use.

Cell lines

Human colorectal cancer cell lines SW480 and HCT116 were obtained from were purchased from Guangzhou Jennio Biological Science and Technology Ltd (Guangzhou, China), and murine colon cancer cell line CT26 was obtained from the Center for Typical Culture Collection, Chinese Academy of Sciences (Shanghai, China). All cells were cultured with RPMI 1640 medium (Solarbio, 31800) with 10% fetal bovine serum (Hyclone, USA) in a 5% CO2 incubator at 37°C. For site mutation of SMAD4, cells were stably transfected with pHBLV-CMV-MCS-3FLAG-EF1-Luc-T2A-Puro constructs (Hanbio, China) and subsequently selected with puromycin medium (Invitrogen) according to the manufacturer's instructions, with western blotting used to verify the efficiency of the sequence.

Animals

All animal experiments were conducted by the Public Health Service Policy in Humane Care and Use of Laboratory Animals and were approved by the Ethical Committee of Southern Medical University. *BALB/c* male mice aged 4–5 weeks were purchased from the Experimental Animal Center, Southern Medical University (Guangzhou, China). To assess the effectiveness of 5-FU and bevacizumab on colon cancer with different states of the SMAD4 gene, 1×10^7 transfected CT26 cells were subcutaneously injected into the left flank of mice. One week after cell inoculation, mice were treated with PBS, 5-FU (25 mg/kg, i.p., twice a week), or 5-FU

combined with monoclonal BVZ (B20.4–1.1, 5 mg/kg, i.p., twice a week) for two weeks. Tumor volumes and mice weight were measured every two days. Tumor volume was calculated using the formula $V = 0.5 \times L \times W$,[2] where V is the volume, L is the length, and W is the width. After two weeks, the mice were euthanized to compare tumor weight and volume, and tumors were collected for immunohistochemistry and immunofluorescence staining. In addition, to verify the effect of GB201 on reversing 5-FU and bevacizumab resistance, 1×10^7 transfected CT26 cells with $SMAD4^{R361H}$ or $SMAD4^{R361C}$ mutation were respectively injected into mice subcutaneously. Mice were randomly divided into four groups. Each group was administered one of the following: PBS, 5-FU (25 mg/kg, i.p., twice a week) combined with monoclonal BVZ (5 mg/kg, i.p., twice a week), GB201 (10 mg/kg, i.p., q2d), and three-drug combination. Tumor volumes and mice weights were measured and recorded, and the mice were euthanized after two weeks.

METHOD DETAILS

DNA extraction and library construction

Genomic DNA was extracted from blood and tissue samples using the TIANamp Blood DNA Kits and TIANamp Genomic DNA Kits (Tiangen Biotech, Beijing, China), respectively, following the manufacturer's protocols. The extracted DNA was then fragmented using the ultra-sonicator UCD-200 (Diagenode, Seraing, Belgium). Subsequently, the fragmented DNA was purified and size-selected using magnetic beads (Beckman, MA, USA). The quality of the DNA was assessed using the Qubit 2.0 Fluorometer with the Quanti-IT dsDNA HS Assay Kit (Thermo Fisher Scientific, MA, USA). For library construction, the fragmented DNA was hybridized to the SeqCap EZ Exome 64M (Roche NimbleGen, Madison, WI, USA), following the manufacturer's instructions. The sequencing process was performed using the Gene+ Seq-2000 platform with 2 × 100-bp paired-end reads. To ensure data integrity, an in-house script was utilized to remove terminal adaptor sequences and low-quality reads from the raw data.

Somatic mutation detection

Raw fastq files were aligned to hg19 reference using bwa mem with default parameters after fastp quality checking.[67,68] Picard MarkDuplicates was applied to mark PCR duplicates. Aligned bam files of longitudinal (pre- and post-samples) tumors and matched normal blood were subjected to SAVI2 for somatic SNV/Indel calling which takes advantage of samtools for variant identification as before.[69] We set the parameter as '–conf 1e−5 –precision 5' to acquire more accurate mutational allele frequency (MAF). To remove false positives, we added three features to SAVI2 PD-filter report, including PON (all SNPs from blood samples were used to build a Panel of Normal variant set), AltNormal (altered reads in corresponding blood control bam files), and MQ0 (average number of reads with mapping quality of zero measured by sambamba[84]). The somatic mutation candidates were acquired based on the jointly filtering criteria: (1) MAF in blood $\leq$1%, altered depth in blood $\leq$2, altered depth in tumors >2; (2) not present in Meganormal database; (3) PON $\leq$2, MQ0 $\leq$ 5; AltNormal $\leq$2 for WES, AltNormal $\leq$15 for Panel; (4) not reported as common SNPs; (5) non-synonymous mutations. We then sought to identify mutated genes that (1) were reported in the Cancer Genome Atlas Network (TCGA, 2012)[85] analysis of CRC. The background mutation rate of each gene was calculated from 223 TCGA tumors (downloaded from cBioPortal).[66] Droplet Digital PCR (ddPCR) was used to detect the $SMAD4^{R361\ H/C}$ mutations in CRC tumor samples from the independent cohort. The cases supported by > 5 positive droplets and >0.5% fractional abundance were categorized as mutant; otherwise, they were classified as wild-type.

Somatic copy number alteration

Facets was applied to estimate somatic copy number alterations and tumor purity using WES/Panel sequencing data of tumor and matched blood.[71] The detailed parameter for embedded samtools mpileup was '-q15 -Q20' when other parameters were set as default. By taking the tumor purity (p) into account, the arm-level and cytoband-level copy number status was determined: a) copy number gain: the segment log2 ratio $\geq$ log2((2 + p)/2); b) copy number loss: the segment log2 ratio $\leq$ log2((2-p)/2). Copy number heterogeneity (CNH), defined as the average proportion of malignant cells that differ by one copy from the mode copy number value at each position of the genome was predicted using CNH MATLAB code[25] for each sample.

Microsatellite instability prediction

To estimate microsatellite instability status for each tumor sample, we applied MANTIS v1.0.4[72] with tumor-normal BAM files as input. RepeatFinder function with default parameters was firstly used to capture microsatellite loci within hg19 reference genome. Next, we run python program "mantis.py" with the following parameters: -mrq = 20.0, -mlq = 25.0, -mlc = 20, -mrr = 1. Samples with StepWise Difference (DIF) score between the tumor and normal distributions $\geq$0.4 were assigned "MSI-H" as recommended by the algorithm, and hence all samples were predicted as MSS.

Evolutionary tree

Somatic SNV/Indel of Pre, Post1, Post2 and Post3 samples from WES data were transformed as a binary matrix as representation of somatic mutation status, with 0 for wildtype and 1 for mutant. Then the matrix of each patient was subjected to calculate sample distance using *adist* function in R. Further, neighbor-joining tree estimation was completed using *nj* function from *ape* package.[73,86] Finally, the evolutionary tree of longitudinal timepoints was visualized in an unrooted manner. For each tree, the length of tree is proportional to the somatic mutation number. Cello2-R was used to obtain three-dimensional frequency of key driver altered genes and

moduli space analysis were performed to represent the evolutionary patterns following therapy using Cello2-MATLAB.[24] In the ternary plot, three variables, which sum up to a constant, are depicted on a two-dimensional graph using a barycentric plot. Specifically, the plot illustrates the fractions of mutations that are shared between pre-treatment and post-treatment, mutations that are private to the pre-treatment stage, and mutations that are private to the post-treatment stage, all of which have been adjusted using the ETRIP program and were represented in a matrix of three columns. The fractions matrix was subjected to K-means clustering with clusters parameter set to three and visualized using Cello2 in MATLAB, which could also be done using ggtern function in ggtern R package.

ETRIP (Evolutionary Tree Inference Program) is used to enhance the accuracy of phylogenetic tree inference by effectively estimating the underestimated mutations in tumor samples caused by factors such as low-purity or low-sequencing depth in DNA sequencing data. The real mutation allele spectrum (real MAS) is defined as the distribution of mutational allele frequency (MAF). The measured mutation allele spectrum (measured MAS) is defined as the distribution of calculated MAF, which is obtained by dividing the number of positive reads by the total reads. ETRIP first partitioned MAS into n intervals, namely $\{a_n\}$, where a_i means the number of alleles with MAF in $(\frac{1-1}{n}, \frac{i}{n}]$. In real MAS, denoted as $\{a_n\}$, with i ranging from 1 to n, while in measured MAS, denoted as $\{a'_n\}$, with i ranging from 0 to n where a_0 means the number of undetected alleles, i.e., false negatives. The purity of real MAS is 1, while the measured MAS has a purity of p, determined by the sample purity. ETRIP mimicked the process by a function that mapped the real MAS to the expected measured MAS ($\{a'_n\}_{exp}$) based on predetermined purity and read depth parameters. Subsequently, it generated an inferred real MAS whose measured MAS fits the observed measured MAS. To evaluate the accuracy of fitness, a chi-square score is computed. Ultimately, ETRIP calculates the false-negative rates for both pretreatment and post-treatment samples and regenerates the evolutionary trees.

The generation of the function $f(\{a_n\}) = \{a'_n\}_{exp}$ is based on two assumptions.

1. For an allele, the number of reads X (including positive reads and negatives) follows Poisson distribution $P(X = k) = \frac{\lambda^k}{k!}e^{-\lambda}$, where λ is read depth and k is a positive integer.
2. For an allele with k reads, the number of positive reads Y follows binomial distribution $P(Y = m) = \binom{k}{m}(p \cdot MAF)^m(1 - p \cdot MAF)^{k-m}$, where MAF is the allele frequency when purity is 1, m is an integer between 0 and k. Particularly, for an allele in the i-th interval in MAS, its MAF can be approximated to $\frac{i-0.5}{n}$ when n is large. Then $P_i(Y = m) = \binom{k}{m}(p \cdot \frac{i-0.5}{n})^m(1 - p \cdot \frac{i-0.5}{n})^{k-m}$.

Therefore, the contribution c from the alleles in the i-th interval in real MAS to the j-th interval in measured MAS is

$$c(i,j) = \sum_{k=0}^{\infty}\left[P(X = k)\sum_{m \in \left(\frac{i-1}{n}k, \frac{i}{n}k\right]} P_i(Y = m)\right]$$

Hence, the expected value of a'_j is derived as

$$a'_j = \sum_{i=1}^{n} a_i c(i,j)$$

And the function $f(\{a_n\}) = \{a'_n\}_{exp}$ is generated.

Chi-square scoring system is used to evaluate the fitness between expected measured MAS $\{a'_n\}_{exp}$ and observed measured MAS $\{a'_n\}_{obs}$ which is obtained from DNA-seq data. It calculates $\sum_{i=1}^{n}\frac{([a'_i]_{exp} - [a'_i]_{obs})^2}{[a'_i]_{exp}}$ with the degree of freedom n. The higher score indicates less confidence or less fitness. ETRIP infers the real MAS with purity = 1 from the observed MAS with purity = p by performing the following steps.

1. generate a rough candidate real MAS n$\{a_n\}_{ca}$.
2. calculate $\{a'_n\}_{exp} = f(\{a_n\}_{can})$, which is the expected measured MAS.
3. calculate Chi-square score between $\{a'_n\}_{exp}$ and s$\{a'_n\}_{ob}$.
4. iterate each element in $\{a_n\}_{can}$, modify its value, perform step 2 and 3 again, compare the scores before and after modification, keep the version of $\{a_n\}_{can}$ with lower score.
5. repeat step 4 until no modification is applied.
6. output $\{a_n\}_{can}$ as inferred real MAS.

With the inferred real MAS, ETRIP calculates $\{a'_n\} = f(\{a_n\}_{can})$ and hence false negative rate fn $= \frac{a'_0}{\sum_{i=0}^{n} a'_i}$ of Pre (fn_{Pre}) and Post (fn_{Post}) respectively. Then ETRIP infers the evolutionary tree by solving the following maximum likelihood equations.

$$\text{Measured Pre-private} = \text{Inferred real Pre-private} \times (1 - fn_{Pre})$$

$$\text{Measured Post-private} = \text{Inferred real Post-private} \times (1 - fn_{Post})$$

$$\text{Measured shared} = \text{Inferred real shared} \times (1 - fn_{Pre}) \times (1 - fn_{Post})$$

The process of inferring the evolutionary tree is completed after resolving three false negative rates.

RNA extraction and library construction

For RNA extraction from tissue samples, the Trizol reagent was employed. Subsequently, strict quality control measures were implemented for the RNA samples, which encompassed three main aspects. Firstly, concentration and total quantity were assessed using Qubit 4.0. Secondly, the integrity of the RNA samples was evaluated using the Agilent 2100 Bioanalyzer (Agilent Technologies, CA, USA). Lastly, sample purity was evaluated using the NanoDrop spectrophotometer. Following quality assessment, RNA sequencing libraries were constructed using the TruSeq RNA Sample Prep Kits, v2 (Illumina, CA, USA). Once the library construction was completed, an initial quantification was carried out, and the library was subsequently diluted. The distribution of library fragments was determined using the Agilent 2100 DNA 1000 Kit. Finally, the library was sequenced using a Gene+ Seq-2000 sequencer. Similar to the earlier DNA sequencing process, an in-house script was utilized to remove terminal adaptor sequences and low-quality reads from the raw data.

Bulk RNA-seq preprocessing

Data quality control was performed with fastp.[68] Reads were aligned to the human reference genome (GRCh38) using STAR v2.7.0days.[74] Gene count tables were generated by featureCounts[75] and normalized as Fragments Per Kilobase Million (FPKM). Comb-seq[76] was used for batch correction. The ESTIMATE algorithm[77] was used to infer tumor purity from bulk tissue samples.

Differential gene expression analysis, pathway analysis and gene set enrichment

For the analysis of differentially expressed genes, we restricted our analysis on protein-coding transcripts. DESeq2 v.1.32.0[78] (two-sided Wald-test and Benjamini-Hochberg FDR correction) or limma v3.48.3 was used to identify genes differentially expressed between two groups. Comparison of pathway activity between pre-treatment and posttreatment samples was performed by Gene Set Enrichment Analysis (GSEA)[80] of 50 MSigDB hallmark gene sets.[87] The enriched gene sets with normalized enrichment score >1.2 or < −1.2 were selected in Figure 2H. The AR and IR gene list was analyzed using Enrichr[81] to identify significantly enriched pathways ($p < 0.05$), and the pathway rankings were determined based on the p values (Figures 3B and 4B). The AR gene signature score (Figure S6E) was computed by taking the weighted average expression (log2FPKM) of 80 resistant genes and subtracting the weighted average expression of 20 sensitive genes for each sample. The weights assigned to each gene were based on their AR contribution.

Sample-based response feature selection

To identify molecular determinants related to BVZ-based chemotherapy response, we developed Sample-based Response Feature Selection (SRFS). In the initial phase, SRFS pooled all available samples together to increase our statistical power for detecting changes and then we excluded the post-therapy samples with PR to eliminate ambiguous response annotations. Following this, the remaining samples were re-annotated based on their subsequent timepoint responses to roughly reflect how tumors would react to the upcoming treatment. In the second phase, SRFS categorized the samples into two groups - sensitive (PR, $n = 27$) or resistant group (SD or PD, $n = 64$) - based on their updated response. For genomic features, SRFS gauged their discriminative potential between the two groups using a two-sided Fisher's exact test, while transcriptomic features were assessed in a univariate logistic regression model. Significant features were categorized as either resistance-related or sensitivity-related. In the third phase, for resistance-related features, SRFS assessed their contribution to IR by calculating the proportion of patients consistently displaying genomic alterations or higher gene expression (using average expression as a threshold) throughout the treatment period, among all IR patients. Conversely, for sensitivity-related features, IR contribution counted the patients consistently lacking genomic alterations or showing lower gene expression throughout treatment. In the context of AR contribution, resistance-related genomic features measured the proportion of patients developing genomic alterations post-treatment among all AR patients, while sensitivity-related features focused on lost alterations. For transcriptomic features, resistance-related ones considered patients with an increased gene expression trend (from low to high) post-treatment, while sensitivity-related features assessed the declining trend. To decouple AR-from IR-related features, we defined the AR features as AR contributions exceeding the average (43.6%) of all significant genes, while IR features were defined as contributions surpassing the average (47.3%) of IR contributions. Features such as

somatic mutations, copy number alterations, tumor purity and ploidy, CNH, mutation burden, and CMS subtypes were classified as AR and IR features if their contributions exceeded 30%. Cell type proportions were categorized using a cutoff of 20%.

Bulk transcriptional subtype classification

Consensus Molecular Subtypes (CMS)[11] were applied using classifyCMS.SSP function within CMSclassifier v1.0.0. All CMS subtypes with minCor>=0.15 and minDelta>=0.06 were assigned to the sample in SSP.predictedCMS output while the "mixed" CMS subtypes were defined by 'NA' (unclassified) results with minCor<0.15 or minDelta<0.06.

Deconvolution analysis

The BayesPrism v1.4[26] was used to infer the relative cellular proportions and cell type-specific gene expression matrices. Reference scRNA-seq count matrix was extracted from a previous paper,[27] which identified eight cell types including tumor epithelial cells, normal hepatocytes, endothelial cells, fibroblasts, myeloid cells, T cells, NK cells and B cells. To verify the validity of deconvolution results in our CRLM RNA data, we applied the method to the synthetic mixtures created according to the previously described procedure.[88] Correlation analysis was conducted to compare the inferred proportions from BayesPrism with the true proportions.

Spatial transcriptomic data analysis

The spatial transcriptomic data (ST-P1 and ST-P3) from CRLM samples pre- and post-XELOX treatment was downloaded from a prior paper.[29] RCTD (spacexr v2.0.3)[82] was implemented to estimate relative cell type abundance for each spot. The scRNA-seq dataset[27] was used for reference input. Cell types were considered to exist in spots only if their cell proportions exceeded a certain threshold. We used the cell type labels from the prior paper as the ground truth. For cell types reported in prior paper (Epithelial, Hepatocyte, Fibroblast, and Endothelial), we selected thresholds that yielded the maximum F-scores between the predicted labels and real labels. For other cell types (Myeloid, T, B, NK), we set the threshold as 0.1. Next, we examined if certain cell types had spatial interactions or exclusions within a single spot. This involved calculating the ratio for the presence of each cell type amongst all spots. The statistical significance of spatial interactions or exclusions for specific cell type combinations was determined by one proportion z-test with their presence probabilities as the null hypothesis.

Machine learning model

A machine-learning model was built to classify BVZ-C treatment response in patients based on genomic and transcriptomic markers. Using 22 key features—including SMAD4 mutation status, 20q-gain, and expression of the top 10 resistance- and sensitivity-associated genes—a Random Forest classifier was trained on data from the main cohort (n = 48). Missing data was handled with BayesianRidge iterative imputation, and the model involved 10 decision trees with a depth limit of 5, optimized through 5-fold cross-validation for best performance.

Antibodies

Rabbit anti-SMAD4 (Cat# 46535, RRID: AB_2736998), rabbit anti-DYKDDDDK (Cat# 14793, RRID: AB_2572291), rabbit anti-STAT3 (Cat# 12640, RRID: AB_2629499), rabbit anti-phospho-STAT3 (Tyr705) (Cat# 9145, RRID: AB_2491009), rabbit anti-SHP2 (Cat# 3397, RRID: AB_2174959) were obtained from Cell Signaling Technology (CST). Mouse monoclonal anti-SMAD4^{R361H} (Cat# 26422, RRID: AB_2629384) were obtained from NewEast Biotechnologies. Mouse monoclonal anti-β-Actin (Cat# 60008-1-Ig, RRID: AB_2289225), mouse monoclonal anti-GAPDH (Cat# 60004–1-Ig, RRID: AB_2107436), mouse monoclonal anti-CCL2 (Cat# 66272-1-Ig, RRID:AB_2861337), rabbit anti-Ki-67 (Cat# 27309-1-AP, RRID: AB_2756525) and rabbit anti-CD31 (Cat# 11265-1-AP, RRID: AB_2299349) were obtained from Proteintech. Alexa Fluor 647-labeled Goat Anti-Rabbit IgG (Cat# A0468, RRID: AB_2936379) and 2-(4-Amidinophenyl)-6-indolecarbamidine dihydrochloride (DAPI) (Cat# C1002) were obtained from Beyotime.

Chemicals

5-FU and oxaliplatin were respectively obtained from Hainan Zhuotai Pharmaceutical Co., Ltd and Jiangsu Hengrui Pharmaceuticals Co., Ltd. Irinotecan (Cat# S5026) was obtained from Selleck. Human bevacizumab and murine monoclonal bevacizumab (B20.4–1.1) were respectively obtained from Roche Pharma (Schweiz) Ltd and Genentech. The STATTIC (Cat# HY-13818), JSH-23 (Cat# HY-13982), AC-4-130 (Cat# HY-124500), GB201(Cat# HY-13919), and recombinant CCL2 protein (Cat# HY-P7237) were obtained from MCE (MedChemExpress).

Scoring of morphological response to therapy

The contrast-enhanced CT scans of CRLM patients at the efficacy evaluation time node (Reponse, n = 6; Primary Resistance, n = 9; Acquired Resistance, n = 7) were available for the analysis of morphological response to therapy using a method based on previously published morphological response criteria.[31] Morphological response to replacement histopathological growth pattern (RHGP) was calculated based on whether the lesion changed from a homogeneous, low-attenuation lesion with a thin, sharply defined tumor-liver interface or a moderate degree of heterogeneous attenuation and a moderately defined tumor-liver interface to a heterogeneous attenuation and a thick, poorly defined tumor-liver interface after treatment. Morphological response was scored independently by 3 observers using the same criteria.

Tumor conditioned medium

For preparation of tumor conditioned medium (TCM), stable transfected SW480 and HCT116 cells were inoculated into growth medium at a density of 1×10^6 cells overnight. After adherence and removing the growth medium, fresh medium (5mL) was added to further culture the cells for 48 h, and the supernatant was collected as tumor conditioned medium with cell debris and excess substances in the supernatant removed by centrifugation. Human vascular endothelial cells (HUVECs) were stimulated with the collected TCM and standard medium in a 1:1 ratio for the subsequent experiments.

Cell tubule formation

Tubule formation assay for HUVECs was performed as previously described.[89] HUVECs were cultured with standard medium and TCM with or without bevacizumab (0.25 mg/ml) for 48h, and subsequently suspended in corresponding medium and incubated in matrigel (ABW, Cat# 082704) in μ-slide angiogenesis 12-well plate for 4h at 37°C before imaging. The capillary tubes were photographed and quantified by measuring the number of nudes. Three independent experiments were required for each treatment.

Cell viability assay

Cells were plated in 96-well plates and exposed to different concentrations of chemotherapeutic agents such as 5-FU and inhibitors of signaling pathways such as STATTIC for 48 h. Cell counting kit-8 (CCK-8) diluted with RPMI 1640 medium was added to the cells that were incubated for 2–3 h. Absorbance was measured at 450 nm using the SpectraMax M5 microplate reader.

Western blotting

Western blotting was performed as previously described.[90] The cells were washed with cold PBS buffer and prepared using lysis buffer (1mM PMSF, phosphatase inhibitor cocktail, and protease inhibitor cocktail). Protein concentrations of lysates were estimated using a BCA kit (Fdbio science). Separated proteins were resolved in SDS gels and transferred onto polyvinylidene difluoride membranes. Membranes were blocked in 5% BSA for 1 h. Primary antibodies used were anti-SMAD4 (1:1000; CST), anti-$SMAD4^{R361H}$ (1:1000; NewEast Biotechnologies), anti-FLAG (1:1000; CST), anti-STAT3 (1:1000; CST), anti-phospho-STAT3 (Tyr705) (1:1000; CST), anti-CCL2 (1:1000; Proteintech) and anti-β-Actin (1:5000; Proteintech). After incubation with goat anti-mouse or anti-rabbit IgG (Proteintech), the specific immunoreactive bands were detected with enhanced chemiluminescence (ECL kit, Fdbio science) using fluorescence luminescence and quantified by image software.

RNA isolation and quantitative PCR analysis

Total RNA was extracted from the cells using the TRIzol kit (R401-01, Vazyme) according to the manufacturer's instructions. Reverse transcription was performed using the First Strand cDNA Synthesis kit (R312-01, Vazyme). Quantitative PCR (qPCR) was performed using the LightCycler 480 system (Roche), as described in a previous study.[90] The expression levels of the target genes were normalized by subtracting the corresponding *GAPDH* threshold cycle (Ct) value. Primers used were: human CCL2: AGGTGACT GGGGCATTGAT and GCCTCCAGCATGAAAGTCTC.

Colony formation

Transfected tumor cells were seeded into 12-well plates (200 cells per well) and cultured for about two weeks. The medium with 5-FU treatment was replaced every three days. The colonies were washed using PBS, fixed with 4% paraformaldehyde for 30 min, stained with 0.1% crystal violet for 30 min, and finally photographed for quantitative analysis by ImageJ.

Cell apoptosis

Transfected tumor cells were seeded into 12-well plates and cultured with 5-FU for 48h. Cells were digested with Trypsin (without EDTA) and finally resuspended in the binding buffer with PI (10μL) and Annexin V-APC (5μL) for 5∼10min according to the operation manual. The cells were analyzed with a flow cytometer-BD FACS Melody (BD Bioscience, Franklin Lake, NJ, USA).

Immunofluorescence staining

Immunofluorescence staining of Figures 3 and 4 was performed using the Quadruple-Fluorescence Kit (Immunoway). First, dewax the paraffin sections and perform antigen retrieval. Next, inactivate endogenous peroxidase activity and block the tissue samples. Incubate the samples with the appropriate primary antibodies at 4°C for 8 h. After washing with PBST, add the corresponding secondary antibodies and incubate at room temperature for 30 min. Following PBST washing, add the appropriate fluorescent dyes and incubate at room temperature for 10 min. Once the staining is complete, place the samples in a recovery box, add the antibody stripping solution, and maintain the temperature above 95°C for 15 min. After the samples have cooled to room temperature, repeat the incubation with the primary antibodies following the antibody stripping step, sequentially labeling all markers with specific fluorescence. The primary antibodies added include: D-594 fluorescently labeled CK20 (Anti-Cytokeratin 20, abcam), D-488 fluorescently labeled HEP (Anti-Hepatocyte Specific, abcam), D-525 fluorescently labeled CD14 (Immunoway), and D-647 fluorescently labeled CD163 (Immunoway). Finally, label the cell nuclei with DAPI. Image analyses were comducted using an Olympus BX53 inverted epifluorescence microscope or a Zeiss LSM 980 confocal microscope. Five areas from each section were randomly selected to count the percentage of positively stained cells using Image-Pro Plus 6.0 software.

Immunofluorescence staining of Figures 5 and 6 was performed as previously described.[90] Tumor cells or tissues were directly fixed with 4% paraformaldehyde, permeabilized with 0.3% Triton X-100, and incubated with the primary antibodies such as anti-Ki-67 (1:200; Proteintech) for HUVECs staining and anti-phospho-STAT3 (Tyr705) (1:200; CST) for tumor cell stainings or anti-CD31 (1:200; Proteintech) for tissue stainings overnight at 4°C. Next, the cells or tissues were incubated with the secondary antibodies Alexa Fluor 647-labeled Goat Anti-Rabbit IgG (1:500; Beyotime) for 1 h at room temperature. Finally, the cells or tissues were incubated for 10 min with DAPI diluted with methanol to stain the nucleus. Images were obtained with fluorescence and laser confocal microscopes (A1-DUVB-2, Nikon) for quantitative analysis by ImageJ.

Immunohistochemistry staining

Formalin-fixed tissue samples of mouse or human CRC liver metastasis tissues were embedded into paraffin and processed into 2∼4μm sections. Hematoxylin-eosin (HE) staining was performed according to standard procedures. CRLM mainly contains 3 different histopathological growth patterns (HGPs): desmoplastic HGP (DHGP), pushing HGP (PHGP), and replacement HGP (RHGP).[31] The types of histopathological growth patterns were evaluated using ImageJ software (NIH), and the full-length pixels of RHGP (a), DHGP (b), and PHGP (c) in the liver-tumor interface of each image were calculated and converted into micrometers. The percentage RHGP was then quantified according to the following formula: a/(a + b + c)×100. The same calculation method was used for the quantification of DHGP and PHGP. Furthermore, from each HE-stained slide, 1–5 observation fields containing the tumor boundary were randomly selected for statistics. For antigen retrieval, mounted sections were put into a pressure cooker after being treated with sodium citrate. Slides were placed in 3% H_2O_2 for 10 min at room temperature, blocked in 5% BSA for 1 h and incubated with primary antibodies against anti-Ki-67 (1:2000; Proteintech) and anti-CD31 (1:2000; Proteintech) overnight at 4°C. Secondary antibody goat anti-rabbit HRP IgG (ZSGB-BIO, PV6001) and DAB were used to perform the immunostain. Counterstaining was developed using hematoxylin. Finally, images were obtained using a microscope (BX51, Olympus).

Co-IP analysis

As described previously in our study,[90] cell lysates of stably transfected cells were collected and incubated with a specific primary antibody, anti-FLAG (1:200; Cat# 14793, CST), anti-phospho-STAT3 (Tyr705) (1:200; Cat# 9145, CST), or anti-SHP2 (1:200; Cat# 3397, CST), and mixed with protein A/G-Sepharose beads (7 Sea Biotech) overnight at 4°C. After extensive washing, the beads were boiled in 4×SDS-PAGE loading buffer for 5 min and analyzed by immunoblotting with specific antibodies to detect the protein complex.

siRNA transfection

Ablation of STAT3 in tumor cells was performed by transfection with siRNA duplex oligos, which were synthesized by Ribobio Company. Cell transfection was performed with Lipofectamine 2000 (Invitrogen) and replaced with a fresh medium after transfection for 12∼24h to further culture the cells for 48 h. The sequences used in this study are #1 GGCGTCCAGTTCACTACTA and #2 CATCGAGCAGCTGACTACA. Western blotting and qPCR were used to verify the efficiency of the sequence.

QUANTIFICATION AND STATISTICAL ANALYSIS

For binary outcomes, 95% two-sided CIs were constructed using the Clopper–Pearson method. Fisher's exact test for independence was utilized to examine the relationship between two categorical variables and Mann-Whitney U test was conducted to assess the independence between a continuous variable and a binary categorical variable. Each experiment was repeated at least three times in this study. Differences between experimental groups were assessed using Student *t* tests, one-way or two-way ANOVA. All data were analyzed using GraphPad Prism 7.0 software (RRID: SCR_002798). All values are presented as mean ± SD, and statistical significance was noted as a p value of <0.05.

Cell Reports Medicine, Volume *5*

Supplemental information

Genetic and microenvironmental evolution of colorectal liver metastases under chemotherapy

Min Shi, Yingxi Yang, Na Huang, Dongqiang Zeng, Zongchao Mo, Jiao Wang, Xiaomeng Zhang, Ran Liu, Chunlin Wang, Xiaoxiang Rong, Zhenzhen Wu, Qiong Huang, Haixia Shang, Jihong Tang, Zhaojun Wang, Jianan Cai, Genjie Huang, Yijin Guan, Jian Guo, Quanhua Mu, Jiguang Wang, and Wangjun Liao

A Baseline patient characteristics according to response status of first-line therapy

	Total (n=48)	R (n=27)	NR (n=21)	p-Value
Age at enrollment (years)				
Median (range)	55.5 (29-79)	57.4 (33-73)	53.1 (29-79)	0.33[a]
Sex (n (%))				
Female	20 (42)	10 (37)	10 (48)	0.56[b]
Male	28 (58)	17 (63)	11 (52)	
Stage (n (%))				
IVA	17 (35)	7 (26)	10 (48)	0.14[b]
IVB	23 (48)	16 (59)	7 (33)	0.09[b]
IVC	8 (17)	4 (15)	4 (19)	0.72[b]
Primary tumor site (n (%))				
Left	37 (77)	19 (70)	18 (86)	0.30[b]
Right	11 (23)	8 (30)	3 (14)	
Smoking history (n (%))				
Yes	10 (21)	7 (26)	3 (14)	0.48[b]
No	38 (79)	20 (74)	18 (86)	
Alcohol drinking history (n (%))				
Yes	4 (8)	2 (7)	2 (10)	1.00[b]
No	44 (92)	25 (93)	19 (90)	
Lung metastases (n (%))				
Yes	20 (42)	15 (56)	5 (24)	0.04[b]
No	28 (58)	12 (44)	16 (76)	
Number of metastases (n (%))				
1 (liver-only)	16 (33)	6 (22)	10 (48)	0.12[b]
>=2	32 (38)	21 (78)	11 (52)	
First-line therapy (n (%))				
BVZ+mFOLFOX6	35 (73)	21 (78)	14 (67)	0.52[b]
BVZ+FOLFIRI	13 (27)	6 (22)	7 (33)	

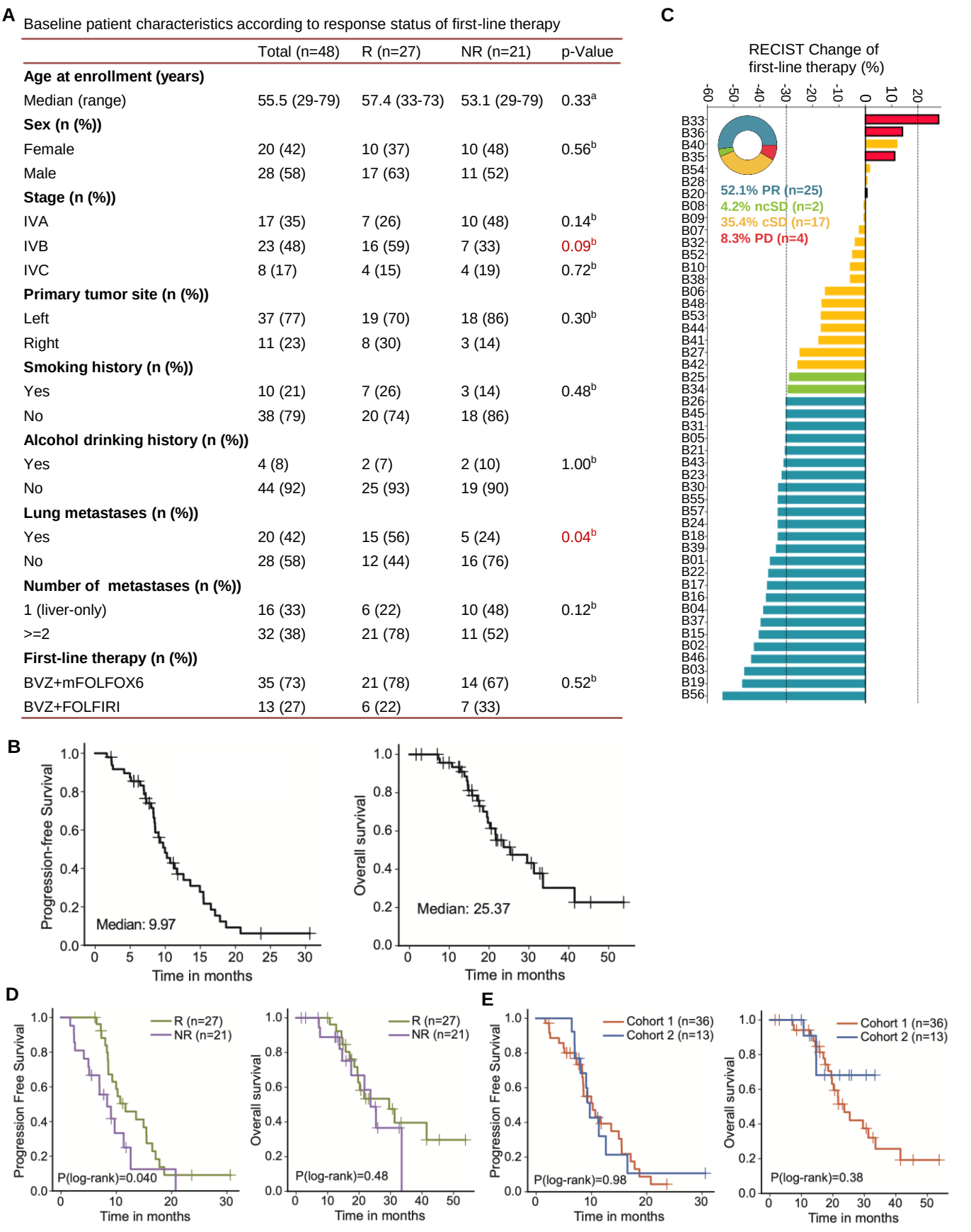

Figure S1. Clinical information of the enrolled CRLM patients, related to Figure 1.
(**A**) Relationship between baseline patient characteristics and their response status to first-line therapy. P-values were calculated by either Mann-Whitney U test (labelled with "a") or two-sided Fisher's exact test (labelled with "b"). (**B**) Kaplan–Meier estimates of progression-free survival (left panel) and overall survival (right panel) for all enrolled patients. (**C**) Waterfall plot demonstrating best percentage reduction of tumor burden with the guideline (Figure 1C) for first-line therapy. The vertical dotted line represented the threshold of 30% regression and 20% progression in tumor size. Patients with new lesions were highlighted with black border. (**D**) Kaplan–Meier estimates of progression-free survival (left panel) and overall survival (right panel) for first-line Responders (R) and Non-responders (NR). (**E**) Kaplan–Meier estimates of progression-free survival (left panel) and overall survival (right panel) as per treatment arm.

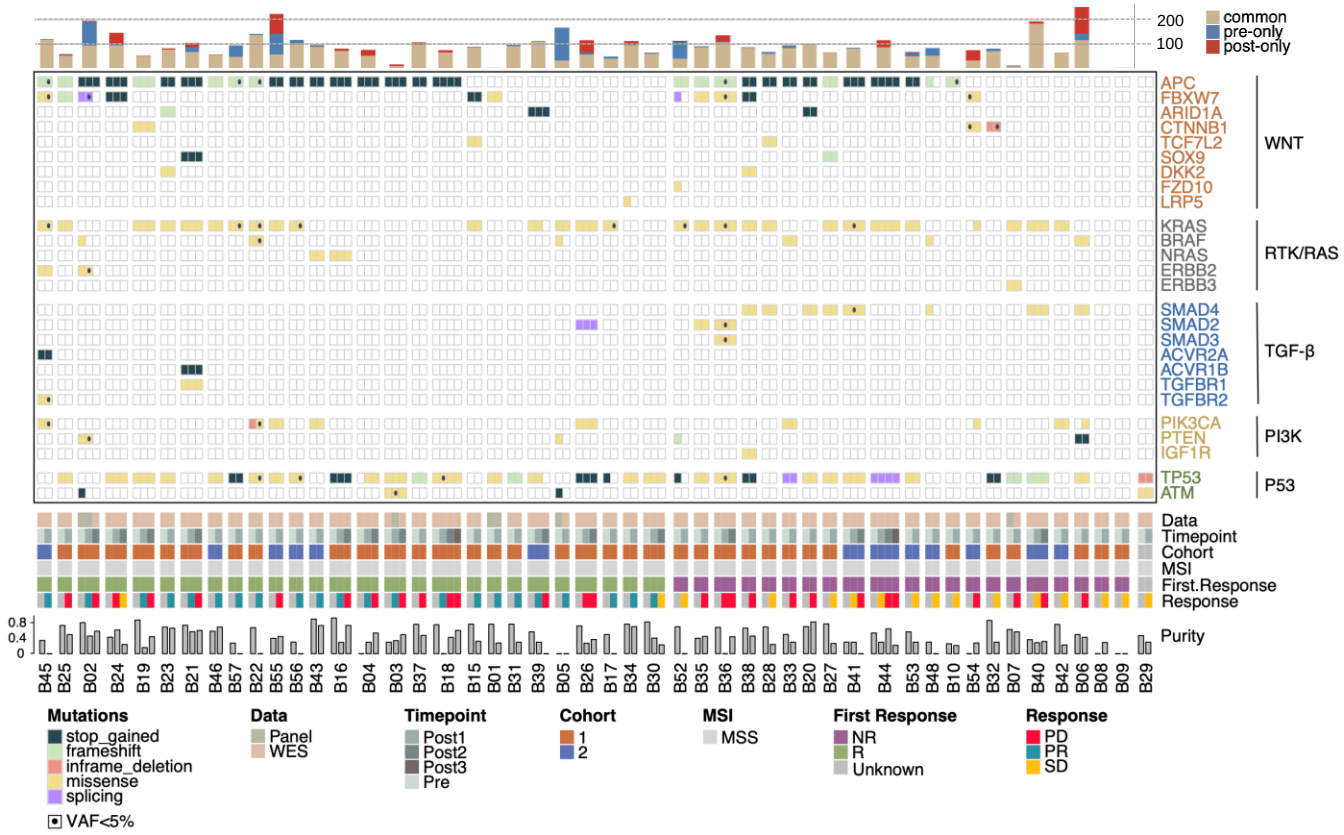

Figure S2. Somatic mutational landscape of pre- and post-treatment CRLM tumors, related to Figure 2.
Nonsynonymous mutations in 115 matched diagnostic and treated tumor samples. The top panel demonstrated the number of somatic mutations that are shared (common), pre-treatment private or post-treatment private. The middle panel included somatic mutations of known CRC driver genes that were clustered by pathway. The third panel annotated each sample by WES/panel, pre-/post-treatment, MSI status, response status of first-line therapy and timepoint response. Each column represents a sample and patients were ordered by first-line response. Purity (estimated by Facets) of each tumor sample was showed at the bottom panel. MSS. microsatellite stable.

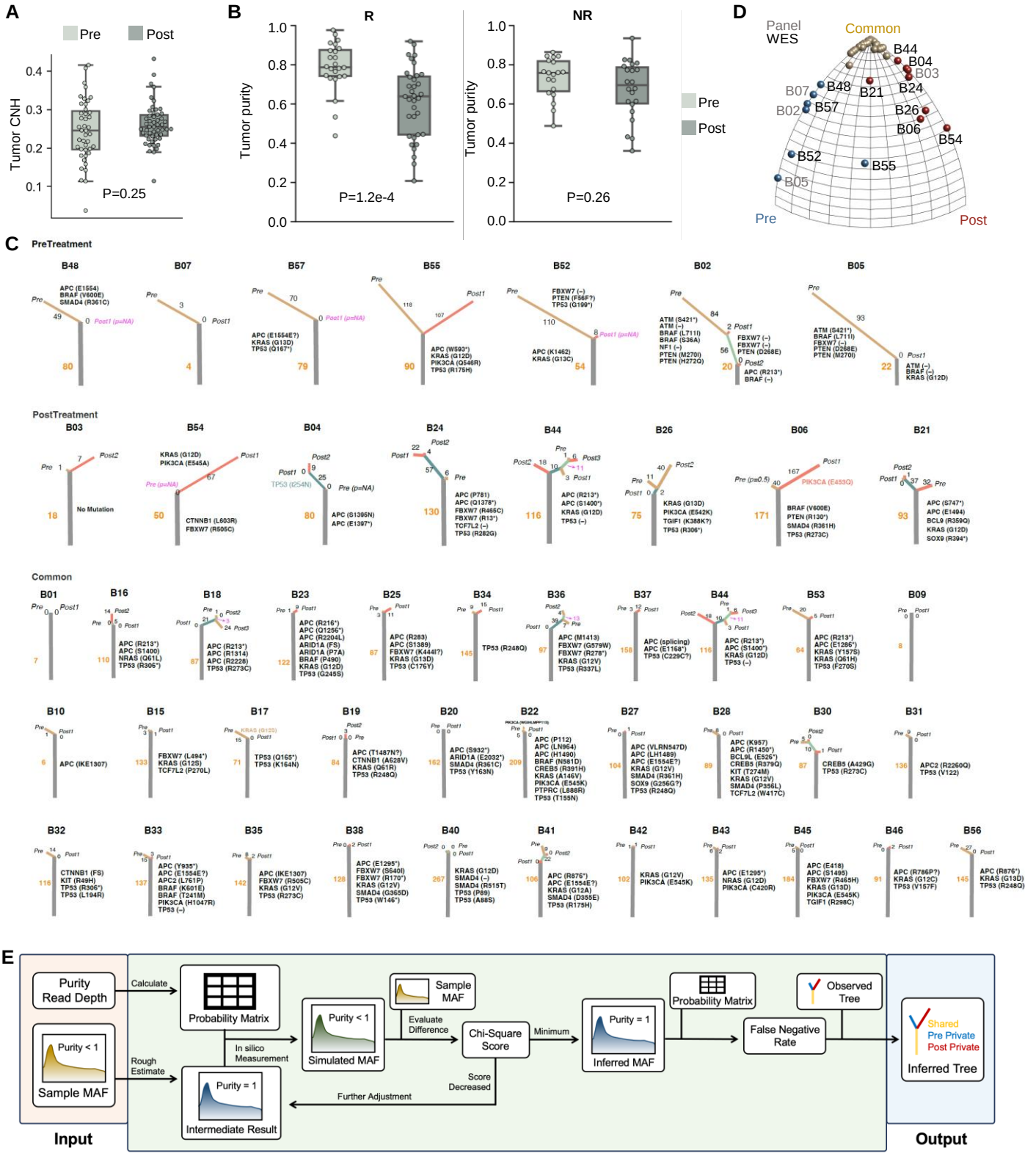

Figure S3. CLRM evolution under BVZ-based chemotherapy, related to Figure 2.
(**A**) Chromosomal copy number heterogeneity (CNH) of pre-treatment tumors versus post-treatment tumors. P-value was calculated by Mann-Whitney U test**.** (**B**) Comparison of tumor purity in the treatment-responsive group (left) and the non-responsive group (right) before and after treatment. P values were determined by the Mann-Whitney U test. (**C**) Phylogenetic trees of 49 CLRM patients based on genomic sequencing of their matched pre- and post-treatment tumor samples. (**D**) Moduli space of evolutionary trees before ETRIP adjustment. (**E**) Overview workflow of ETRIP pipeline (see details in STAR Methods).

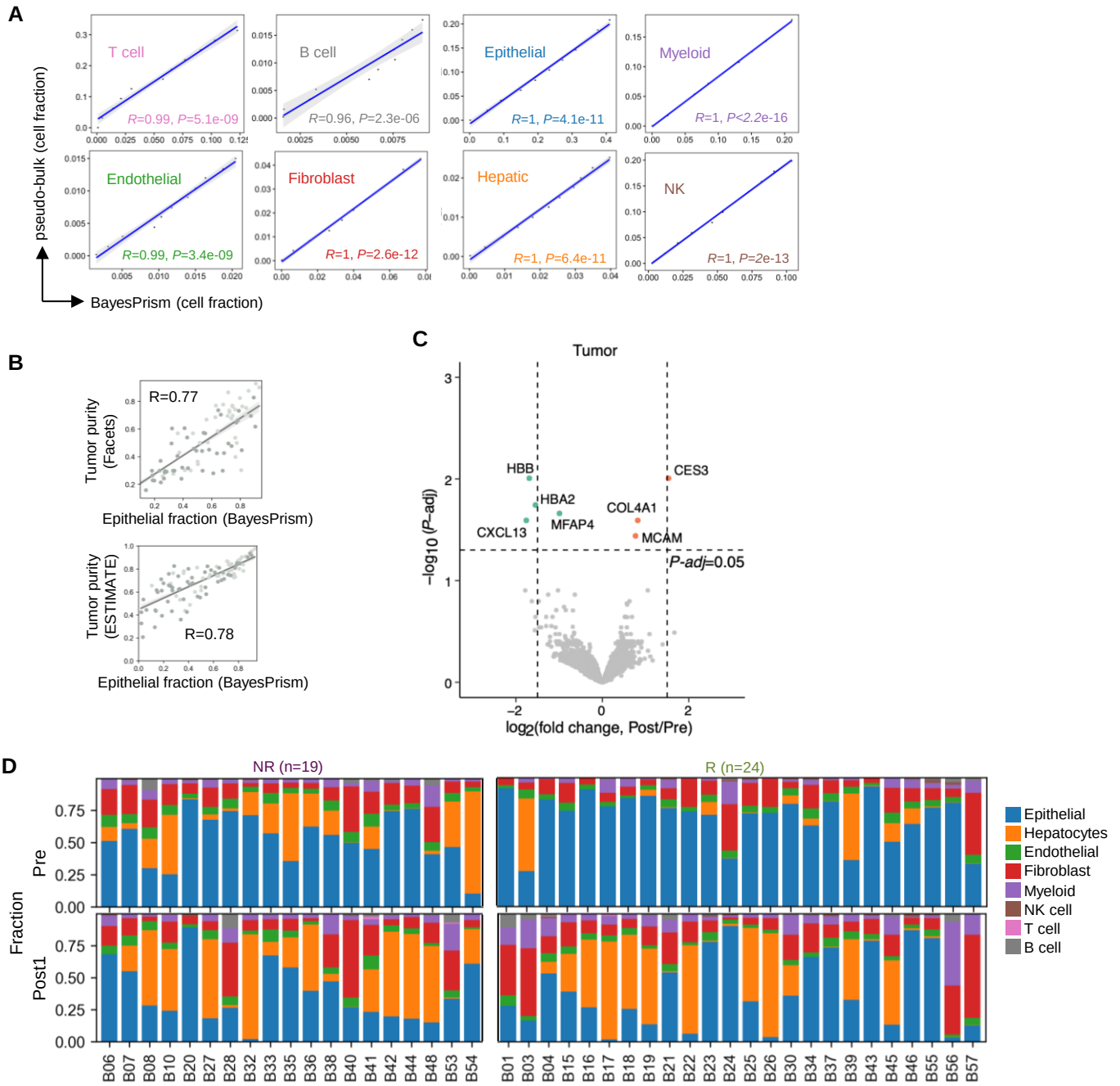

Figure S4. Tumor microenvironment profile calculated by BayesPrism, related to Figure 3.
(**A**) Scatter plots showing the correlation between the ground truth and the BayesPrism-inferred proportion for each cell type. Gene expression profiles were obtained from synthetic mixtures composed of diverse combinations of single cells. (**B**) Scatter plots showing the correlation between the tumor purity and epithelial cell fraction inferred by BayesPrism. The tumor purity was inferred by Facets with DNA-seq (left panel) or ESTIMATE with RNA-seq (right panel). (**C**) Volcano plot showing DEGs in post-treatment tumors versus pre-treatment tumors. The tumor gene expression was estimated by BayesPrism and differential gene expression was analyzed using DESeq2. (**D**) The cell type composition of each sample with pre-treatment (Pre) on the top and post-treatment (Post1) on the bottom.

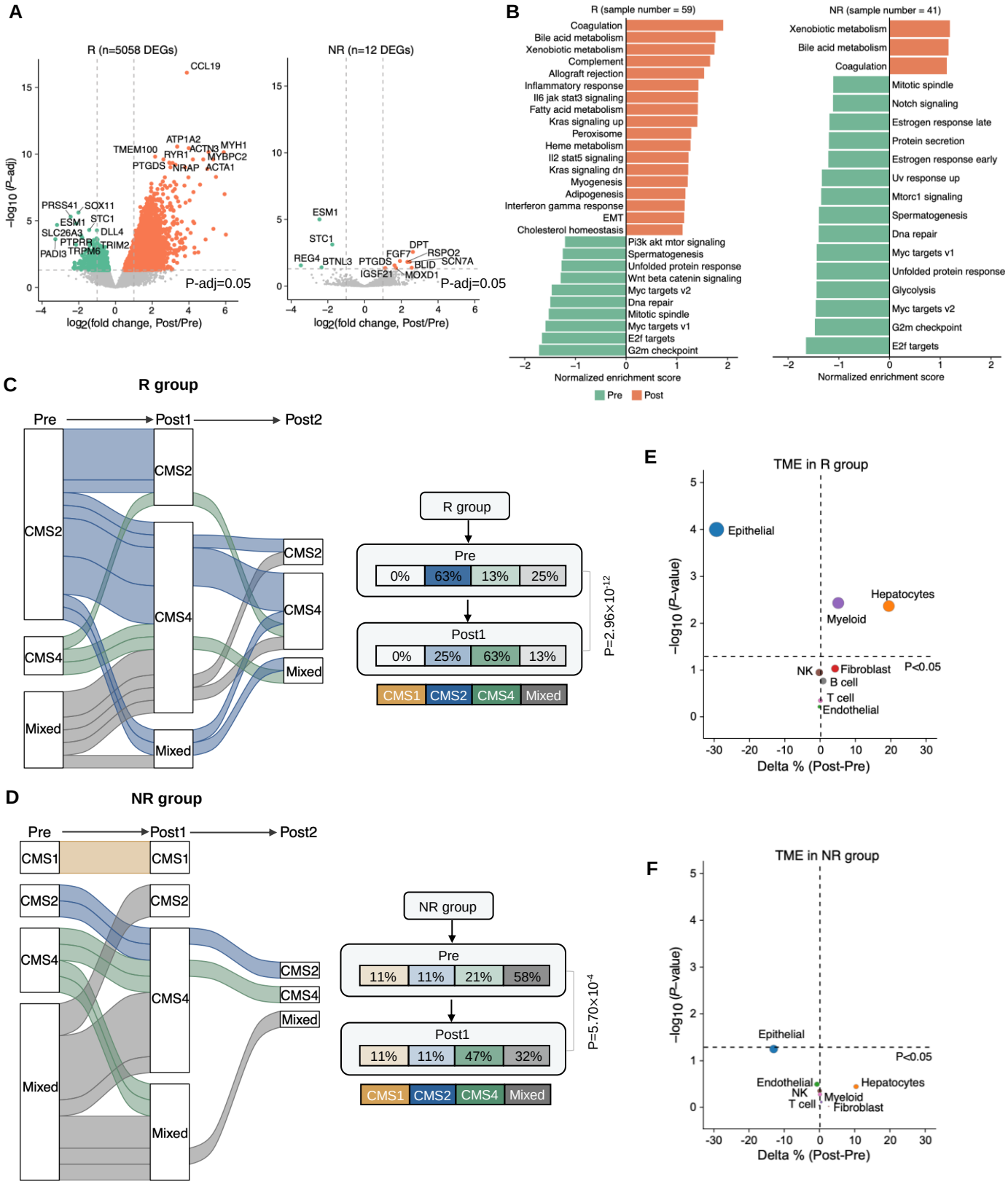

Figure S5. Transcriptional changes before and after treatment by the response group, related to Figure 3.

(**A**) Volcano plot showing DEGs in post-treatment versus pre-treatment tumor samples in responder (left) and non-responder (right) group. The log2 foldchanges were extracted from DESeq2 and P-value: the Wald test. P values were then adjusted for multiple testing using the Benjamini-Hochberg procedure (P-adj). Significantly DEGs with P-adj < 0.05 were colored and selected top genes were labelled. (**B**) GSEA showing the enriched pathways in baseline compared with post-treatment samples in responder (left) and non-responder (right) group. (**C**-**D**) Alluvial plot showing CMS transition under treatment (left panel) in responder (C) and non-responder (D) group. The right panel displayed the change of proportion in each subtype. P-value: Chi-squared test. (**E**-**F**) Bubble plot demonstrating the percentage changes of various cell types between post-treatment and pre-treatment samples in responder (E) and non-responder (F) group. The relative percentage of each cell type within the bulk RNA-seq samples was inferred by the deconvolution method BayesPrism, with the public CRLM scRNA-seq data (dbGAP: phs001818.v3.p1) as a reference. The change in percentage (Delta %) was calculated by subtracting the average cell type proportions in treated samples from those in baseline samples. The bubble size was proportional to -log10(P-value). P-value: Mann–Whitney U-test.

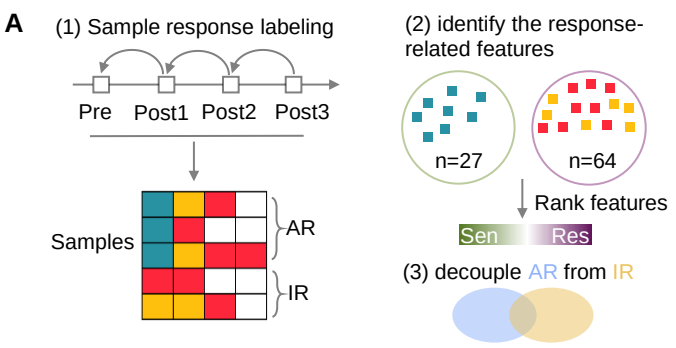

B

AR	Res	Sen
DNA mutation	0	0
Mutation burden	0	0
CNA	0	0
CNH	0	0
Tumor purity	0	1
RNA gene expression	80	20
CMS subtypes	1	1
Cell type proportion	2	2

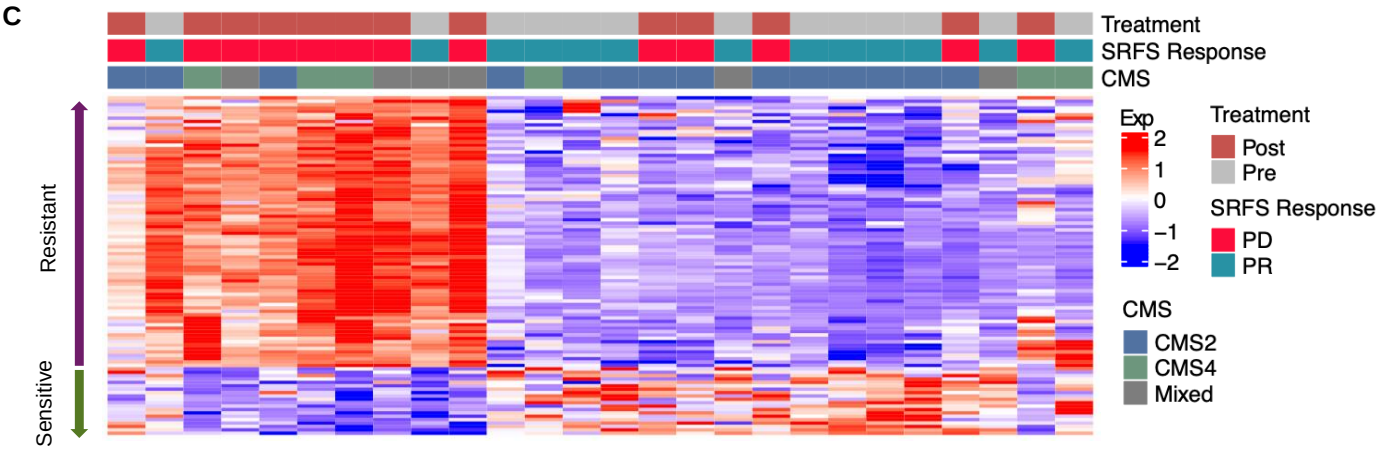

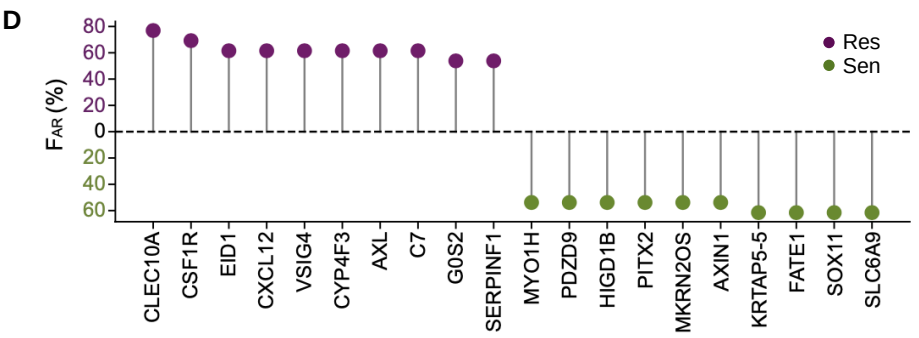

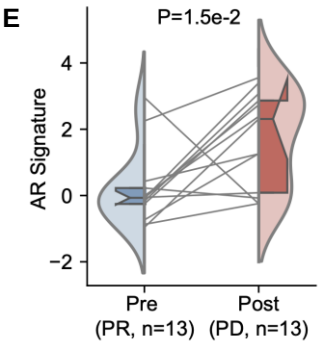

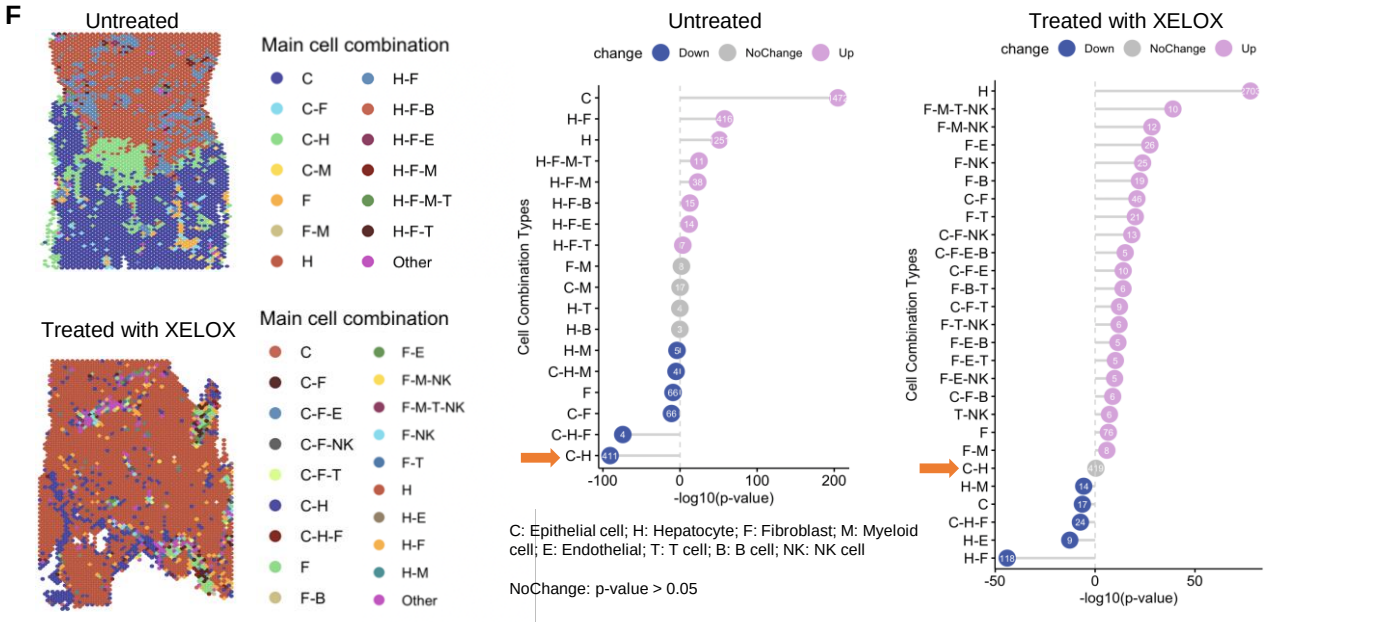

Figure S6. Transcriptomic analysis of sensitive versus resistant samples under treatment, related to Figure 3.
(**A**) Overview of the Sample-based Response Feature Selection (SRFS) approach for identifying treatment response-related factors. Step 1: pooling samples, and re-annotating the sample responses based on their future response labels. Step 2: categorizing samples into sensitive (PR) or resistant (SD or PD) groups, evaluating genomic and transcriptomic features for discriminative potential, and classifying them as resistance (Res)- or sensitivity (Sen)-related. Step 3: decoupling AR and IR features based on the IR and AR contribution thresholds (see STAR Methods). (**B**) Statistics of AR-related features identified by SRFS. (**C**) Heatmap showing the expression of AR-related genes from 13 patients with baseline (PR, n=13) and matched treated recurrent samples (PD, n=13). (**D**) Lollipop plot showing the top 10 genes related to AR. The y-axis represents the fraction of patients whose AR was potentially contributed by certain gene expression. (**E**) Comparisons of AR signatures (see Methods) between pre-treatment PR samples and matched post-treatment PD samples in 13 patients. This analysis focused on patients who initially showed a PR but later progressed to PD. P value: two-sided paired t-test. (**F**) Spatial distribution of different cell types within a pre-treatment sample (left top panel) and a sample after treatment (left bottom panel). Lollipop plots showed spatial interactions or spatial exclusion of cell type combinations before (middle panel) and after (right panel) therapy. The number in dots represented number of spots harboring the cell type combination. The color of the dots indicated whether spots with the cell type combination were significantly enriched in the sample with red representing significantly enriched, blue representing significantly depleted, and grey representing not significant (p-value > 0.05).

A

IR	Res	Sen
DNA mutation	2	0
Mutation burden	0	0
CNA	0	4
CNH	0	0
Tumor purity	0	1
RNA gene expression	47	42
CMS subtype	0	1
Cell type proportion	1	2

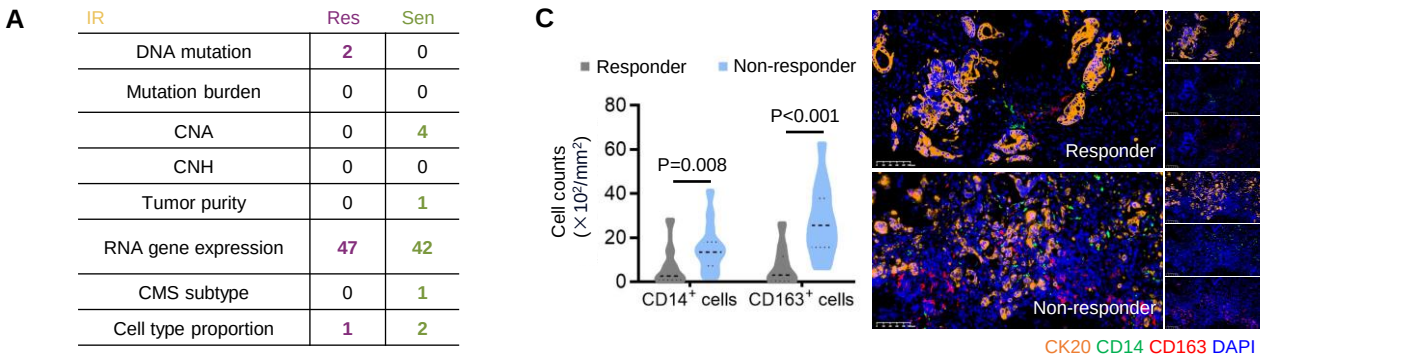

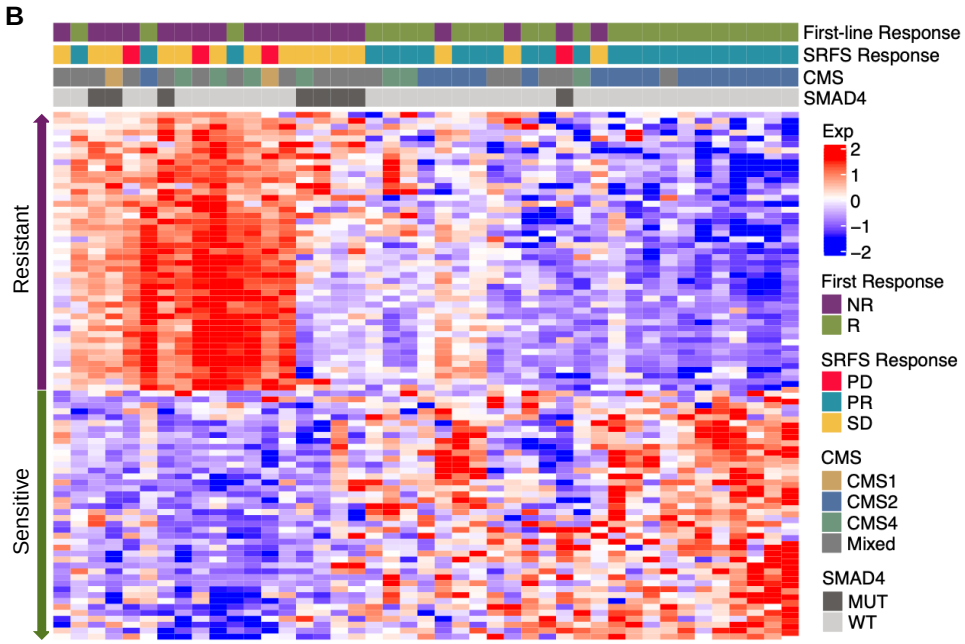

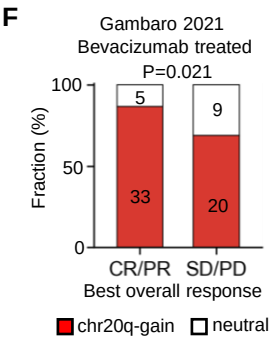

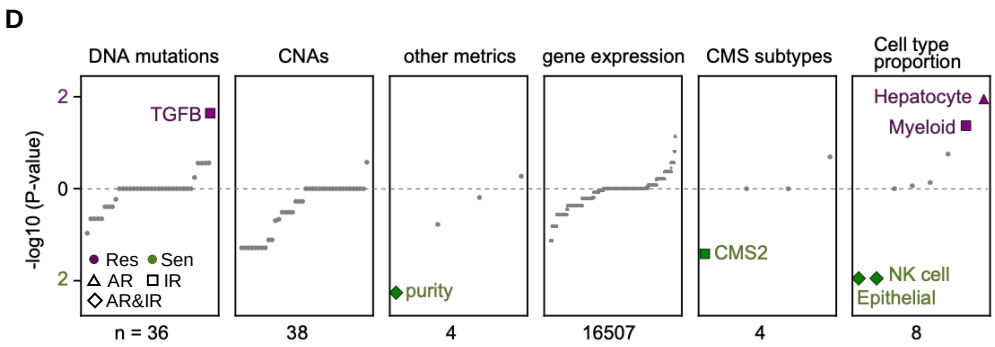

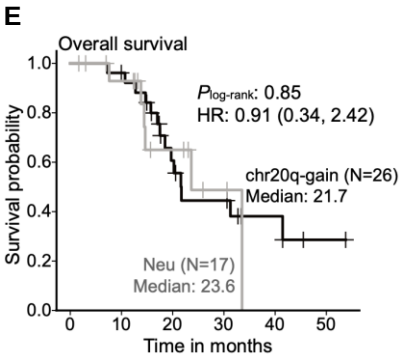

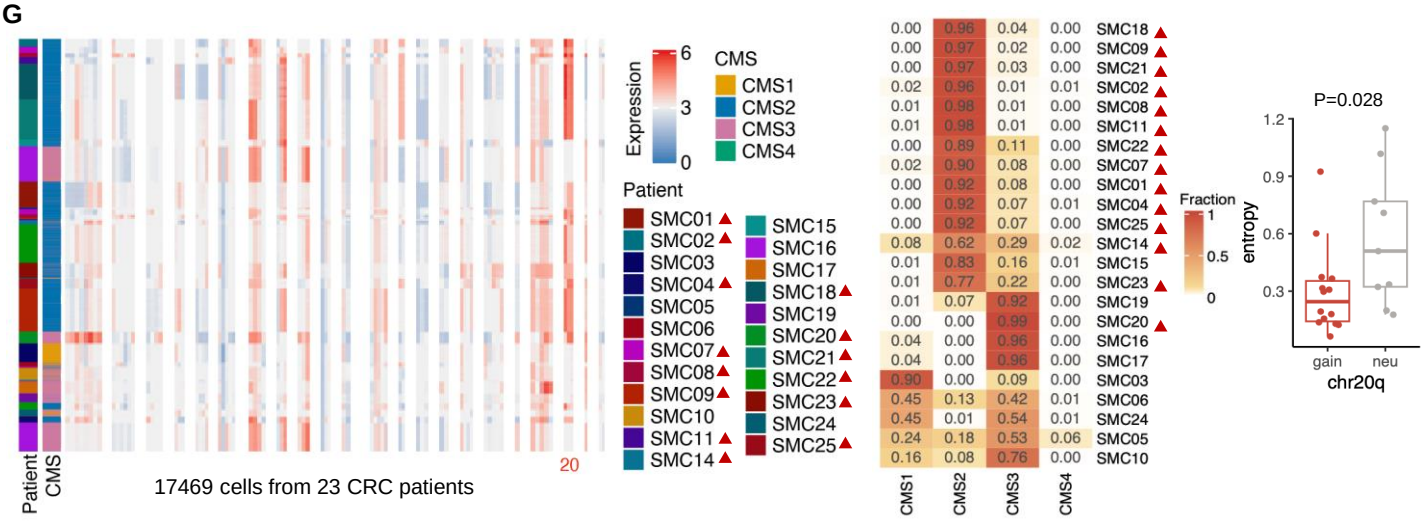

Figure S7. chr20q gain were associated with IR, related to Figure 4.
(**A**) Statistics of the detected AR-related feature by SRFS. (**B**) Heatmap showing the expression profile of IR-related genes in pre-treatment tumor samples. (**C**) Quantification (left) and representative IF images (right) of monocytes (CD14+) and macrophages (CD163+) in hepatic metastasis samples from responders (n = 10) and non-responders (n = 17). P value: Mann-Whitney U test. Scale bars = 100 μm. (**D**) Different types of features prioritized by SRFS in patients with RHGP. Each dot represented an individual feature and significant AR or IR-associated features were highlighted in green (pro-sensitive) or purple (pro-resistant). (**E**) Kaplan–Meier estimates of overall survival for patients segregated by chr20q-gain. (**F**) Chr20q gain was associated with response to BVZ-based therapy in an independent cohort reported by *Gambaro 2021*. CR: complete response. P value: exact binomial test. Pre-treatment CRLM patients treated with Oxaliplatin, Irinotecan or Oxaliplatin + Irinotecan + BVZ were included. (**G**) Representative CNV heatmaps (left) from inferCNV analysis from tumor cells in CRC patients (GSE132465). The patients with chr20q gain were labelled by a red triangle. Each single cell was annotated with a CMS subtype determined by the highest similarity scores of each tumor cell to the reference CMS gene expression programs (*Guinney J 2015*). CMS distribution in each patient (middle). Comparison of the entropy scores in chr20q-gain versus chr20q-neutral patients (right). Lower entropy values indicated a more stable cellular state. P value: Mann-Whitney U test.

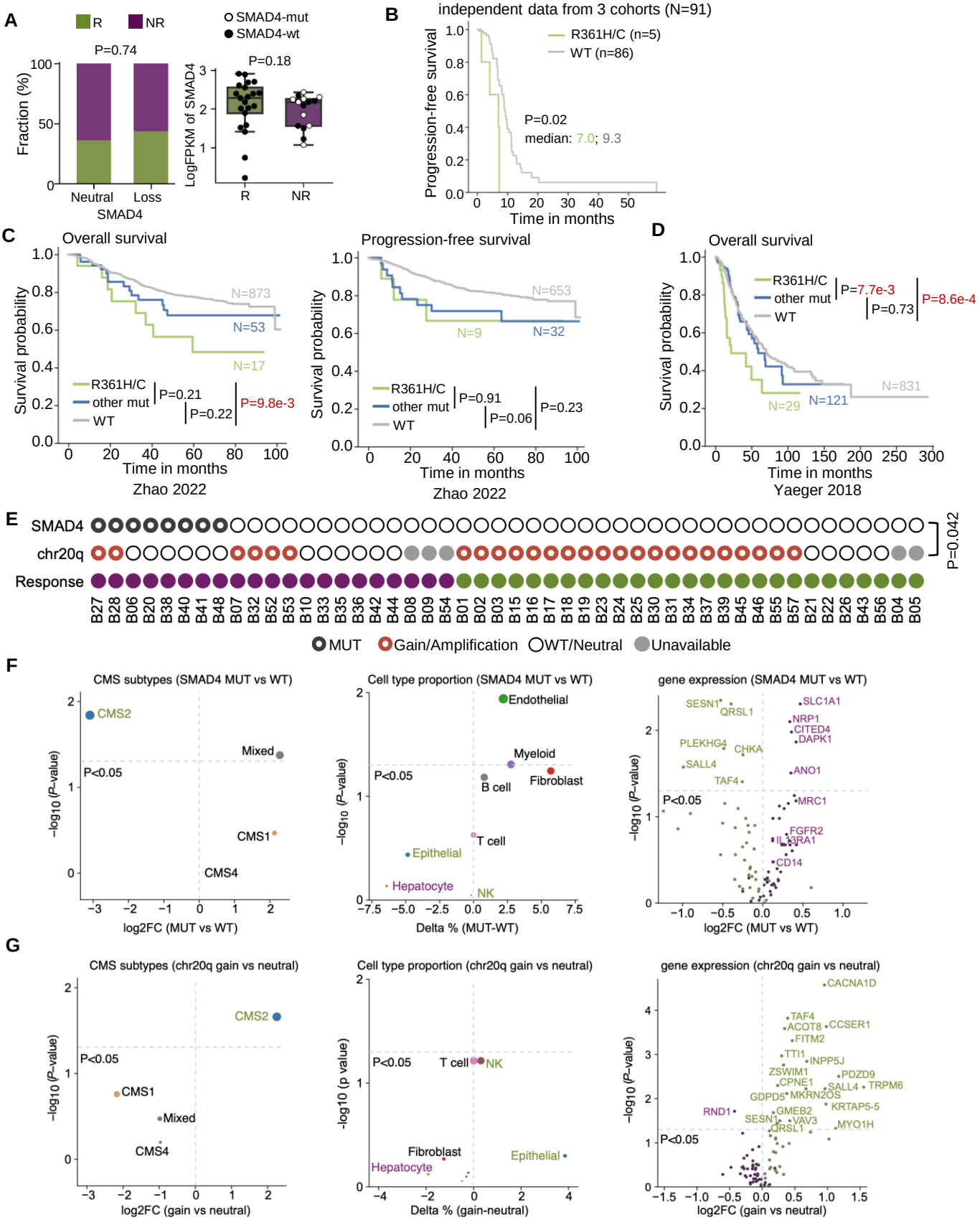

Figure S8. *SMAD4* mutations was associated with IR, related to Figure 4.

(**A**) Bar plot (left) comparing the non-responding frequency in SMAD4 copy number loss and neutral groups before treatment. P-value was calculated by one-proportion z-test. Box plot (right) showed the expression level of SMAD4 for pre-treatment samples from either responders or non-responders. P-value: Mann-Whitney U test. (**B**) Kaplan–Meier estimates of progression-free survival in the independent Chinese cohorts segregated by SMAD4$^{R361H/C}$ mutation status defined by ddPCR. (**C**) Kaplan–Meier estimates of overall survival (left panel) and progression-free survival (right panel) in another independent cohort, Chinese ChangKang CRC cohort stratified by SMAD4 mutation status. Patients diagnosed with pathological stage IV were included, irrespective of their treatment status. (**D**) Kaplan–Meier estimates of overall survival in MSK CRC cohort stratified by SMAD4 mutation status. All patients were included, irrespective of their treatment status. (**E**) Exclusivity between SMAD4 mutations and gain of chr20q. P-value was calculated by two-sided Fisher's exact test. (**F-G**) CMS subtype distribution (left), relative percentage of cell types (middle), and the expression of IR-related genes (right) in SMAD4-mutant versus SMAD4-wildtype samples (F), as well as chr20q-gain versus chr20q-neutral samples (G) prior to treatment. Each dot represented an individual feature and the IR-associated features were highlighted in green (pro-sensitive) or purple (pro-resistant) detected by our method SRFS. P values: two-sided Fisher exact test (left) and Mann-Whitney U test (middle and right), respectively.

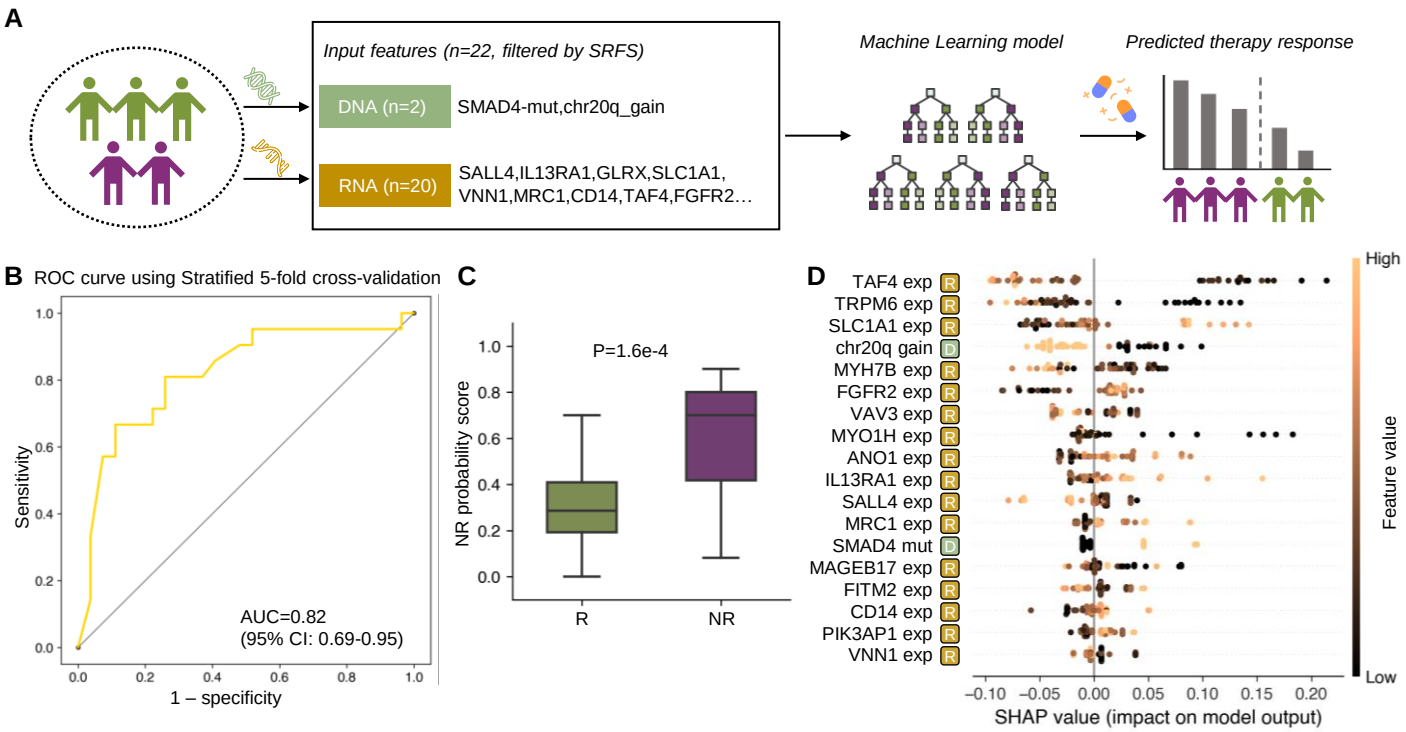

Figure S9. Machine learning model designed for the early prediction of drug resistance or sensitivity in CRLM patients, related to Figure 4.

(**A**) Schematic illustration of machine learning model to predict BVZ-C therapy responders and non-responders. Input features (n=22) included the IR-related features (DNA: SMAD4 mutation and chr20q gain; RNA: top ten pro-sensitive and pro-resistant genes) selected by SRFS. Bayesian ridge were used for imputation of missing data in 48 CRLM pretreatment samples and a 22-feature prognositic model (Random Forest) was trained with hyperparameters optimization. (**B**) Receiver operating characteristic (ROC) curves showing the model performance in stratified 5-fold cross-validation. (**C**) Model probability score distributions in responder and non-repsonder samples. P value was determined by Mann-Whitney U test. (**D**) Shapley additive explanation (SHAP) value of each feature in the model.

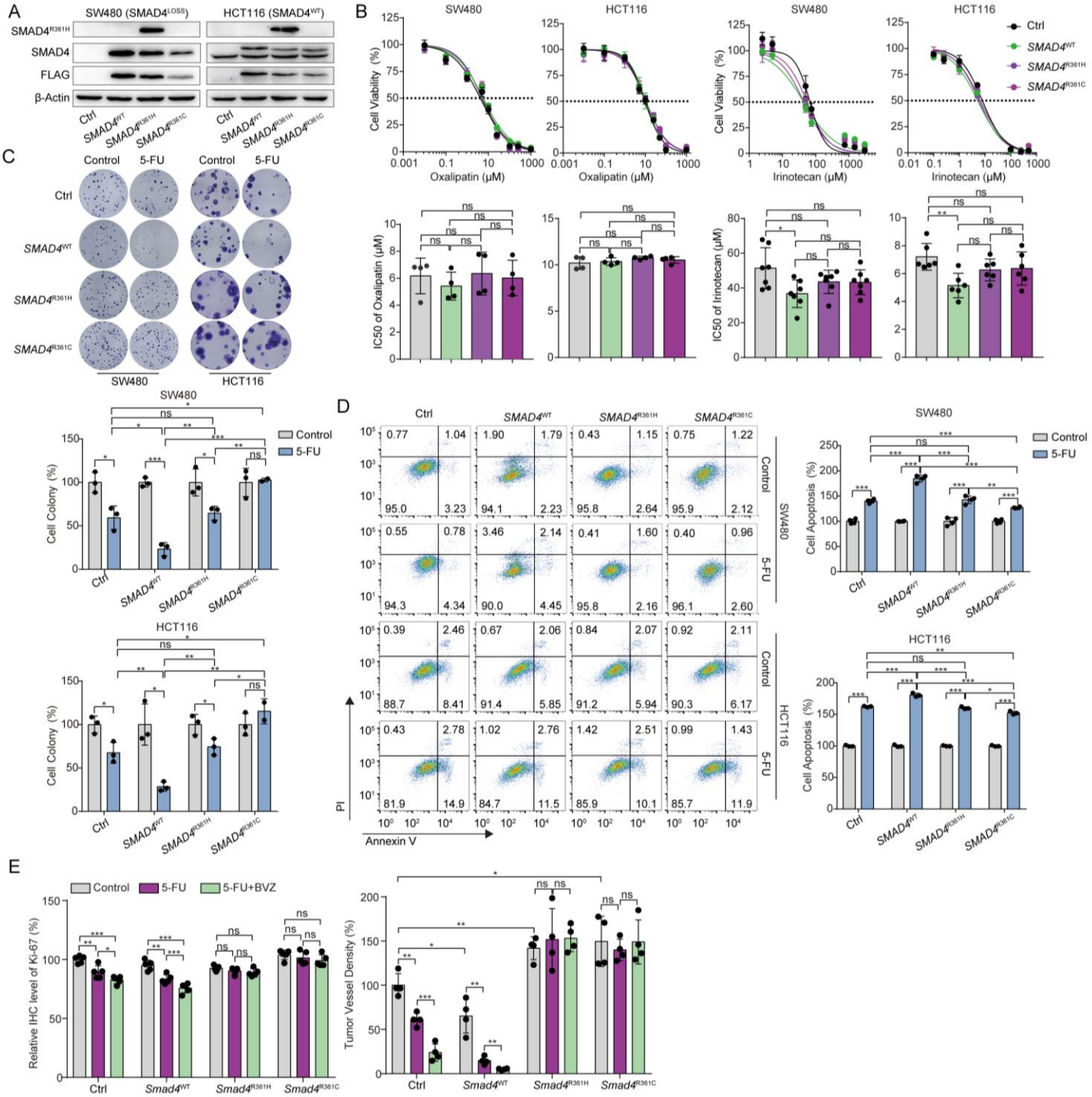

FigureS10. *SMAD4*$^{R361H/C}$mutationspromote5-FUandbevacizumabresistanceinCRC, related to Figure 5.

(A) Western blotting confirming ectopic expression of SMAD4, SMAD4$^{R361H/C}$, and FLAG in retrovirally transduced SW480 and HCT116 cells. **(B)** Cell viability assay of SW480 and HCT116 cells following treatment with Oxaliplatin or Irinotecan for 48 hours, IC50 value of Oxaliplatin or Irinotecan (bottom) and representative curve-fitting graphs (top) are shown (n=4,6). **(C)** Colony formation assay and the quantitative graph of SW480 and HCT116 cells exposed to 5-FU for two weeks. Representative images (top) and the quantification (bottom) of the numbers of colonies are shown (n=3). **(D)** Flow cytometry of apoptosis and the quantitative graph of SW480 and HCT116 cells following treatment to 5-FU for 48h (n=3,4). **(E)** Transplanted subcutaneous tumors with treatment are collected, and the quantification for immunohistochemical (IHC) staining of tumor-proliferation marker Ki-67 and immunofluorescence of tumor vascular markers CD31 are shown (n=4,5). Data are graphed as the mean ± SD; *, P < 0.05; **, P < 0.01; ***, P < 0.001; ns, nonsignificant, P > 0.05.

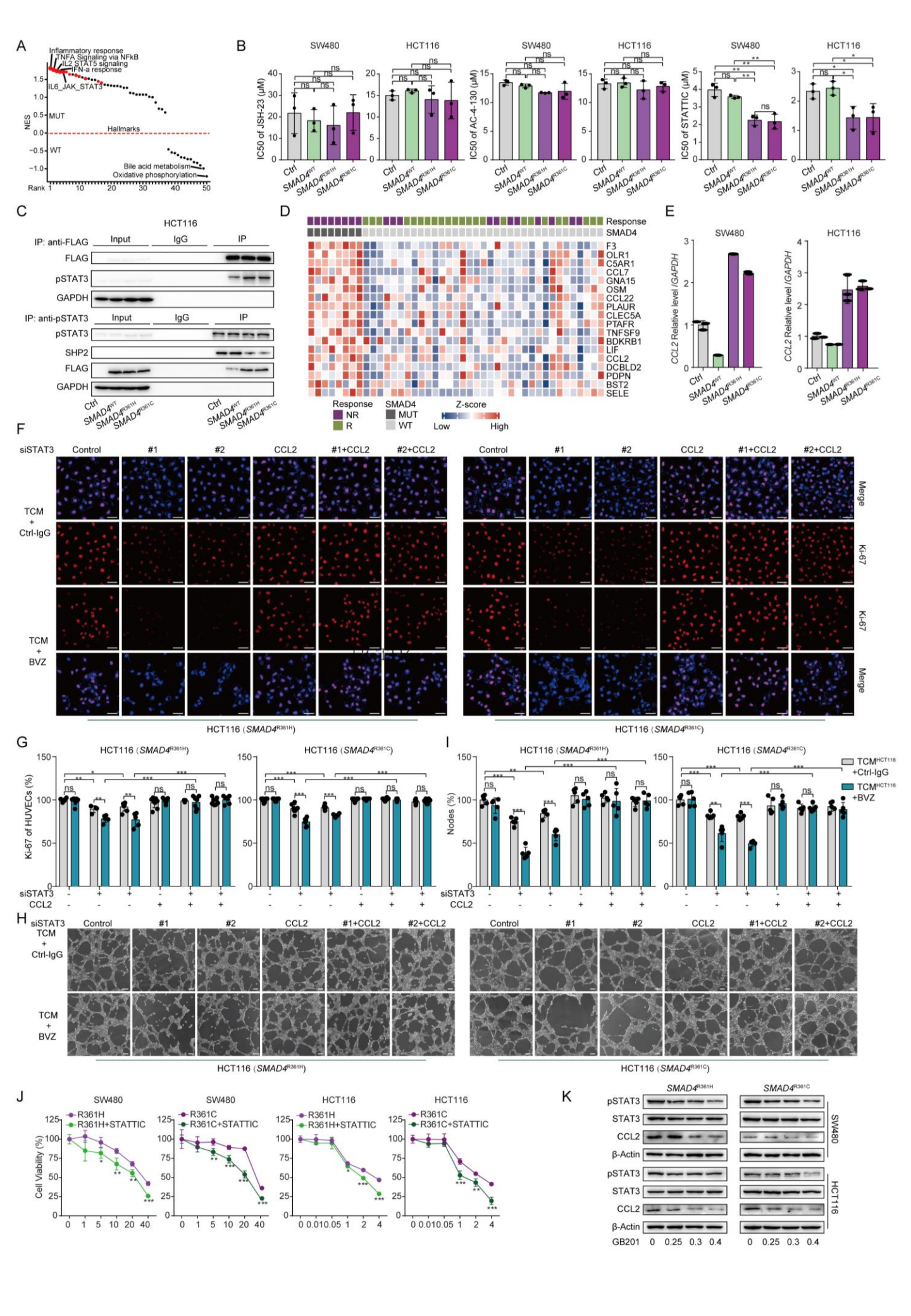
A
Inflammatory response
TNFA Signaling via NFkB
IL2 STAT5 signaling
IFN-a response
IL6_JAK_STAT3
MUT
Hallmarks
WT
Bile acid metabolism
Oxidative phosphorylation
NES
Rank
B
SW480
HCT116
IC50 of JSH-23 (μM)
IC50 of AC-4-130 (μM)
IC50 of STATTIC (μM)
Ctrl
SMAD4WT
SMAD4R361H
SMAD4R361C
C
HCT116
IP: anti-FLAG
IP: anti-pSTAT3
Input
IgG
IP
FLAG
pSTAT3
GAPDH
SHP2
D
Response
SMAD4
NR
R
MUT
WT
Z-score
Low
High
F3
OLR1
C5AR1
CCL7
GNA15
OSM
CCL22
PLAUR
CLEC5A
PTAFR
TNFSF9
BDKRB1
LIF
CCL2
DCBLD2
PDPN
BST2
SELE
E
SW480
HCT116
CCL2 Relative level /GAPDH
F
siSTAT3
Control
#1
#2
CCL2
#1+CCL2
#2+CCL2
TCM + Ctrl-IgG
TCM + BVZ
Merge
Ki-67
HCT116 (SMAD4R361H)
HCT116 (SMAD4R361C)
G
HCT116 (SMAD4R361H)
HCT116 (SMAD4R361C)
Ki-67 of HUVECs (%)
siSTAT3
CCL2
I
HCT116 (SMAD4R361H)
HCT116 (SMAD4R361C)
Nodes (%)
TCMHCT116 +Ctrl-IgG
TCMHCT116 +BVZ
H
siSTAT3
Control
#1
#2
CCL2
#1+CCL2
#2+CCL2
TCM + Ctrl-IgG
TCM + BVZ
HCT116 (SMAD4R361H)
HCT116 (SMAD4R361C)
J
SW480
HCT116
R361H
R361H+STATTIC
R361C
R361C+STATTIC
Cell Viability (%)
K
SMAD4R361H
SMAD4R361C
pSTAT3
STAT3
CCL2
β-Actin
SW480
HCT116
GB201
0
0.25
0.3
0.4

FigureS11. *SMAD4*$^{R361H/C}$mutations induce resistance to BVZ therapy in CRC via the pSTAT3-CCL2 axis, related to Figure 6.
(A) Dot plot showing significantly enriched HALLMARK gene sets in CRLM with *SMAD4* mutation. **(B)** IC50 value of JSH-23 (NF-κB inhibitor), AC-4-130 (STAT5 inhibitor) and STATTIC (pSTAT3 inhibitor) in SW480 and HCT116 cells. **(C)** Co-IP assay shows a complex containing pSTAT3 and FLAG-SMAD4^{R361H}, SMAD4^{R361C}, or SHP2 in HCT116 cells. Top, FLAG antibody coprecipitating pSTAT3. Bottom, pSTAT3 antibody coprecipitating FLAG-SMAD4^{R361H}, SMAD4^{R361C}, or SHP2 protein. Input, protein expression in cell lysates detected by Western blot. IgG, negative control. IP, expression of compound coprecipitated by pSTAT3 or FLAG antibody. **(D)** Heatmap showing the DEGs in pre-treatment samples with versus without *SMAD4* mutation.The DEGs were identified using the limma method. The signicant DEGs (log2foldchange > 1 and P-value < 0.05) within the HALLMARK inflammatory response gene set are shown. **(E)** QPCR analysis of *CCL2* in SW480 and HCT116 cells with R361H/C mutation. **(F-I)** HCT116 cells with R361H/C mutations were transfected with siRNA of *STAT3* for 24h and replaced with fresh culture medium for 48h. Immunofluorescence staining for Ki-67 (red) and DAPI (blue) in HUVECs incubated with TCM collected from the indicated cells with *STAT3* silence, BVZ (0.25 mg/ml) and CCL2 protein (50 μg/ml). Representative immunofluorescence images **(F)** and the quantification **(G)** of MFI are shown (n=4~5). Scale bar, 100 μm; representative images **(H)** and quantification **(I)** of the formation of HUVECs tubules following incubation with TCM collected from the indicated cells with *STAT3* silence, and treatment with BVZ (0.25 mg/ml) and CCL2 protein (50 μg/ml) (n=4~5). Scale bar, 100 μm. **(J)** Cell viability of SW480 and HCT116 cells with R361H/C mutation exposed to 5-FU at the gradient concentrations, with or without combination with STATTIC. **(K)** Western blot analysis of pSTAT3 and CCL2 in SW480 and HCT116 cells with R361H/C mutations following treatment with GB201 at the gradient concentrations. Data are graphed as the mean ± SD; *, P < 0.05; **, P < 0.01; ***, P < 0.001; ns, nonsignificant, P > 0.05.

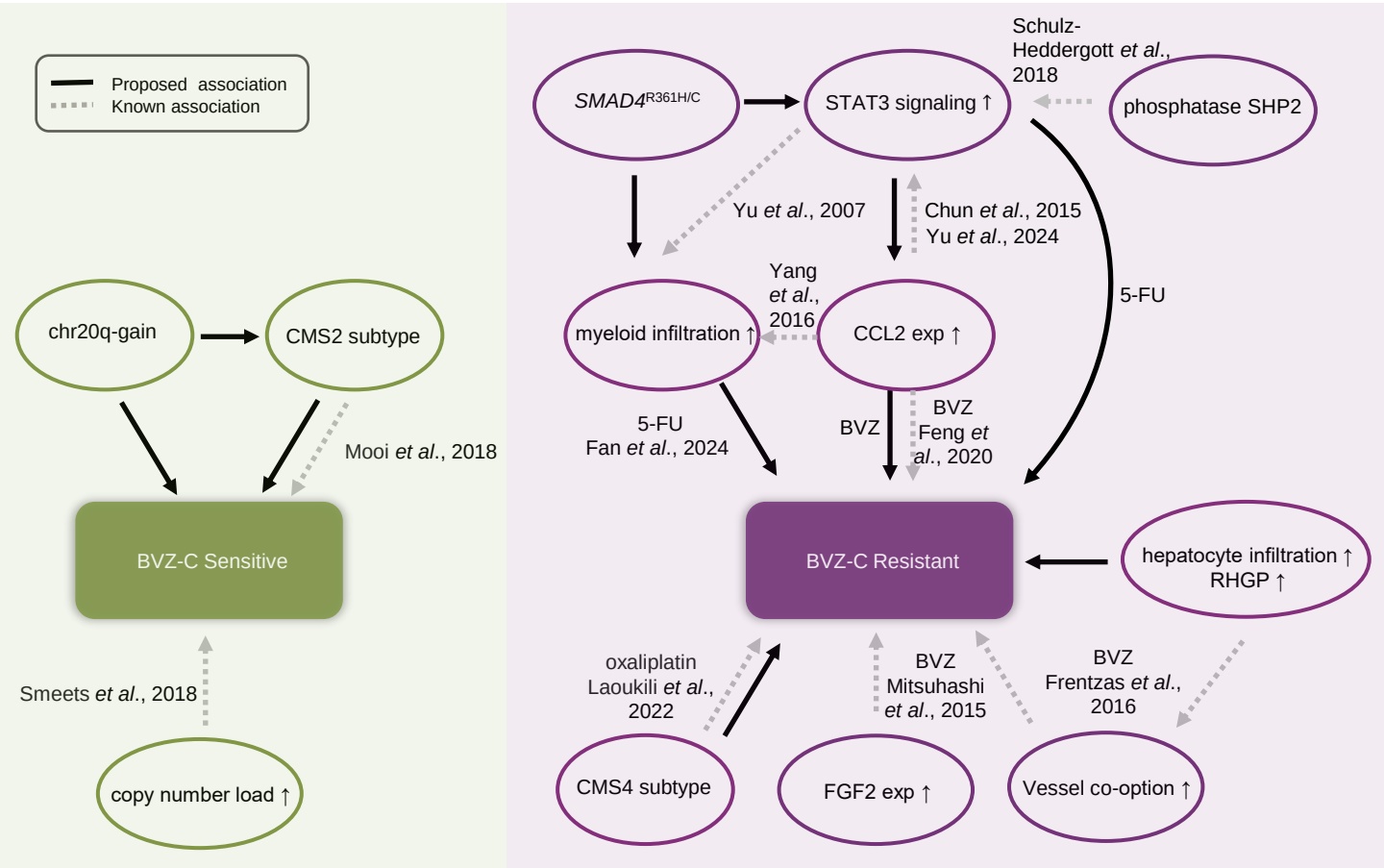

Figure S12. Summary representation of the known and newly identified molecular features linked to BVZ-C response in CRLM, related to Figure 6.

Previous papers reporting the associations are labelled. Features with black lines are the associations proposed in this study. Arrows directed upward within the circles indicate activated signaling, high expressed or increased number..